An Investigation of The Antimicrobial Effect of Porphyrin Dyed Titanium Dioxide Nanofibers in Pure Rutile and Mixed Anatase /Rutile Phases

A thesis submitted in fulfilment of the requirements for the degree of

MASTER OF SCIENCE

at

RHODES UNIVERSITY

Kamogelo Hlabangwane

Dedications

This work is dedicated to all the women in my life.

Acknowledgements

First and foremost, I would like to extend my deepest gratitude to the **Distinguished Professor Tebello Nyokong**, for her passion and dedication to all of us, her students, and our work. I would also like to extend my gratitude to my co-supervisor, Dr Muthumuni Managa, and mentors Dr Refilwe Matshitse and Dr Azole Sindelo for their teachings and guidance throughout the production of this work. Their help and greatly appreciated.

I thank the people in the Tebello Nyokong Institute for Nanotechnology Innovation, Ms. Gail Cobus, Professor John Mack, Dr Johnathan Britton and Mr. Francis Chindeka for ensuring the smooth operations of the department, as well as the students of the Tebello Nyokong-INI for their continued support. I thank my friends and family, more especially, my mother, for their immense support and encouragement throughout the completion of this work. I would like to thank the National Research Foundation (NRF) for its financial support.

I can do all thing through Christ who strengthens me.

– Philippians 4:13

Abstract

South Africa and many other nations face an issue of a decline in the quality of fresh water. One of the factors causing this decline is contamination by biological components such as bacteria and other microorganisms present in the water. Over time, microorganism can mutate and become resistant to common available treatments. The World Health Organisation has reported that antimicrobial resistance is one of the top 10 health threats that humanity faces today. Alternative therapies such as antimicrobial photodynamic inactivation (aPDI) are methods that can be used to inactivate bacteria while reducing the possibility of antimicrobial resistance. The method uses a combination of light, a photosensitiser and molecular oxygen to generate reactive oxygen species that can be used to target microbial tissue.

In this work asymmetric and symmetric tin (II) and indium (III) porphyrins functionalised with methoxy and thiomethyl substituents were adsorbed onto mixed phase anatase/rutile titanium dioxide (TiO_2) nanofibers and onto rutile titanium dioxide nanofibers. The effects of metalation, symmetry of the porphyrins and adsportion onto different phases of TiO_2 nanofiber are explored and reported on in this work. The porphyrins exhibited good photophysical properties with high singlet oxygen quantum yields and low fluorescence.

Staphylococcus aureus, Escherichia coli and *Candida albicans* were the model microorganisms use in the aPDI studies. The results obtained in this research showed the porphyrins and nanofibers were not effective in the inactivation of *E. coli* and *C. albicans*, however, upon adsorption with metalloporphyrins both the mixed-phase anatase/rutile TiO_2 nanofiber and rutile TiO_2 nanofiber were able to inactivate *S.*

aureus. Reusability studies indicated that the mixed-phase anatase/rutile TiO_2 nanofibers have good potential in multiuse applications in the inactivation of *S. aureus*.

Based on the results obtained in this research, it can be concluded that the porphyrins and nanofibers have a synergetic effect that increases efficacy in the eradication of microorganisms for *S. aureus*.

Contents

List of abbreviations

^{1}H NMR	Proton nuclear magnetic resonance
ADMA	9,10-Antracenediyl-bis(methylene)dimalonoic acid
AMR	Antimicrobial resistance
aPDI	Antimicrobial photodynamic inactivation
$BF_3O(Et)_2$	Boron trifluoride diethyl etherate
CFU	Colony forming units
$CDCl_3$	Deuterated chloroform
DCM	Dichloromethane
DDQ	2,3-Dichloro-5,6-dicyano-1,4-benzoquinone
DMA	9,10-Dimethylanthacene
DMF	Dimethylformamide
DMSO	Dimethyl sulfoxide
DMSO-d6	Deuterated Dimethyl sulfoxide
FTIR	Fourier transform infrared spectroscopy
HOMO	Highest occupied molecular orbital
LUMO	Lowest occupied molecular Orbital
MALDI TOF-MS	Matrix-assisted laser desorption ionisation time of flight mass spectrometry
PDT	Photodynamic Chemotherapy
PVP	Polyvinylyrrolidone
ROS	Reactive oxygen species
SEM	Scanning electron microscopy
TCSPC	Time-correlated single photon counting setup

TPP	Tetraphenylporphyrin
TGA	Thermogravimetric analysis
TFA	Trifluoroacetic acid
TiO_2	Titanium dioxide
UV-Vis	Ultraviolet- visible
XRD	X-Ray diffraction
WHO	World Health Organisation

List of symbols

S_0	Ground state
S_1	Excited singlet state
S_2	Excited second state
T_1	Triplet-state
$^1O_2$	Singlet oxygen
$^3O_2$	Ground state oxygen
$O_2^{-\cdot}$	Superoxide
$OH^{\cdot}$	Hydroxyl radical
Φ_F	Fluorescence quantum yield
τ_F	Fluorescence lifetime
τ_T	Triplet lifetime
Φ_Δ	Singlet Oxygen Quantum Yield
ε	Molar extinction coefficient

Chapter 1

Introduction

The chapter highlights the problem statement, gives an overview of reported research on porphyrins and titanium dioxide nanofibers and their application in antimicrobial photodynamic inactivation studies.

Problem Statement

South Africa is currently facing an issue of water scarcity. The quality of freshwater is constantly deteriorating due to various factors and among these factors are chemical pollution from industries and mines, and biological contaminants[1]. Biological contamination refers to the presence of living organisms in water. These organisms can lead to fatal water-borne diseases and cause infections in humans. Gram-negative *Escherichia coli (E. coli),* which is a common bacterium found in contaminated water sources, has been reported to be the most common cause of diarrhoeal diseases and gastrointestinal tract infections and this is especially fatal to children[2]. On the other hand, gram-positive S*taphylococcus aureus (S. aureus)* can be easily spread on contact when good sanitation and hand washing are not observed. It is highly infectious in clinical settings and can be fatal if introduced to the bloodstream or internal tissue[3]. This bacterium is a cause of concern when found in drinking water as isolated samples were found to contain the *mecA* gene which causes resistance to antimicrobials[4], and can produce enterotoxin in the body[5].

Candida species have been isolated in drinking groundwater and have been reported to show antifungal resistance and express virulence factors that can cause and worsen infections upon contact[6,7]. As a result, the antimicrobial activity against the singled celled fungi, *Candida albicans (C. albicans)* along with both the aforementioned bacteria are explored in this thesis.

Bacteria and other microbes are usually treated with antibacterial and antimicrobial agents which over time could become ineffective as bacteria can mutate and become resistant to the common antibacterial treatments. The World Health Organisation (WHO) has declared antimicrobial resistance (AMR) as one of the top 10 public health threats facing humanity[8].

In this research, photosensitiser-dyed titanium dioxide nanofibers that will be applied in photodynamic antimicrobial inactivation are synthesised in an effort to decontaminate water of biological contaminants such as gram-positive, gram-negative bacteria and fungi, such that the people who are negatively affected by these contaminants could have an affordable, reusable solution to cleaner drinking water. This alternative therapy to common antimicrobial therapies utilises singlet oxygen species to disturb the biological functions of the cell, which then can be used to target resistant microorganisms.

AIMS OF THIS WORK

This work aims to develop porphyrin-adsorbed nanofibers and investigate their antimicrobial effect in water, as a potential water decontamination solution. A novel porphyrin along with reported porphyrins are used, where some of their antimicrobial properties are assessed for the first time.

The objectives were observed as follows, where,

- two different functional groups are attached to the porphyrins are utilised in investigating the effect of heavier functional groups on singlet oxygen production and antimicrobial activity.
- inorganic titanium dioxide nanofibers are fabricated, and their antimicrobial activity is explored. In addition to this, the activity of different phases of nanofibers, more specifically, a mixture of rutile and anatase nanofibers with pure rutile, highly stable nanofibers are compared.
- photoactive porphyrins are dyed onto photocatalytic nanofibers to synergistically inactivate different classes of microbes. Novel explorations of the antimicrobial activity of previously reported and newly synthesised Sn porphyrin-dyed TiO_2 nanofibers are explored in this work.

1.1 ANTIMICROBIAL PHOTODYNAMIC INACTIVATION (aDPI)

1.1.1 MICROBIAL RESISTANCE

Bacteria are simple prokaryotic cells that can be identified and classified by different features and among these is the structure of their cell wall. The cell wall serves as a protective layer for the organism from the external environment. There are two different types of bacterial cell walls, namely, gram-positive, and gram-negative cell walls. The image in Fig. 1.1 compares the structure of the cell wall of a gram-positive and of a gram-negative bacterium.

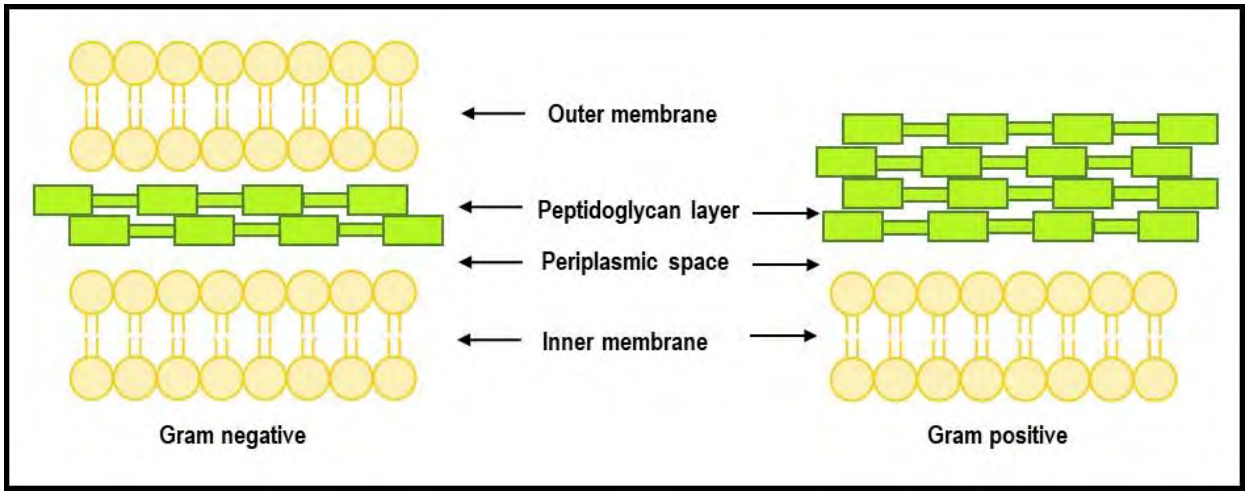

Figure 1.1: Structural differences in gram-negative and gram-positive cell walls.

A gram-positive bacterial cell wall does not have an outer membrane but is composed of a thick peptidoglycan layer while the gram-negative cell wall is composed of an inner and outer membrane with a thin peptidoglycan layer between the membranes. The outer membrane provides extra protection and increases the cells' adaptability in environments, therefore making it harder to inactivate gram-negative cells, while also increasing their chances of building resistance to traditional antibacterial treatments.

Gram-positive *Staphylococcus aureus,* gram-negative *Escherichia coli, and* single-celled yeast cells of *Candida albicans* (*C. albicans*) are the model microorganisms to be assessed in this work. These microbes, along with many others can develop resistance to drugs through various mechanisms. *S. aureus* develops resistance to drugs through de novo mutations in chromosomal genes or through the acquisition of horizontally transferred resistant determinants, as in the case of Methicillin resistance, where mecA genes with low affinity to β-lactams lead to resistance to this class of drugs[9]. Cephalosporins are a β-lactam class of antibiotics most used to treat gram-negative bacteria. *E. coli* can become resistant to these drugs by producing extended-spectrum beta-lactamase that can hydrolyse and inactivate β-lactam drugs[10,11]. The more complex eukaryotic fungi cells of *C. albicans* are highly adaptable and have been reported to develop resistance to various antifungals through various mechanisms outlined by Costa-de-Oliveira &Rodrigues[12], and Lee et al[13]. This wide range of microbial resistance to drugs has raised a necessity for methods like aPDI to be explored in the inactivation of bacteria.

Antimicrobial photodynamic inactivation (aPDI) is a non-invasive alternative method to traditional therapies such as antibacterial, antifungal, and antivirals, that has proved to be effective in microbial inactivation. This therapeutic method requires the use of a non-toxic photosensitiser[14,15] that can be illuminated with light of an appropriate wavelength to generate reactive oxygen species (ROS) that cause non-specific, irreversible oxidative damage to target tissue[16]. Photosensitisers absorb light and transfer the energy from the light to the nearby oxygen molecules generating ROS that inactivate nearly cells.

1.1.2 MECHANISM OF ACTION of aDPI

Fig. 1.2 shows a Jablonski diagram that can be used to explain the mechanism of the principle of aPDI

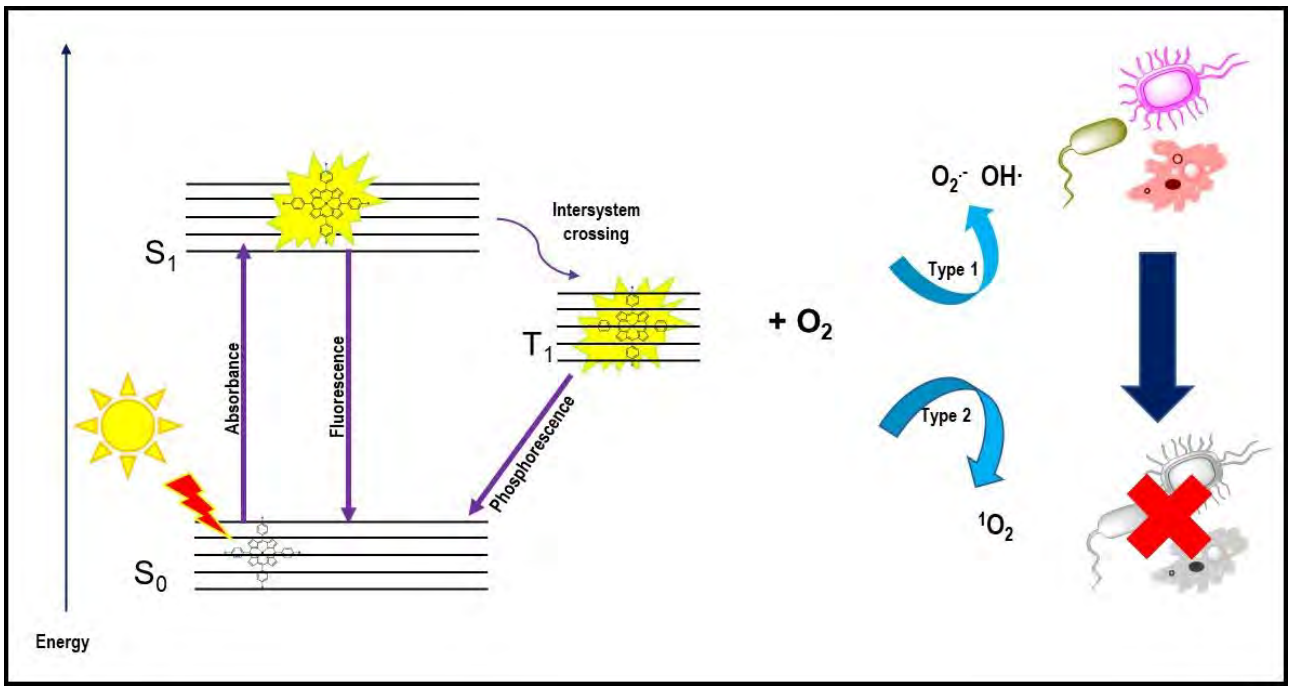

Figure 1.2: A Jablonski diagram showing the excitation patterns that can be experienced by a photosensitiser upon excitation.

Upon absorbing the light, photosensitisers can be promoted from the ground state (S_0) into an excited singlet state (S_1), where they can either fluoresce back to the S_0 or undergo intersystem crossing into the triplet state (T_1). In the T_1 state, the photosensitiser reacts with nearby ground state oxygen species ($^3O_2$) to create reactive oxygen species (ROS) such as singlet oxygen ($^1O_2$) that results in the death of nearby tissue[17] as depicted in Fig. 1.2.

Photosensitisers produce ROS through type 1 and type 2 mechanisms[18] to inactivate different microorganisms such as bacteria, fungi[19,20], viruses and protozoa[20]. In a type

1 mechanism, photosensitisers in the excited triplet state (T_1) react with biomolecules that transfer energy to molecular oxygen to produce cytotoxic reactive oxygen species (ROS) in the form of free radicals such as superoxides ($O_2^{-\cdot}$) and hydroxyl radicals ($OH^{\cdot}$) that result in irreversible oxidative damage to the cells. In a type 2 mechanism, the photosensitiser reacts with molecular oxygen to produce singlet oxygen ($^1O_2$) species that are highly cytotoxic to nearby cells, by causing damage to biological molecules such as nucleic acids, lipids, enzymes and proteins[16,18,21].

1.1.3 ADVANTAGES of aDPI

The method is advantageous as the photosensitisers used have a broad-spectrum action that allows activity against a diverse range of microorganisms[22]. Another advantage is that their mechanism of action, through the use of ROS, reduces the development of microbial resistance as they react with different biomolecules and target different cellular structures[18,22]. aPDI has reduced adverse effects and generally causes less damage to host tissue[22].

1.2 PORPHYRINS

The photosensitiser that will be used in this research are porphyrins. Porphyrins are an abundant group of naturally occurring molecules such as haemoglobin and chlorophyll that participate in important biological processes such as oxygen transport and photosynthesis respectively[23].

Porphyrins are heterocyclic macrocycle aromatic organic compounds that are made up of four pyrrole subunits linked together by a methane bridge[24], Fig. 1.3. Porphyrins

contain 22-π electrons, where 18 of them are involved in the delocalisation of the π-conjugated framework[25] and form an aromatic system that fits into Hückel's rule of aromaticity (4n+2 delocalised electrons). In their free base form, they exhibit an intense purple colour and absorb light largely in the visible region of the electromagnetic spectrum[23].

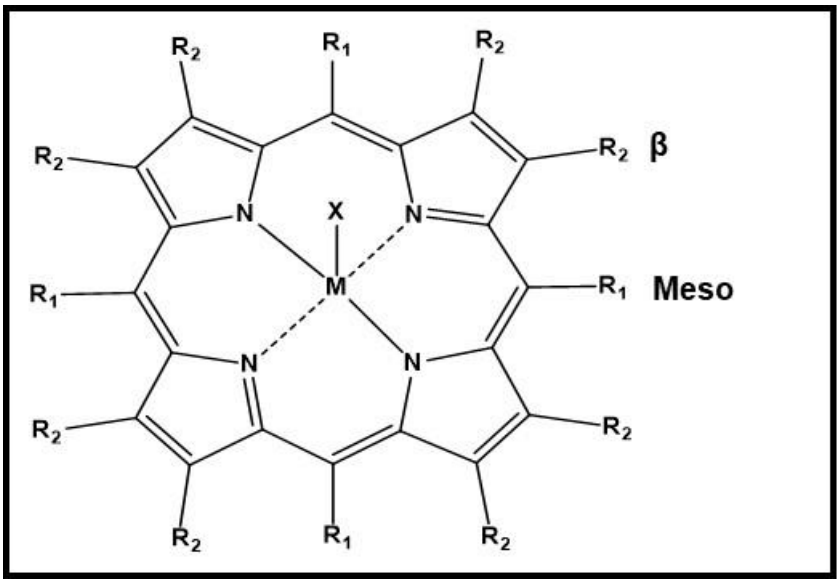

Figure 1.3: Possible substitution points of a porphyrin, where R1 and R2, R2 are the meso and beta positions, M is the central metal and X is the axial ligand.

At the skeleton, porphyrins can either be substituted at the meso positions and the β-positions as depicted by R_1 (meso) and R_2 (β), respectively, in Fig. 1.3. A metal along with an axial ligand can be inserted at the core of the porphyrin and these are represented with M and X in Fig 1.3, respectively.

1.2.1 PORPHYRIN SYNTHESIS

1.2.1.1 The Rothemund method

The Rothemund method was first reported in 1941[22]. This method employs a condensation reaction where an aldehyde and pyrrole are reacted in pyridine under inert conditions and are heated in a furnace at 220 ℃ for 48 h. The heating process is followed by slow cooling of about 10 h to yield 10 % of the porphyrin[26], Scheme 1.1.

1.2.1.2 Adler-Longo method

The inert, sealed-tube Rothemund method for synthesis of tetraphenylporphyrin (TPP) was inconvenient for thermodynamic and kinetic studies and this led to a modification by Alder et al[27,28] to what is now known as the Adler-Longo method. This method is a simpler condensation reaction where an aldehyde and distilled pyrrole are refluxed in an acid, such as propionic acid in open-air conditions at 141℃ for 30 min increasing the yield to 20%[28], Scheme 1.1. Since its report in 1964 this method has been widely used to synthesise an impressive number of porphyrins[29]. This method was also employed in the synthesis of the porphyrins used in this work.

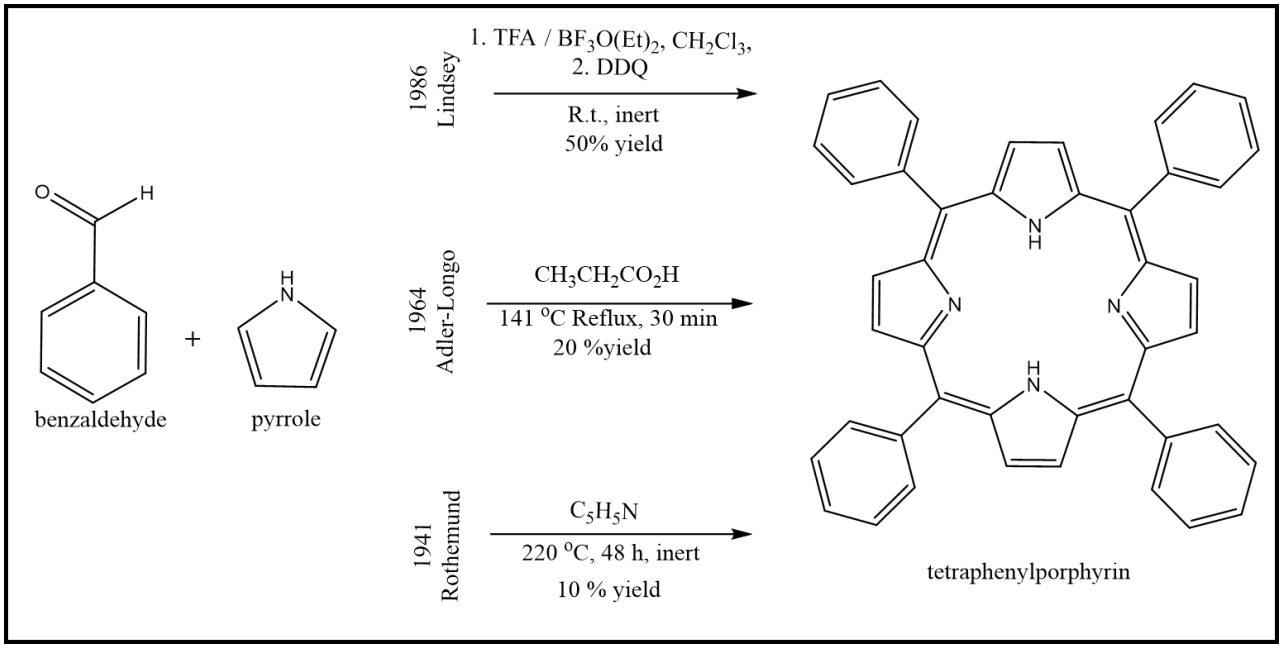

Scheme 1.1: Schematic diagram showing the Rothmund, Adler Longo and Lindsey methods of porphyrin syntheses.

1.2.1.3 Lindsey method

The Lindsey method was later developed by Jonathan S. Lindsey and colleagues[30,31] in an effort to synthesise porphyrins in a gentle approach. This method involves a 2-step, 1-pot reaction where a porphyrinogen is formed in the first step and then oxidised into a porphyrin in the second step. In a typical setup, pyrrole and an aldehyde are reacted in dry dichloromethane (DCM) under inert conditions at room temperature and then catalysed with a trace acid catalyst (boron trifluoride or trifluoracetic acid). After about 1 h, an oxidising agent such as *p*-chloranil or 2,3-dichloro-5,6-dicyano-1,4-benzoquinone (DDQ) is then added to irreversibly oxidise the porphyrinogen formed in step 1 into a porphyrin[30,31] increasing the yield up to 50% depending on the aldehyde used[29], Scheme 1.1. This method allows aldehydes with sensitive functional groups to easily be converted into porphyrins. The method has also been used to synthesise a

multitude of novel porphyrins such as disubstituted porphyrins, ruffled porphyrins, capped porphyrins, and expanded porphyrins[29].

The methods above can be used to synthesise both symmetric and asymmetric porphyrins, where different aldehydes can be used in different ratios to yield the desired porphyrins. Symmetrical A_4 substituted, porphyrins are usually easier to synthesise as they require an equimolar 1:1 ratio of pyrrole and aldehyde.

Asymmetrical porphyrins, however, require two different aldehydes of different ratios, typically a ratio of 1:3, that are reacted with an equimolar pyrrole. This then results in the formation of a different array of porphyrins (A, A_3B, A_2B_2, AB_3) where the desired product is then isolated using other methods such as chromatography. This method was used in the synthesis of the porphyrins used in this work.

1.2.2 ELECTRONIC ABSORPTION SPECTRA OF PORPHYRINS

The UV-visible absorption spectrum of highly conjugated porphyrin macrocycle exhibits an intense peak of the Soret band between 400 and 450 nm that is due to a strong $S_0 \rightarrow S_2$ transition, followed by several weaker Q-band absorptions (typically four for free base porphyrins which become 1 or 2 upon metallation, depending on the type of metal inserted) at higher wavelengths typically ranging between 500 and 750 nm that are a result of the weaker $S_0 \rightarrow S_1$ transition. The Soret and Q-bands both arise from the π-π* transitions and can be better explained by the Gouterman four orbital model[32,33].

Using this model, Martin Gouterman theorised that the absorption bands in the porphyrin system are a result of transitions between two highest occupied molecular

orbitals (HOMOs) (a_{1u} and a_{2u}) and two lowest unoccupied molecular orbitals (LUMOs) (e_{gx} and e_{gy}), and these are represented in Fig. 1.4. The relative energies of these transitions are dependent on the identities of the metal centre and the substituents on the ring.

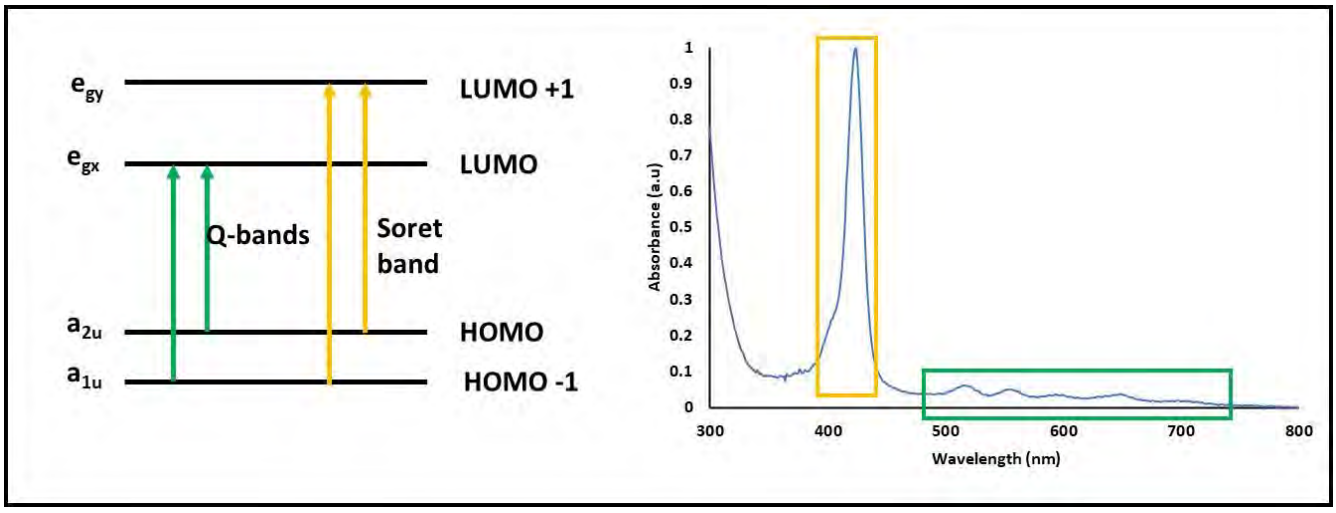

Figure 1.4: Electronic transitions showing the rise of the Soret peak and Q-bands as explained by the Gouterman four orbital model for free base porphyrins.

The absorption of these peaks can vary in wavelength and intensity. The exact positions, shapes, and intensities of the absorption bands in the spectra of porphyrins can be influenced by various factors, including the nature and number of peripheral substituents, the type of central metal ion, the electronic structure of the porphyrin, and the solvent used. These factors can cause spectral shifts, broaden, or split the absorption bands or add new characteristics to the spectra[25,32].

1.2.3 PORPHYRIN APPLICATIONS

Porphyrins have a vast range of applications and they can be used in fields such as medical, drug delivery, bio-sensing, and bio-imaging applications[24,34,35]. They can also be used in biomimetic catalysis, where metalloporphyrins are studied as catalysts for oxidizing organic compounds and for water splitting to generate molecular hydrogen and oxygen for fuel cells[36], in molecular electronics and sensors where synthetic metalloporphyrins dyes and some porphyrin analogues are incorporated in dye-sensitised solar cells and are being investigated as sensors[37,38] as well as photodynamic therapy/ photodynamic antimicrobial chemotherapy and aPDI where they are used as photosensitisers[18]. In this work, porphyrins are applied in aPDI.

1.2.4 PORPHYRINS IN aPDI

Porphyrins are ideal for aPDI because they exhibit a good production of $^1O_2$ which is responsible for photoinactivation when excited with light. The effectiveness of porphyrins in aPDI is strongly related to the molecular structure of the photosensitiser. The structure can be altered by functionalising the porphyrin with substituents on porphyrin's skeleton or by adding a central metal[17] in the core.

When used as photosensitisers, research suggests that asymmetrical porphyrins are more effective as they allow a different charge distribution over the new macrocycle [39].The different charge distribution also gives the porphyrin slightly amphoteric character that aids in enhanced transportation of the photosensitiser to the cellular targets in both polar and non-polar media for the external environment of the cell and lipid bilayer of the cell membrane, respectively[39].

Tin and indium have previously been used as central metal in aPDI and photophysical studied as they have proved to enhance the production of singlet oxygen and yield great inactivation results in previously reported microbial studies. Some of these are studies reported in Table 1.1[36-48].

Table 1.1: Sn and In metallated porphyrins previously reported in microbial studies, along with Sn porphyrins applied in combination with Titania.

Compound	Application	Reference
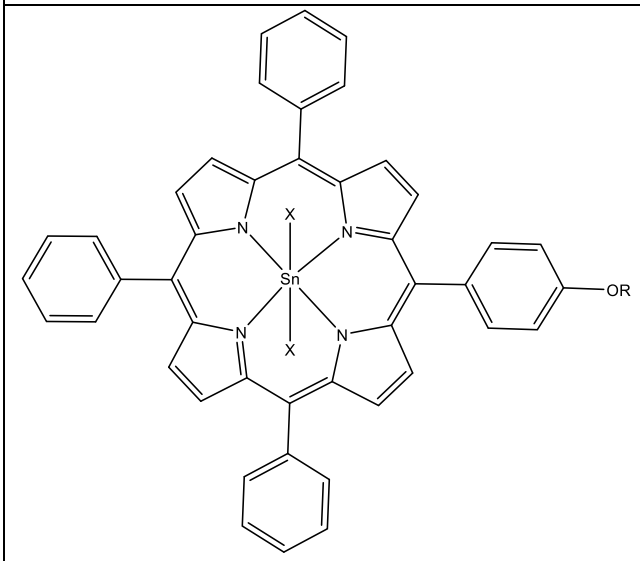 R= C_8H_{17}, $C_{16}H_{33}$ X = Cl, OH	Photophysical studies and aPDI against gram (+) *B. subtilis* and gram (-) *E. coli*.	[40]
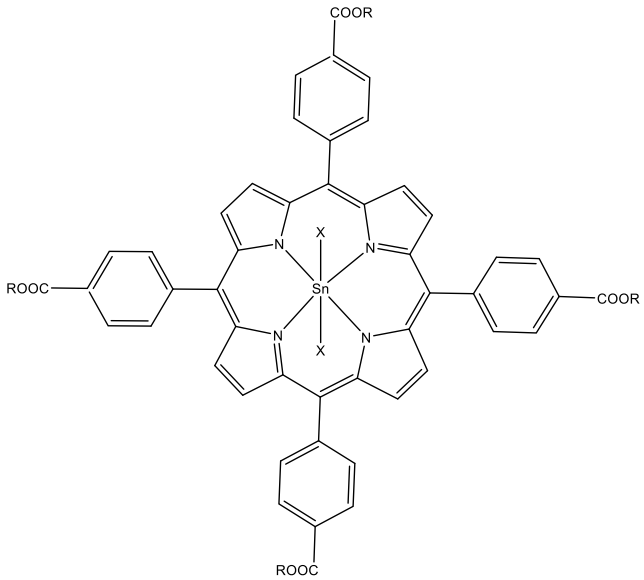	Photophysical studies, aPDI application against *C. albicans*	[41]

X=OH, 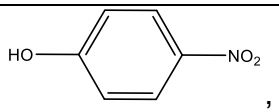 , R=CH_3, H		
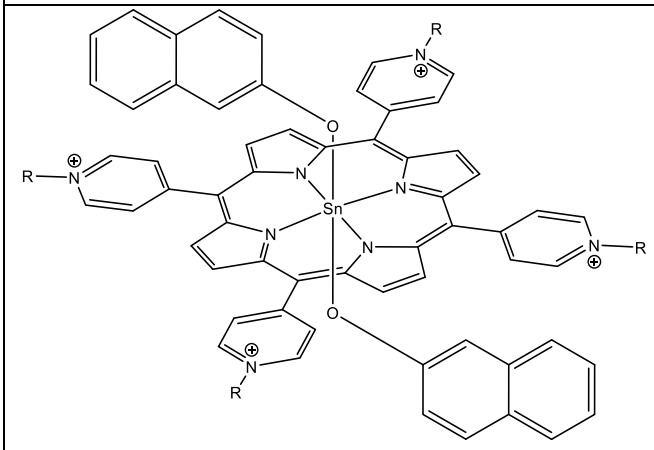 R= CH_3, C_6H_{13}	Photophysical studies, aPDI application against *S. aureus*	42
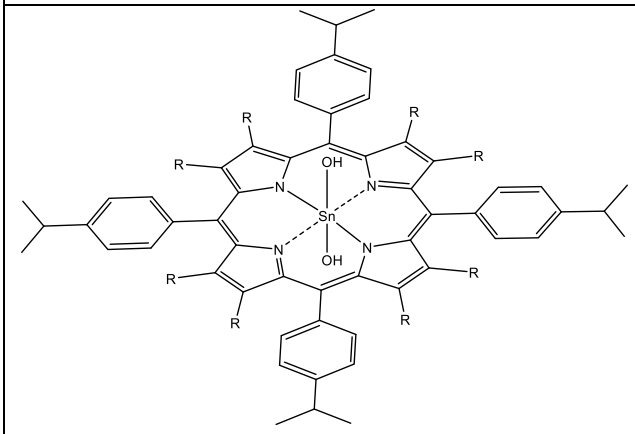 R= H, Br	Photophysical studies, aPDI application against *S. aureus*	43

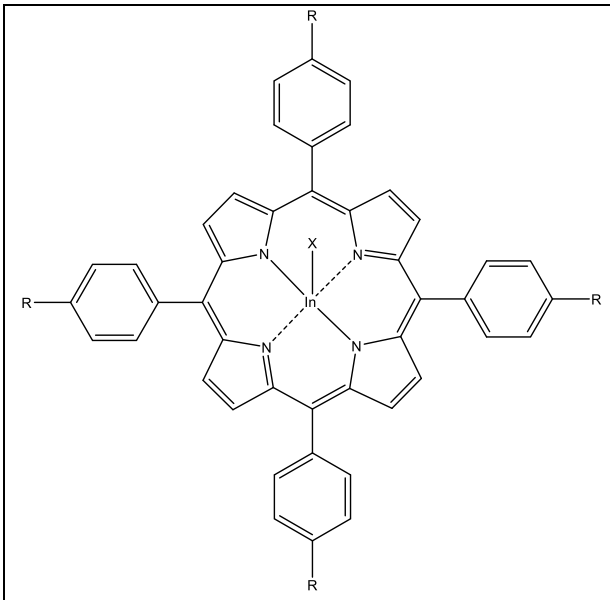 X = Cl, 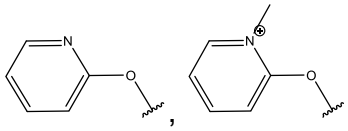 R=SCH_3, OCH_3, Br, Cl	Photophysical studies, aPDI application against *S. aureus* aPDI studies were performed against Methicillin Resistant *S. aureus* (*MRSA), C. perfringens*, and *S. enterica*.	44,45 46
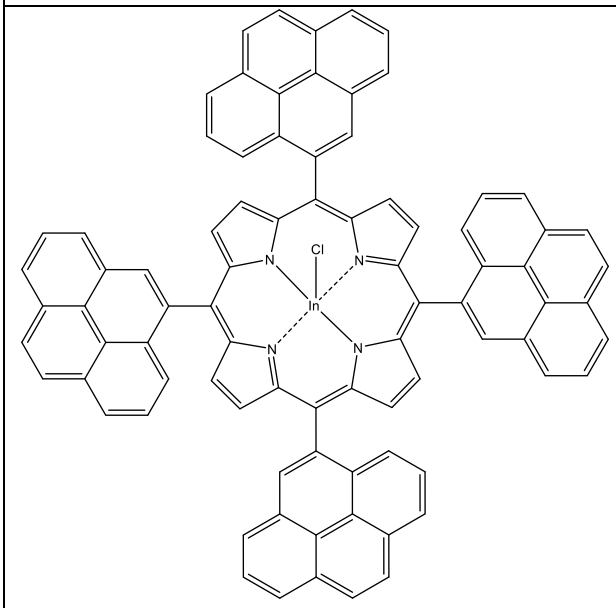	Photophysical studies, aPDI application against *S. aureus*	47

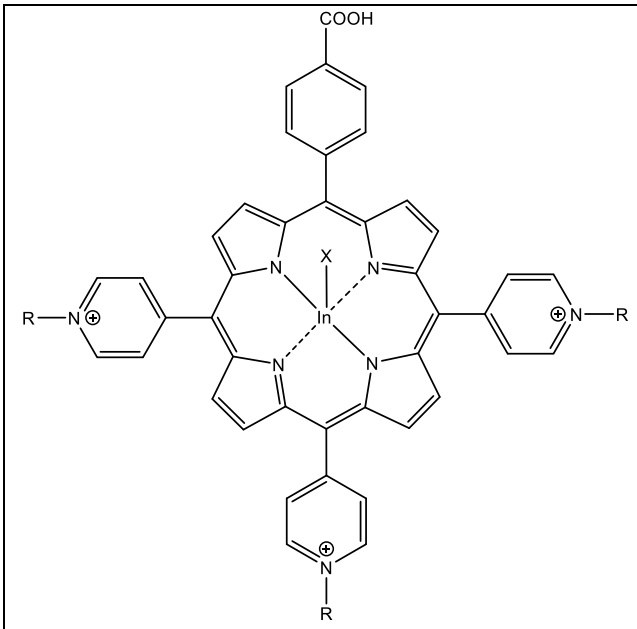 a. X=Cl, R=CH_3, C_6H_{13} b. X= 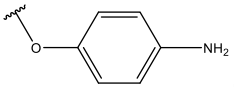 , R=CH_3, C_6H_{13}	Photophysical properties were studied. The molecules were used in aPDI application against *E. coli* and of *S.aureus*	48 45
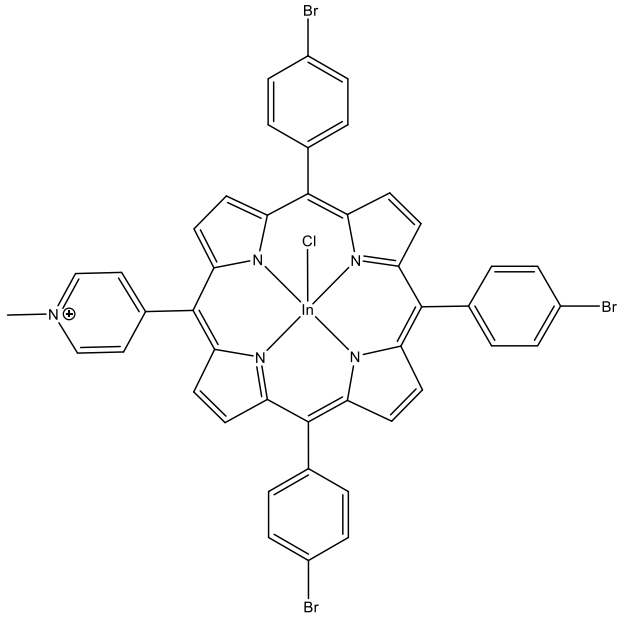	Photophysical properties were studied, aPDI application against *S. aureus*	50

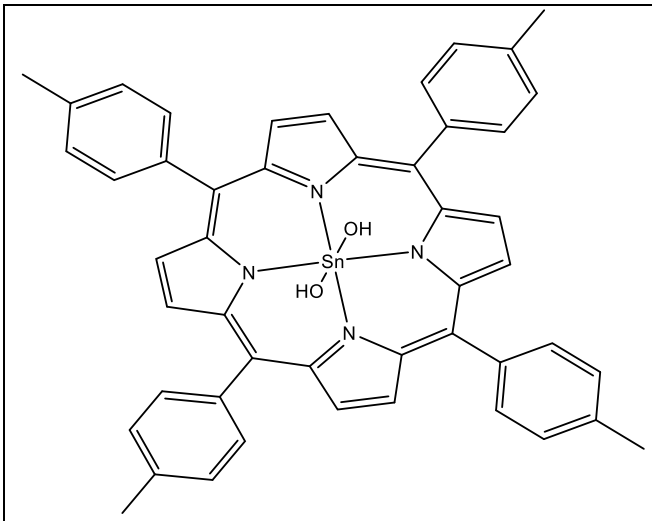	Porphyrin was Intercalated into trititanate ($H_2Ti_3O_7$) nanofibers. Optoelectronic and photocatalytic properties were investigated.	[51]
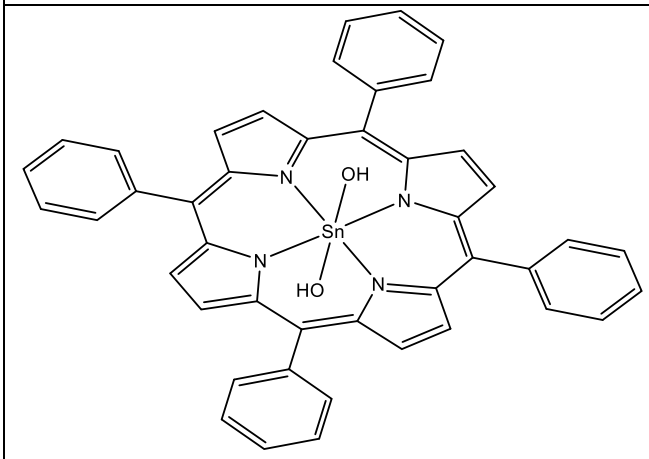	Porphyrin-incorporated TiO_2 nanotubes and nanofibers were applied in the visible light photodegradation of methylene blue.	[52]

The data presented in Table 1.1 shows limited studies on asymmetric porphyrins for applications in aPDI, hence a subject for this thesis. Bulkier groups are substituted at the axial ligand to prevent aggregation of the porphyrins in aqueous media[53].

1.2.5 PORPHYRINS IN THIS WORK

In this work, various porphyrins were synthesised successfully using the Alder-Longo method and were applied in aPDI, Table 1.2. Previously reported 5,10,15,20-

tetrakis(4-methoxyphenyl)porphyrin[54–58] and 5,10,15,20-tetrakis (4-(methylthio)phenyl)porphyrin[59] were synthesised and investigated. The asymmetric 5,10,15-tris(4-methoxyphenyl)-20-(4-(methylthio)phenyl)porphyrin, was synthesised and reported for the first time in this work, Table 1.2.

Positively charged photosensitisers are highly favoured as they tend to have better distribution and improved solubility in aqueous media[60]. These photosensitisers are also better for applications against gram-negative bacteria, as the positively charged molecules allow for better localisation onto the negatively charged cell wall. The challenge of using water soluble porphyrins in this work was that post bacterial inactivation, porphyrins would first need to be removed from the water before it is suitable for use.

To combat this challenge, two approaches were employed to ensure that porphyrins do not dissolve in the water. The porphyrins were adsorbed onto nanofibers such that the dyed nanofibers could be recovered post microbial inactivation. The other approach was to synthesise neutral porphyrins that are non-soluble in aqueous media. These porphyrins were functionalised with methoxyphenyl- and 4-(methylthio)phenyl groups, as well as tin (II) and indium (III) chloride in an effort to enhance their activity.

In a study by Gladkowski et al., some methoxy-substituted flavanones were studied against their unsubstituted counterparts where it was noted that the compounds containing the methoxy substituents inhibited the growth of various bacteria and fungi[61] . Similar results were observed in studies by Suwito et al. and Marques et al. where variations of chalcones containing the methoxy substituents displayed antibacterial and antifungal properties[62,63].

Heavy atom effect is known to promote intersystem crossing into the T_1 where ROS are created. Methyltio groups were employed in this thesis to compare the heavy metal effect of sulphur in the methylthio group against the oxygen in the methoxy group. The porphyrins were also metallated with heavy metals containing axial ligands to also take advantage of the heavy atom effect and promote the production of singlet oxygen species.

Table 1.2: Porphyrins that were used in this work. The type of nanofibers they were adsorbed onto and the microbes they were used to inactivate.

Porphyrin		TiO_2 nanofiber phase	Inactivated microbe
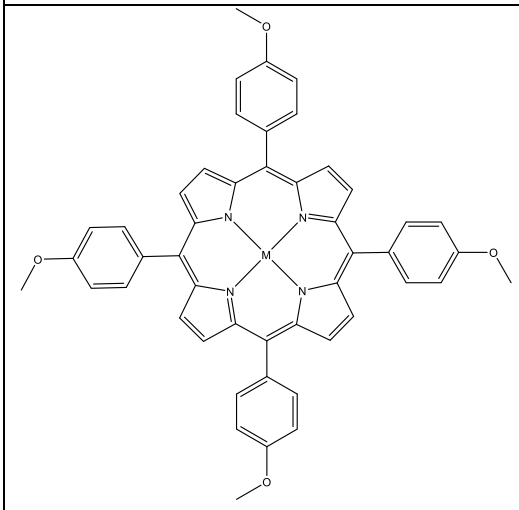 **1**[54] **1-Sn**[55,56] **1-In**[57,58]	**1-Sn**	Mixed anatase/rutile Rutile	*S. aureus*
	1-In	Mixed anatase/rutile	*S. aureus*

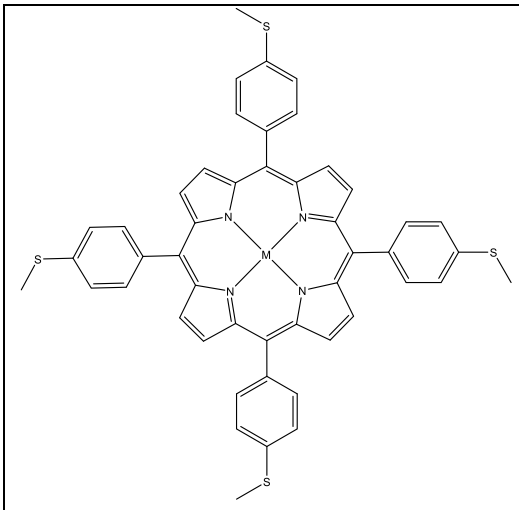 **2-Sn**[59]		Rutile	*S. aureus* *E. coli* *C. albicans*
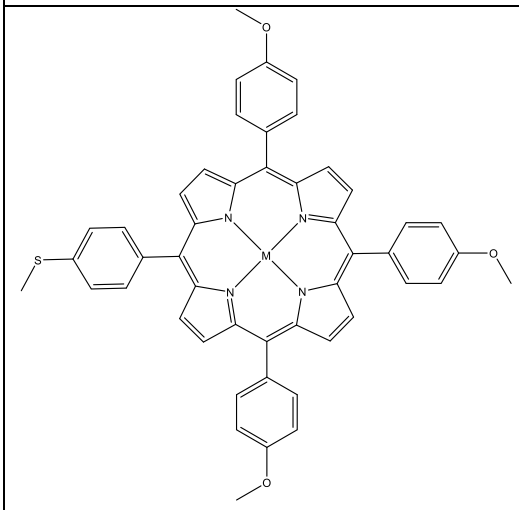 **3** **3-Sn**	**3**	Rutile	*S. aureus* *E. coli* *C. albicans*
	3-Sn	Rutile	*S. aureus* *E. coli* *C. albicans*

1.2.6 PHOTOPHYSICOCHEMICAL PROPERTIES

The potential effectiveness of porphyrins can be assessed by their photophysicochemical properties. Molar extinction coefficient, fluorescence lifetimes, fluorescence quantum yields, and singlet oxygen quantum yield are some of the important parameters that are used to assess the potential effectiveness of a porphyrin.

1.2.6.1 Fluorescence quantum yields (Φ_F), fluorescence lifetimes (τ_F) and triplet lifetimes(τ_T)

Fluorescence quantum yield can be described as the ratio of photons absorbed to the photons emitted. The Φ_F values of the complexes were determined using a comparative method[64,65], where the emission spectrum of a sample is compared with that of a standard (zinc tetraphenylporphyrin (ZnTPP) in n,n-dimethylformamide (DMF)) (Φ_F^{Std} = 0.033)[66], both being excited at the same wavelength. Φ_F was calculated according to Eq. 1.1,

$$\Phi_F = \Phi_F^{Std} \frac{F\ A^{Std}\ n^2}{F^{Std} A\ (n^{Std})^2} \quad (1.1)$$

where F and F^{Std} are the areas under the fluorescence curves for sample and standard, respectively. A and A^{Std} are the absorbances of the sample and reference at the excitation wavelength, respectively. *n* and n^{Std} are the refractive indices of the solvent used for the sample and standard, respectively. The Φ_F values were determined for all porphyrins exciting at 490 nm. Fluorescence and triplet lifetimes of porphyrins were

measured. Fluorescence lifetime (τ_F) is defined as the average time a fluorophore spends in the excited state before it emits a photon and drops to the ground state through radioactive or non-radioactive decay[67].

Lower fluorescence lifetimes are preferred as this implies that there are higher chances of intersystem crossing into the excited triplet state. On the contrary, longer triplet-state lifetimes (τ_T) are preferred as this increases the chances of singlet oxygen production.

1.2.6.2 Singlet oxygen quantum yield (Φ_Δ)

Singlet oxygen quantum yield quantitively measures the efficiency of photosensitisers in converting molecular oxygen into reactive singlet oxygen species in the presence of light. It can be described as the number of $^1O_2$ species being generated per photon absorbed by the photosensitiser[68]. Alternative quenching routes of a photosensitiser such as fluorescence, phosphorescence, nonradiative decay and triplet-triplet annihilation can limit the production of Φ_Δ[69,70]

The Φ_Δ for porphyrins were performed in dimethylformamide (DMF) and were calculated using Eq. 1.2,

$$\Phi_\Delta = \Phi_\Delta^{Std} \cdot \frac{\boldsymbol{B} \cdot \boldsymbol{A^{Std}}}{\boldsymbol{B^{Std}} \cdot \boldsymbol{A}} \qquad (1.2)$$

where Φ_Δ^{Std} is the singlet oxygen quantum yield for the ZnTPP standard in DMF(Φ_Δ^{Std}= 0.53)[71] B and B^{Std} refer to a coefficient related to the sensitiser concentration and the $^1O_2$ quantum yield for the sample and standard, respectively; while A and A^{Std} refer to the absorbance values at the excitation wavelengths. The singlet oxygen quantum

yields for the metalloporphyrins were determined in DMF using 9,10-dimethylanthacene (DMA) as the singlet oxygen quencher. The samples were radiated at 30 s intervals for 210 sec using a broad-spectrum LED lamp of 70 kW.

1.3 NANOFIBERS

The field of nanotechnology has grown extensively over the past few decades leading to advancements in the production and function of nanomaterials and among these materials are nanofibers. Nanofibers are fibrous materials with diameters between 1 nm and 1 μm that can be applied in different areas and have shown to have great potential in environmental remediation, energy storage, functional catalysts, cosmetic and biological applications[72–74], and as such, they can be used as a method of delivery for antibacterial therapies.

Titanium-based nanomaterials have been widely researched in different fields such as water splitting and hydrogen production, photo-electrochemistry, dye sensitisation, solar energy conversion, and photochemical air and water treatments[75]. TiO_2 photocatalysts are the most used and have been widely researched due to their high photoactivity and stability[76,77].

TiO_2 nanofibers have recently gained some attraction in antimicrobial research due to their good chemical stability, non-toxic, and inexpensive nature[78] in addition to having good photocatalytic and antimicrobial properties.

TiO_2 can be found in an anatase phase, a rutile phase and a brookite phase, and of these three phases, anatase has been the most widely studied due to its high photocatalytic activity[79].

The anatase phase has a low-velocity recombination of photogenerated charges that allow it to be more photoactive and gives it great application potential in sensors, solar cells and catalytic devices and can also be used in disinfection applications such as air and water cleaning[74,80]. Rutile titania has lower photocatalytic activity and can be used in medical fields for scaffolding for tissue engineering as well as in cosmetic fields[80].

Titania nanofibers are semiconductors[74] and, as a result, the band gap of the decorated titania nanofibers can be determined[80]. The band gap of a material is the minimum amount of energy needed for an electron that is in a bound state to be promoted into a free state where it can be a conducting electron. TiO_2 has an intrinsic wide band gap (3.05 eV for the rutile phase) and 3.20 eV for anatase phase[81]. Due to their large band gap, titania nanofibers absorb light largely in the ultraviolet range and combining them with porphyrins expands their absorption into the visible region as well. Unlike other nanoparticles, nanofibers are advantageous as they can be easily removed and recovered from water post-treatment, which therefore means that their reusability can be explored. Nanofibers have a high surface area and porosity which makes them effective in water purification.

In this work, TiO_2 nanofibers are applied as support for the porphyrins. TiO_2 has photocatalytic bacterial activity[82], hence the combination of porphyrins and TiO_2 will enhance aPDI activity by synergistic effect, in addition to reducing the band gap. Electrospun nanofibers on their own show promising applications in water purification, wound-dressing materials, and biomedical devices[83]. Thus, the TiO_2 nanofibers containing porphyrins have potential applications in the areas stated above.

A previous attempt at enhancing the antimicrobial activity of TiO_2 nanofibers was reported by Soo et al.[84], where the nanofibers were coated with silver nanoparticles and applied against various gram-negative and gram-positive bacteria. Their research indicated a reduction of 3–4 log colony forming units (CFU) of Gram-negative bacteria and a reduction of 0.5–1.5 log CFU of Gram-positive bacteria. Upon increase in irradiation time and concentration of silver nanoparticles, these values were observed to increase up to 5.92 ± 0 and 1.38 ± 0.07 log CFU for gram-negative *Salmonella Albany* and the gram-positive *S. aureus* bacteria samples, respectively[84]. The data observed here further show the antimicrobial potential of decorated TiO_2 nanofibers. Table 1.3 shows some TiO_2 nanofiber composites previously utilised in antimicrobial applications[74,80-87]. Although composites of TiO_2 nanofibers have been applied against microorganisms, none containing Sn and In porphyrins have been reported.

Table 1.3: TiO_2 containing composite nanofibers applied previously against microorganisms.

Nanofiber composite	Application	Reference
Electrospun and blowspun Ag-TiO_2 nanofibers, polymeric Ag-TiO_2 nanoparticle-embedded nanofibers.	Antimicrobial activity was investigated against *S. aureus, E. coli, K. pneumoniae* and *E. faecalis*. Anticancer studies were performed against AT-84 cancer cells.	[78,84–88]
Electrospun TiO_2/ZnO composite nanofibers.	Antimicrobial activity was assessed against *E. coli* and *S. aureus*, Photodegraadation was investigated against methylene blue	[89,90]
Blowspun TiO_2-CeO_2 nanofibers	Antifungal properties of *C. albicans, C. glabrata*, and *C. krusei* were investigated.	[91]

1.3.1 FABRICATION OF TITANIUM DIOXIDE NANOFIBERS

There are different methods of fabrication of nanofibers including chemical synthetic methods such as chemical vapour deposition, hydrothermal, sol-gel, template-assisted synthesis, and microwave synthesis, electrochemical deposition, and physical synthetic methods such as mechanical milling, physical vapour deposition, laser ablation, and electrospinning[92].

Electrospinning is a technique that uses a high voltage to produce electrostatic forces that overcome cohesive forces to result in the production of fine fibers that are squeezed from a syringe with polymer solution[72]. Electrospinning is a versatile method of processing fibers as it can create different arrangements and morphological structures of fibers[93]. This can be done by adjusting the flow rate of the polymer solution, changing the voltage, and changing the diameter of the jet needle to produce desired fibers. Fig. 1.5 represents the electrospinning process.

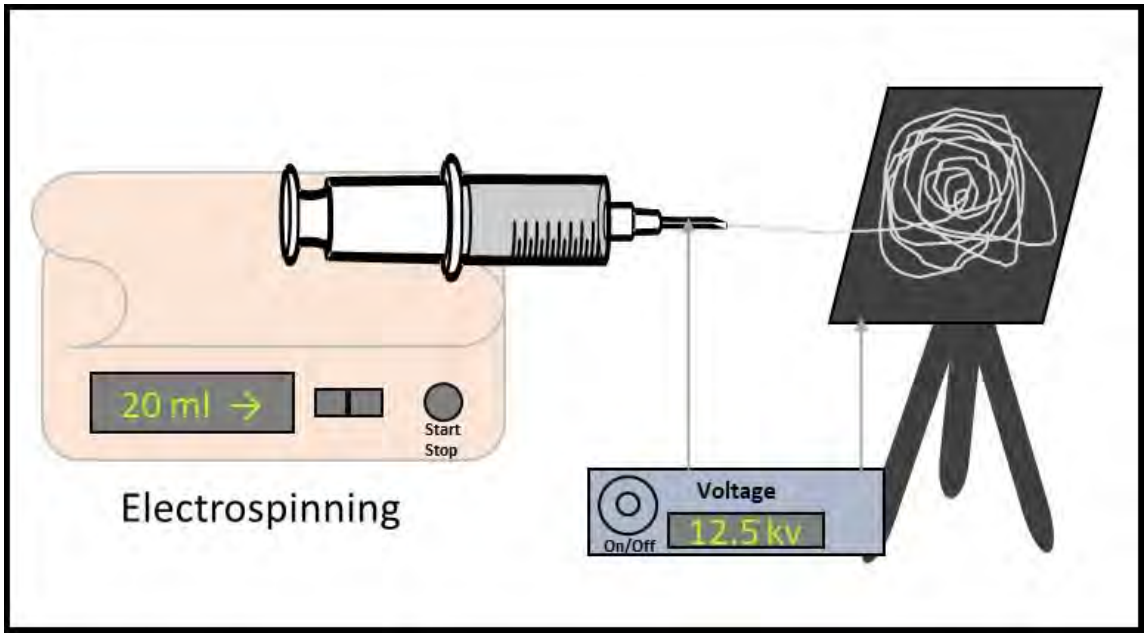

Figure 1.5: A diagram of a typical electrospinning setup.

The fibers are ideal as they have small pore sizes, high surface areas, and high porosity. Another advantage of using electrospun polymer for fiber formation is that different compounds can be added to the polymer solution in order to functionalise the fiber[72]. Fibers could be functionalised by incorporating drugs, nanoparticles or other functional materials[94,95], such that the nanofibers have extraordinary characteristics. Polymers are used extensively in the production of nanofibers. In this work, polyvinylpyrrolidone (PVP) was used as a sacrificial polymer[96] to create titania nanofibers. The polymer, which is later calcined, acts as a template that allows for the formation of the fibrous nanostructures.

1.3.2 MECHANISM OF ACTION OF PORPHYRIN DYED TiO_2 NANOFIBERS

The photocatalytic activity of metal oxide photocatalysts relies on energy absorption from a light source, as depicted in Fig. 1.6.

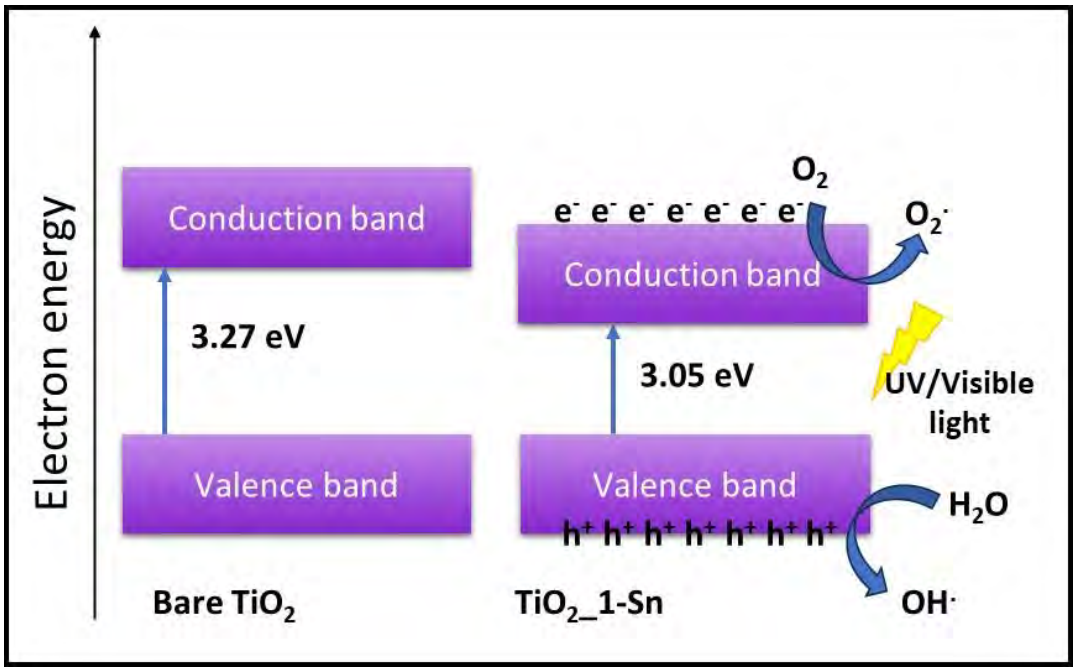

Figure 1.6: Mechanism of action to which metal oxides photocatalysts along with the reduction of band gap post dying with porphyrin dyes.

Upon excitation with light, electrons are transferred from a valence band to a conduction band leaving behind some positively charged holes that form electron-hole pairs. The pairs can migrate to the surface of the material where hydroxyl radicals, singlet oxygen, superoxide radical, and hydrogen peroxide[97] are formed from molecular oxygen present in the environment. ROS are produced and therefore induce an antimicrobial effect by directly interacting with the cells and disrupting their growth[98] by damaging their cell membrane or by cell diffusion of hydrogen peroxide that has been reported to cause disturbances and damage within the microbial cell[98–100]. The production of ROS by the nanofibers together with the production of singlet oxygen species by the porphyrins create a synergistic effect that aids in the inactivation of microbes.

1.3.3 SINGLET OXYGEN PRODUCTION OF PORPHYRIN-NANOFIBER CONJUGATES

Post-adsorption of porphyrins onto the nanofibers, Φ_Δ was determined to assess the production of $^1O_2$ of the conjugates[101].

For the determination of the Φ_Δ on the nanofibers, the direct chemical method was used due to lack of a standard[102]. The anthracene-9,10-diyl-bis-methylmalonate (ADMA) was used as a singlet oxygen quencher in water. The nanofibers were immersed in solution and irradiated using the photolysis set-up similar to the one used

for the porphyrins, where samples were irradiated at 5 min intervals for 35 min. The extinction coefficient of ADMA (ε = 12589[103]) at 380 nm was used.

Eq. 1.3 was first used to calculate the quantum yield of ADMA (Φ_{ADMA}).

$$\Phi_{ADMA} = \frac{(C_0 - C_t) \times V_R}{I_{Abs}.t} \tag{1.3}$$

Where C_o and C_t represent the concentrations of ADMA before and after irradiation, respectively; V_R is the volume of the solution; t is the irradiation time per cycle and I_{Abs} is defined by Eq. 1.4.

$$I_{abs} = \frac{\alpha A I}{N_A} \tag{1.4}$$

where $\alpha = 1\text{-}10^{-A(\lambda)}$, $A(\lambda)$ is the absorbance of the sensitizer at the irradiation wavelength, A is the irradiated area (2.5 cm^2), I is the intensity of light (6.63×10^{16} photons cm^{-2} s^{-1}) and N_A is Avogadro's constant. The absorbance used for eq.1.4 is that of the porphyrin on the nanofiber. The light measured refers to the light reaching the spectrophotometer cell, and it is expected that some of the light may be scattered, hence the values of the porphyrin on the nanofibers are estimates.

Subsequently, the Φ_Δ of the respective materials was calculated using Eq. 1.5,

$$\frac{1}{\Phi_{ADMA}} = \frac{1}{\Phi} + \frac{1}{\Phi} \cdot \frac{K_d}{K_a} \cdot \frac{1}{[ADMA]} \tag{1.5}$$

where K_a is the rate constant for the reaction of ADMA with $^1O_2$ ($^1\Delta_g$) and K_d is the singlet oxygen decay constant.

Chapter 2

Experimental Section

This chapter details the equipment, materials and methods used to synthesise and characterise porphyrins, the fabrication and characterisation of nanofibers, and the porphyrin-nanofiber conjugates.

2.1. EQUIPMENT

- Ultraviolet-visible (UV-vis) optical absorption spectroscopy in solution was recorded using a Shimadzu UV-2550 spectrophotometer.
- Solid-state ultraviolet-visible (UV-vis) optical absorption spectroscopy were recorded using a Perkin-Elmer Lambda 950 UV-vis spectrometer.
- Mass spectral analysis was performed using Brucker AutoFLEX III smartbeam TOF/TOF Mass spectrometer using a positive ion mode. Alpha-cyano-4-hydroxycinnamic acid as was used as the MALDI matrix.
- ^{1}H NMR was conducted on a Bruker 80 MHz Benchtop NMR. The parameters were set at a dummy scan (DS) of 2 with a scan rate of 256 per sample. Deuterated chloroform ($CDCl_3$) and Dimethyl sulfoxide (DMSO-d6) were used as solvents for the samples.
- Fluorescence emission spectra were recorded on a Varian Eclipse spectrofluorometer.
- Fluorescence lifetimes were measured using a time-correlated single photon counting setup (TCSPC), Fluo Time 200, Picoquant GMbH, with a diode laser as the excitation source (excitation source: LDH-P-420 and 380 nm with 10 MHz repetition rate for porphyrin). Fluorescence was detected under the magic angle with a Peltier cooled photomultiplier tube (PMT) (PMA-C 192-N-M, Picoquant GmbH) and integrated electronics (PicoHarp 300E, Picoquant GmbH). A monochromator with a spectral width of about 4 nm was used to select the required measured emission wavelength. The response function of the system, which was measured with a scattering Ludox solution (DuPont), had a full width at half-maximum (FWHM) of about 300 ns. The ratio of stop-to-start pulses was kept low (below 0.05) to ensure good statistics. All

luminescence decay curves were measured at the maxima of the emission peak. The data were analysed with the program FluoFit (Picoquant GmbH). The support plane approach was used to estimate the errors of the decay times.

- Triplet state lifetimes were determined in nitrogen saturated dimethyl sulfoxide (DMSO) solutions at 500 nm, using an Edinburgh Instruments LP980 spectrometer and a pump beam of 425 nm provided by an Ekspla NT-342B laser fitted with an OPO (2.0 mJ/7 ns, 20 Hz).
- X-ray diffraction (XRD) was conducted using a Bruker D8 Discover instrument.
- Photo-irradiations for singlet oxygen studies and antimicrobial photodynamic inactivation studies were done using a broad-spectrum halogen lamp (range 350 nm to 3500 nm, centred at 552 nm). The irradiation was at the crossover wavelengths between the sample and the standard.
- Fourier transform infra-red (FTIR) spectroscopy data were recorded using a Bruker Alpha model FT-IR spectrometer with a platinum-ATR.
- Nanofibers were electrospun using a KD Scientific 1-channel syringe pump. The nanofibers were calcined in a Labotec PRECISION furnace set at a temperature-increasing rate of 10 ℃ per minute.
- Scanning Electron Microscopy (SEM) samples were gold-plated and analysed in a Vega Tescan Instrument. The SEM images were taken with the following parameters - SEM HV: 20.00 -kV, WD: 21.56- 22.09 mm, SEM MAG: 4. 26-4.35 kx and a scale of 5 µm, other samples were carbon coated and analysed on a JSM_7800F JEOL JEM-2100.
- For aDPI application studies, bacterial optical density was determined using an AFEXIM Products LED optical density reader. Colony forming units (CFU/mL) counting was performed using an Interscience Scan® 500 plate reader. The

illumination studies were conducted using a broad-spectrum halogen lamp connected to a YOKOYAMA ELECTRIC WORKS LTD. *Variable V*. voltaic transformer set at 70 kW

2.2 MATERIALS

2.2.1 Porphyrins synthesis and characterisation

N,N-dimethylformamide (DMF), dimethyl sulfoxide (DMSO), silica, chloroform, acetonitrile, Zn 5,10,15,20-tetraphenyl-21H,23H-porphyrin (ZnTPP), 9,10-dimethylanthacene (DMA), and 9,10-antracenediyl-bis(methylene)dimalonoic acid (ADMA) NaOH, propionic acid, tin(II) chloride, silica, p-anisaldehyde, 4-(methylthio)benzaldehyde, pyridine, and pyrrole, which was distilled before use, were purchased from Sigma Aldrich. The listed materials were used for the synthesis, purification and characterisation of porphyrins.

2.2.2 Nanofiber fabrication

Polyvinylpyrrolidone (PVP) (mw: 1 300 000 g/mol), ethanol, titanium isopropoxide, glacial acetic acid used for the fabrication of nanofibers were all purchased from Sigma Aldrich.

2.2.3 aPDI studies

The following were used for the preparation of bacterial solutions and aPDI studies.

S. aureus (ATCC 25923) was purchased from Microbiologic USA. *E. coli* (ATCC 25922*)* and *C. albicans* (ATCC 24433) were purchased from Davies Diagnostics. Agar bacteriological BBL Muller Hinton broth and nutrient agar were obtained from Merck. Phosphate buffer saline (PBS, 10 mM PBS, pH 7.4) was prepared using appropriate amounts of Na_2HPO_4, KH_2PO_4, KCl and NaCl, which were all purchased from Sigma Aldrich. Highly purified water was obtained through an installed water purifying system from ELGA, Veolia water PURELAB, and flex system (Marlow, UK).

2.3 METHODS

The syntheses of tetrakis (4-methoxy)phenyl porphyrin (**1**)[54], Cl_2Sn(IV) tetrakis(4-methoxy)phenyl porphyrin (**1-Sn**)[55,56], ClIn(III) 5,10,15,20-tetrakis(4-(methoxy)phenyl porphyrin (**1-In**)[58] and Cl_2Sn(IV) 5,10,15,20-tetrakis(4-(methylthio)phenyl porphyrin (**2-Sn**)[59] have been reported before.

2.3.1 Synthesis of porphyrins

Synthesis of 5,10,15-tris(4-methoxyphenyl)-20-(4-(methylthio)phenyl) porphyrin (Complex 3)

P-anisaldehyde (0.408 g, 0.003 mol) and 4-(methylthio) benzaldehyde (0.152 g, 0.001 mol) were dissolved in propionic acid (150 mL) and were heated to reflux. Pyrrole (0.004 mol, 0.278 mL) was then slowly added dropwise, and the mixture was left to reflux for 4 h. After refluxing, the mixture was cooled to room temperature before a solution of sodium hydroxide (5 M, 25 mL) was added to precipitate the porphyrin. The porphyrin was then filtered out, washed with Millipore water, dried and purified by column chromatography in a silica column with chloroform as an eluent to obtain clear

purple crystals of free base 5,10,15-tris(4-methoxyphenyl)-20-(4-(methylthio)phenyl) porphyrin (complex **3**).

Yield: 22.5%. FTIR (cm^{-1}): 3279 (N-H pyrrole), 2925 (C-H aromatic), 2831 (C-H alkyl), 1514 (C=C aromatic). MALDI TOF-MS, calc 750.27, found 750.45 $[M]^+$. UV/visible (DMF), λ_{max} nm (log ε): 424 (5.40), 517 (4.00), 555 (3.90), 593 (3.70), 650 (3.54). ^1H NMR (80 MHz, DMSO-d_6) δ 8.86 (s, 2H pyrrole), 8.13 (d, J = 7.9 Hz, 4H aromatic), 7.39 (d, J = 8.3 Hz, 6H aromatic), 7.08 (d, J = 7.9 Hz, 6H aromatic), 6.99 – 6.59 (m, 6H pyrrole), 4.05 (s, 9H methoxy), 3.84 (s, 3H methoxy), 2.08 (s, 1H amine), -2.90 (s, 1H amine).

Synthesis of Cl_2Sn(IV) 5,10,15-tris(4-methoxyphenyl)-20-(4-(methylthio)phenyl) porphyrin (Complex 3-Sn)

Complex **1** was metallated with tin(II) chloride as follows: complex **3** (0.15 g, 0.2 mmol) and tin (II) chloride (0.19 g, 0.0007 mol) were refluxed in pyridine (20 mL) for 4 h. After refluxing, deionised water was added to the mixture, filtered and then washed with water to wash out the pyridine. A green powder was obtained and flushed with chloroform through a silica column to obtain a pure Cl_2Sn(IV) 5,10,15-tris(4-methoxyphenyl)-20-(4-(methylthio)phenyl) porphyrin (complex **3-Sn**).

Yield: 87.5%. FTIR (cm-1): 2925 (C-H aromatic), 2848 (C-H alkyl), 1607 (C=C aromatic). MALDI TOF-MS: calc. 938.09, found 904.51 M-Cl+2H]$^+$. UV/visible (DMF), λ_{max} nm (log ε): 434 (5.13), 566 (4.88), 609 (3.85). ^1H NMR (80 MHz, $CDCl_3$) δ 9.22 (s, 2H pyrrole), 8.18 (s, 2H aromatic), 7.98 (d, J = 8.7 Hz, 4H aromatic), 7.27 (s, 6H aromatic), 7.07 (s, 4H aromatic), 6.93 (d, J = 5.1 Hz, 6H pyrrole), 4.14 (s, 3H methoxy), 3.84 (s, 9H methoxy).

2.3.2 Preparation of nanofibers

TiO_2 nanofibers were fabricated following the reported method[104] with modifications. Polyvinylpyrrolidone (PVP, 10%) (mw ~ 1 300 000) solution was made by adding 1 g to ethanol (10 mL). A titanium dioxide solution was created by adding glacial acetic acid (5 mL) to titanium isopropoxide (10 mL). The titanium dioxide solution was added dropwise to the PVP solution and stirred gently for 4h to obtain a homogenous mixture. The PVP/titanium dioxide solution was electrospun at room temperature (23℃), with a humidity of 35% at a rate of 1.5 mL/h. The voltage was set to 12.5kV, and at a 15 cm distance between the anode and cathode. An aluminium foil collector was employed. The electrospun fibers were then cut into 1.5 cm squares and calcined at a heating rate of 10 ℃/min up to 650 ℃ and 750 ℃ for 4 h to yield purely inorganic TiO_2 nanofibers that are in a mixed anatase/rutile or purely rutile phase, respectively. Pure inorganic nanofibers were submerged into prepared porphyrin solutions (200 μM in a 1:1 acetonitrile: chloroform). The nanofibers were left to soak for 24 h, washed with 70% ethanol, and dried in air overnight. Fig. 2.1 represents the dying process of the nanofibers with porphyrins to give TiO_2 **_1**, TiO_2 **_3,** TiO_2 **_1-Sn**, TiO_2 _1-In and TiO_2**_2-Sn**, and TiO_2**_3-Sn**.

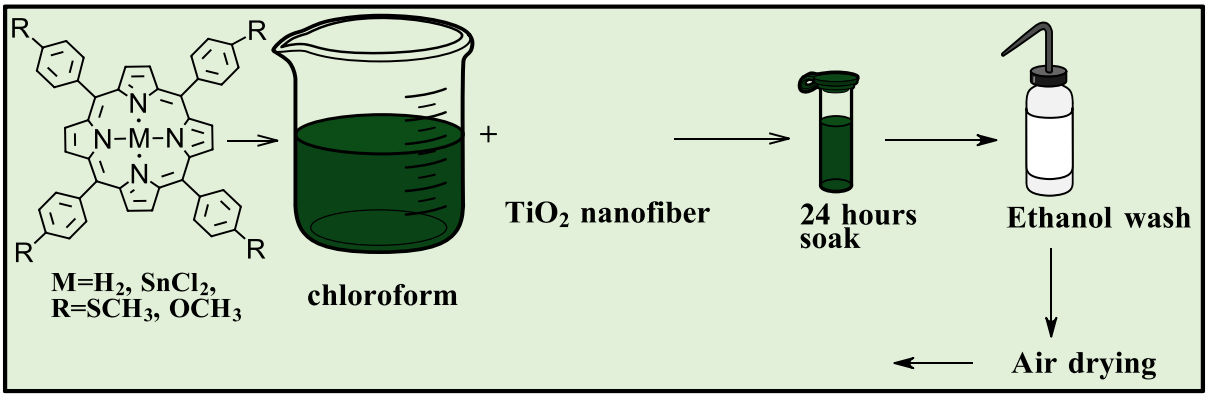

Figure 2.1: The adsorption of porphyrins on electrospun TiO_2 nanofibers

2.3.3 Preparation of bacterial cultures

The *staphylococcus aureus*, *Escherichia coli* and *Candida albicans* microbial cultures were prepared according to a method previously reported in the literature[105]. Briefly, aliquots of the culture were aseptically transferred to 6 mL of fresh broth and incubated at 37 °C to mid-logarithmic phase (absorbance ~ 0.6 at 620 nm). The microorganism culture in the logarithmic phase of growth were harvested through the removal of broth culture by centrifugation (3000 RPM for 15 min), washed three times with 10 mM of PBS and re-suspended in 1 mL of PBS. The microorganism culture was then diluted to 1/100 in PBS (working stock solution), corresponding to 10^8 colony-forming units (CFU)/mL.

2.3.4 aPDI studies

aPDI studies were performed by administration of appropriate concentrations of porphyrin complexes in DMF (1% or 5%) /PBS to a bacterial suspension of 10^8 CFU/mL. The bacterial suspensions were incubated in an oven equipped with a shaker for 30 min in the dark at 37 °C to allow for localisation of the porphyrins into the bacterial cells. Post localisation, the bacterial solutions treated with porphyrin were irradiated in an irradiation chamber for a period of up to 2 h with a broad-spectrum halogen lamp, before inoculating 100 µL onto nutrient agar plates, in triplicates. The plates were then incubated at 37 °C for 18-24 h. The same was done for the nanofiber conjugates, where 5/20 mg of solid porphyrin-dyed nanofibers were placed in the bacterial suspensions, irradiated for 1-2 h and then treated as mentioned, as can be seen in Fig. 2.2.

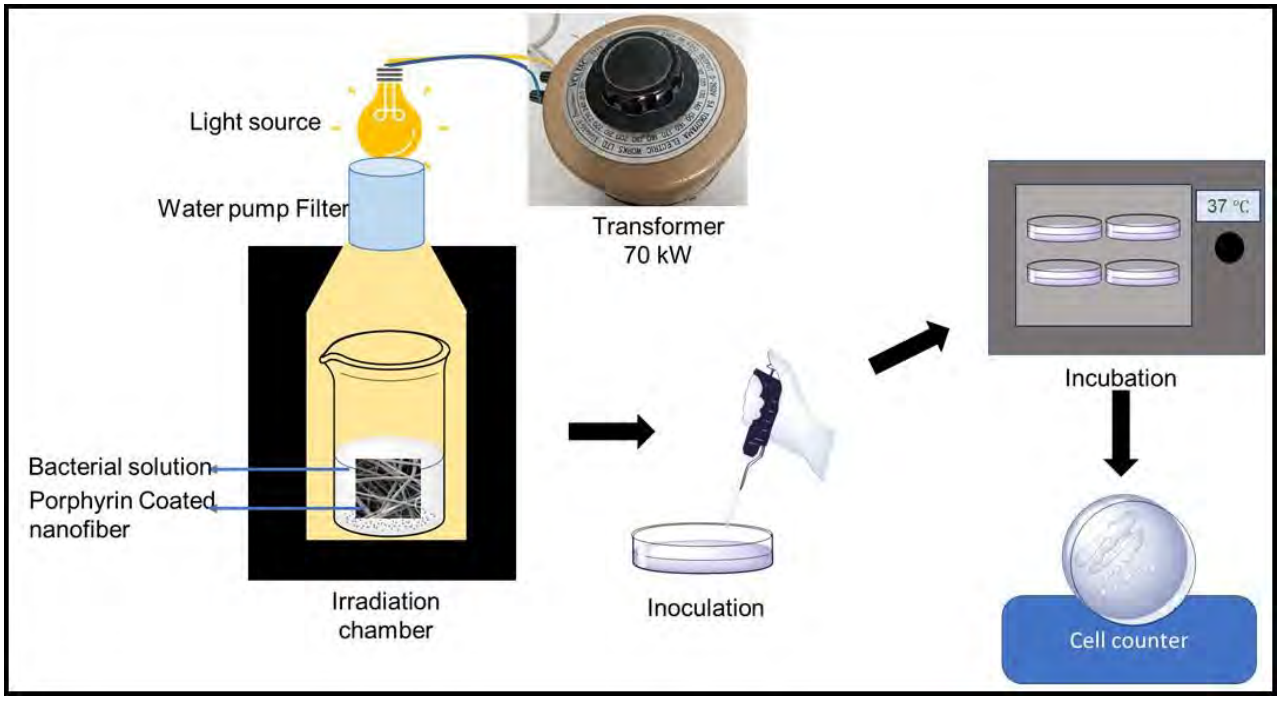

Figure 2.2: Summarised diagram showing the steps observed to carry out the aPDI procedure.

RESULTS AND DISCUSSION

Publications

Some of the work present in this thesis was reported in the following publication:

1. K. Hlabangwane, R. Matshitse, M. Managa, T. Nyokong. The application of Sn(IV)Cl_2 and In(III)Cl porphyrin-dyed TiO_2 nanofibers in photodynamic antimicrobial chemotherapy for bacterial inactivation in water. *Photodiagnosis Photodyn. Ther.,* **2023** *44,* 103795. https://doi.org/10.1016/j.pdpdt.2023.103795
2. K. Hlabangwane, A. Sindelo, M. Managa, and T. Nyokong, Investigation of Antimicrobial Photodynamic Inactivation Effect of Porphyrins Adsorbed onto Rutile TiO_2 Nanofibers. *J. Coord. Chem*. Submitted 19-11-2024.

Chapter 3

Characterisation

Different techniques were used to characterise the porphyrin, the nanofibers, and the porphyrin-dyed nanofibers conjugates to confirm their successful synthesis and fabrication. This chapter explores these characterisation techniques and discusses the data obtained.

3.1. CHARACTERIZATION OF THE PORPHYRINS

The complexes were characterized using MALDI-TOF mass spectra, ultraviolet-visible UV–vis spectroscopy, and ^{1}H NMR spectroscopy.

3.1.1 MALDI-TOF mass spectrometry

Mass spectral analysis was used to assess the successful formation of porphyrins as well as the successful metallation of complex **3** to form complex **3-Sn**.The syntheses of complexes **1, 2-Sn 1-Sn** and **1-In**[54–59] have been reported and expected results were obtained. The structures of the complexes are shown in Fig. 3.1.

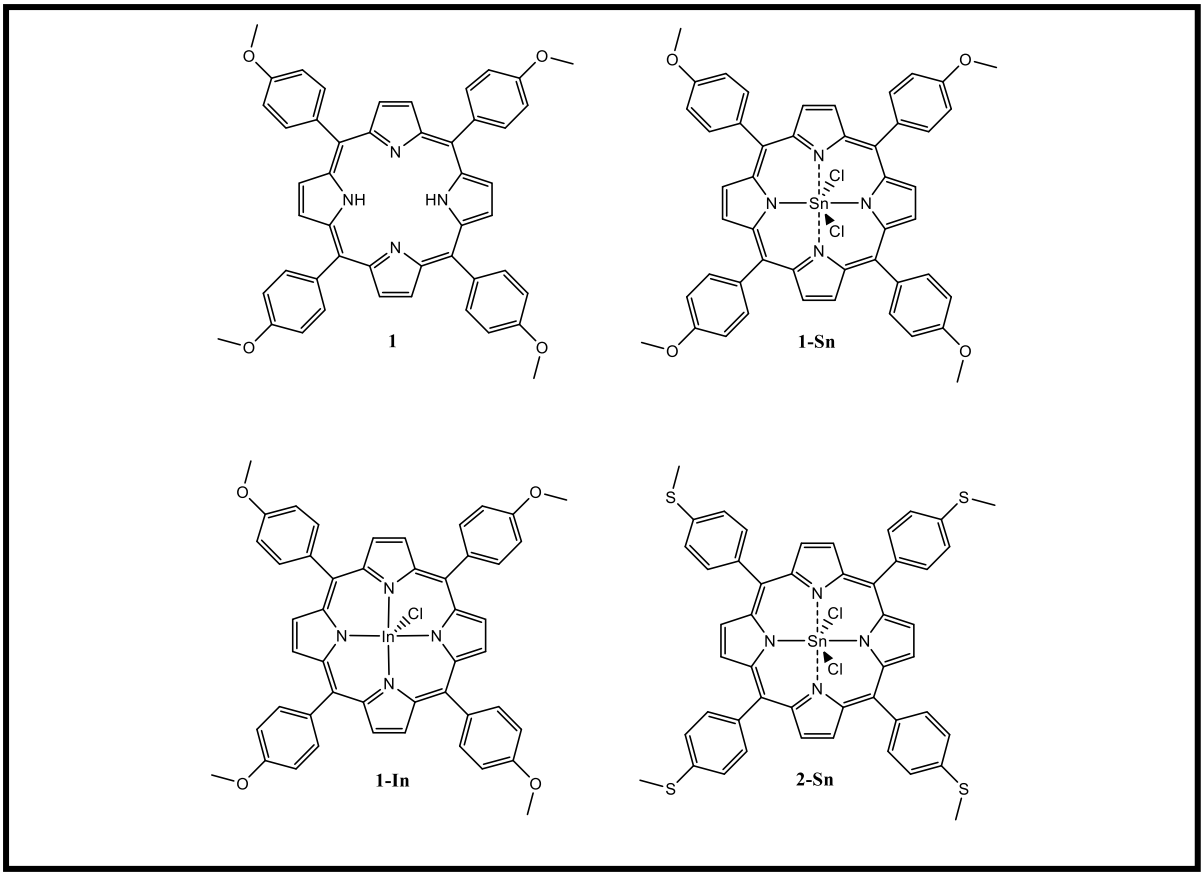

Figure 3.1: Schematic diagrams of Complexes **1**, 1-**Sn**, **1-In**, and **2-Sn** used in this work.

The expected mass for complex **1-Sn** was calculated to be 922.45 amu and the mass obtained was 887.53 amu, Fig. S1 (a) (Supporting Information). The expected mass and obtained mass difference is 34.92 amu, which is consistent with the mass of one chlorine atom. Two peaks were observed for complex **1-In**, the expected mass was calculated to be 883.11 amu and the peak at 884.87 amu is assigned to $[M+H]^+$ (Fig. S1 (b), Supporting Information). The second peak observed at 850.20 amu for complex **1-In** has a mass of 32.91 amu, also consistent with the mass of fragmented chlorine and 2 hydrogen atoms $[M-H]^+$. Scheme 3.1 shows the synthetic pathway towards formation of asymmetrically substituted complexes **3**, and **3-Sn**.

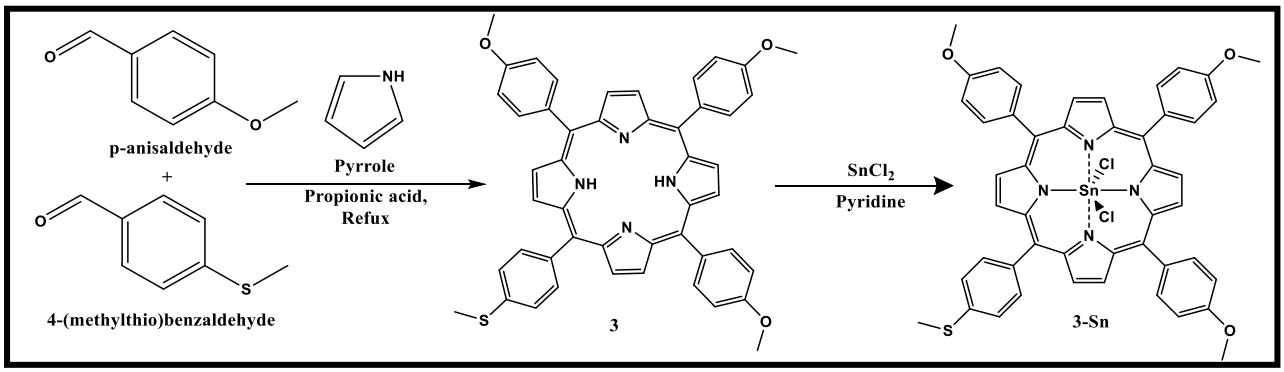

Scheme 3.1: Synthesis of complexes **3** and **3-Sn**.

The mass spectrum in Fig. 3.2 shows the expected mass for complex **3,** which was calculated to be 750.27 amu and found to be 750.45 amu. The obtained mass of complex **3-Sn** of 904.51 $[M-Cl+2H]^+$ amu, is indicative of fragmented chlorine atoms and additional protons.

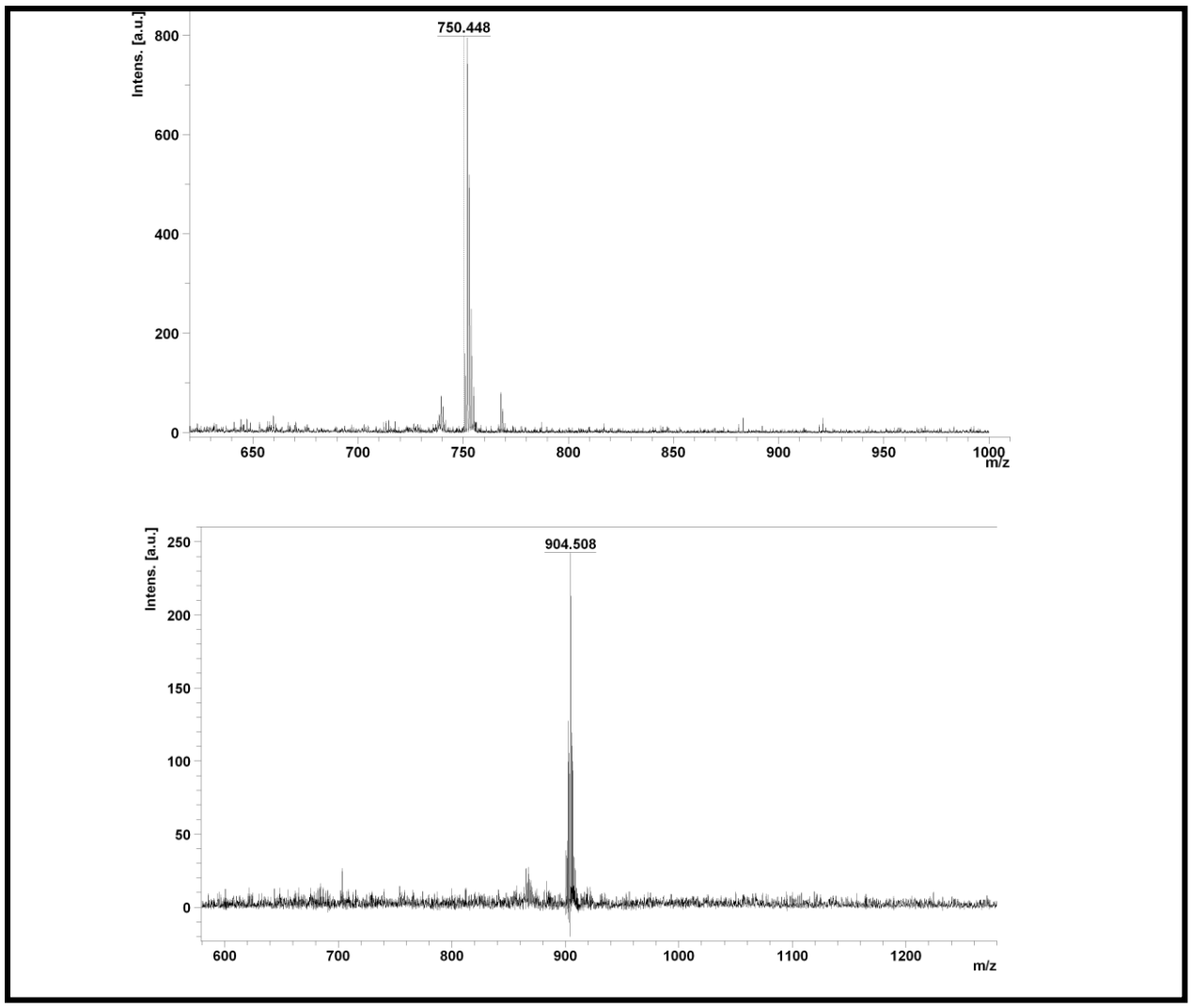

Figure 3.2: MALDI-TOF Mass spectrometry of compounds **3** (top), **3-Sn** (bottom)

3.1.2 Proton Nuclear Magnetic Resonance

Proton NMR of complexes **3** and **3-Sn** (Supporting information Fig. S2) shows all expected protons for both complexes. The spectra also indicated extra peaks that could be attributed to excess solvent peaks (propionic acid) as well as grease peaks from the instrument at 0.5-1.75 ppm and 0.5-2.0 ppm[106,107] for complexes **3** and **3-Sn** respectively.

3.1.3 Ultraviolet-Visible Spectroscopy

Ultraviolet-Visible (UV-Vis) spectroscopy, recorded in dried DMF, showed successful syntheses of the porphyrins, where the four Q-bands of complexes **1**, **2** and **3**, typical of free base porphyrins[33] merged into two, indicating successful metallation of complexes **1-Sn**, **1-In**, **2-Sn** and **3-Sn**, Fig. 3.3.

There is a notable red shift in the Soret band of the metallated porphyrin where the peak shifts from 424 nm of free base complex **3** to 434 for complex **3-Sn**, Table 3.1, and Fig. 3.3. The introduction of heavy metals results in a degree of perturbation and electron delocalisation within the porphyrin macrocycle, resulting in a red shift of the Soret band[33].

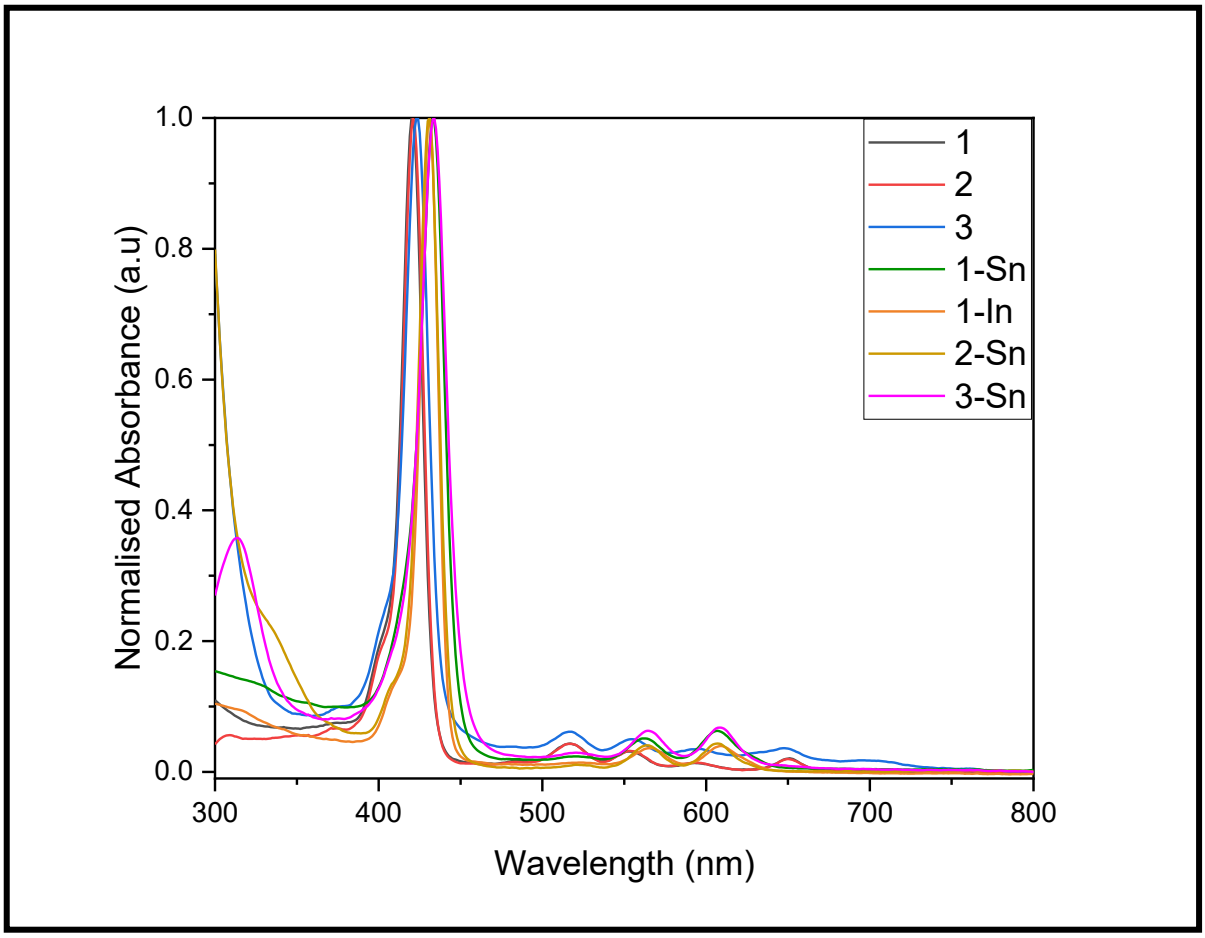

Figure 3.3: UV-Vis spectra of complexes **1**, **2**, **3**, **1-Sn**, **1-In**, **2-Sn** and **3-Sn**

Complexes **1-Sn** and **3-Sn**, both containing methoxy groups display a larger red shifted than complex **2-Sn**, Table 3.1. This could be due to the electron-donating nature of the methoxy group. Electron-donating substituents lead to redshifts in the Soret band[108].

The red shift is an advantage in this work as it results in the increase of light absorption into the visible range.

3.1.4 Fluorescence Emission Spectroscopy

Emission spectroscopy was used to determine the fluorescence of complexes **1**,**2, 3, 1-Sn, 1-In, 2-Sn** and **3-Sn**, and the emission spectra obtained are presented in Fig. 3.4. Two peaks are observed as is typical of porphyrins[108–110]. The emission bands of **1** peak at 658 and 722 nm while those of **1-Sn** were at 623 and 676 nm, and for **1-In** at 625 and 673.

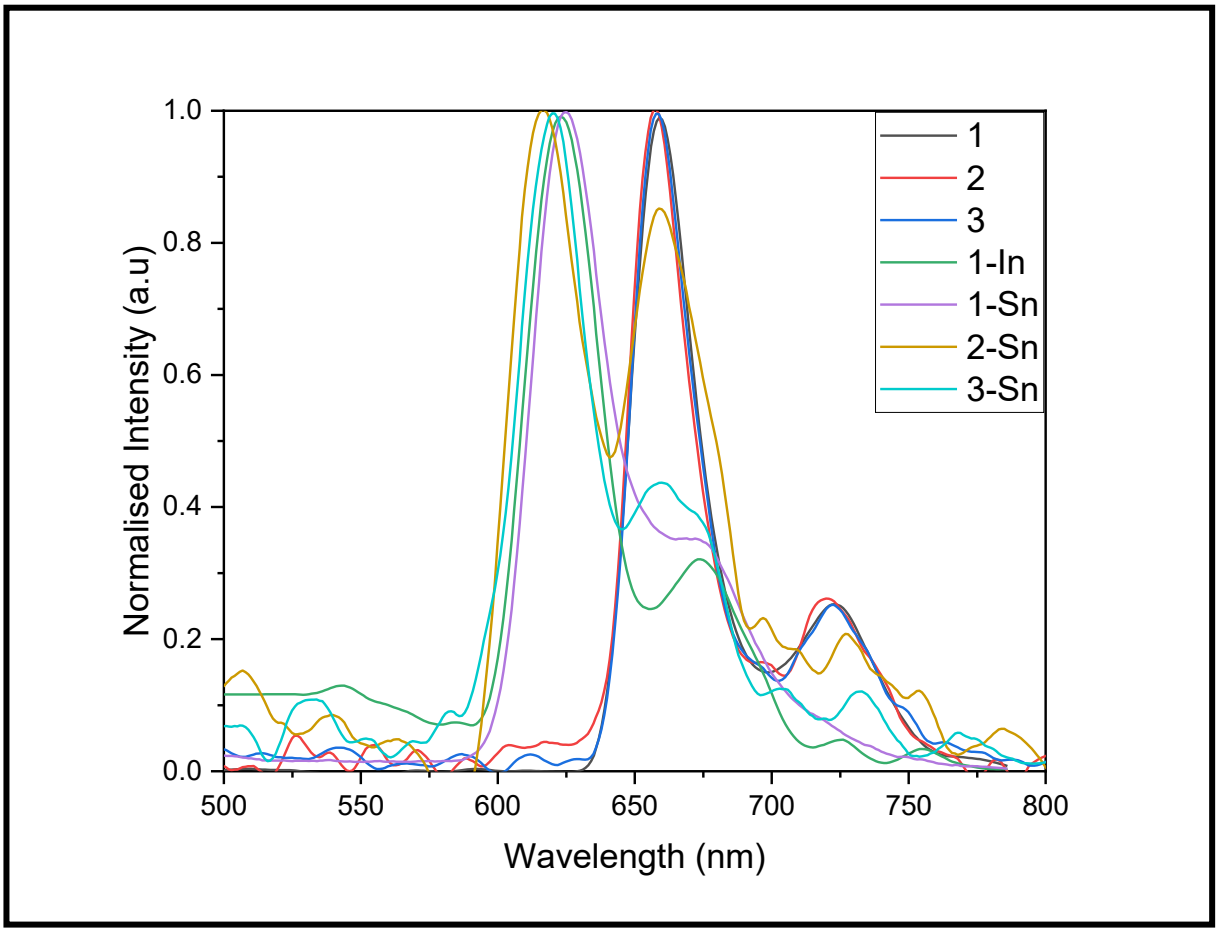

Figure 3.4: Fluorescence emission spectroscopy of porphyrin complexes **1**, **2**, **3**, **1-Sn**, **1-In**, **2-Sn**, and **3-Sn.**

Table 3.1: Summary of Uv-Vis peaks of porphyrin complexes alone or when adsorbed onto TiO_2 nanofibers in DMF unless otherwise stated. TiO_2 refers to mixed-phase anatase and rutile nanofibers, while *r*TiO_2 refers to purely rutile nanofibers.

Complexes	λ(nm) Soret band[a]	λ(nm) Q-bands[a]
1	420	516, 553, 593, 650
1-Sn	433	562, 605
1-In	431	565, 608
2	421	516, 553, 593, 650
2-Sn	429	563, 606
3	424	517, 555, 593, 650
3-Sn	434	566, 609
TiO_2_**1-Sn**	(446)	(572; 616)
rTiO_2_**1-Sn**	(444)	(570; 614)
TiO_2_**1-In**	(431)	(566; 609)
rTiO_2_**2-Sn**	(433)	(562, 608)
rTiO_2_**3**	(427)	(522, 556, 590, 651)
rTiO_2_**3-Sn**	(435)	(565, 609)

[a] values in brackets are for the solid state.

3.2 CHARACTERISATION OF NANOFIBERS AND PORPHYRIN ADSORBED NANOFIBERS

TiO_2 nanofibers and porphyrin-adsorbed TiO_2 nanofibers were characterised using solid-state ultraviolet-visible spectroscopy, X-ray diffraction, Fourier transform infrared spectroscopy (FT-IR), thermogravimetric analysis (TGA) and scanning electron microscopy (SEM).

3.2.1 Solid state UV-Vis spectra

Complexes **1-Sn** and **1-In** were dyed and studied on a mixture of anatase/rutile TiO_2 (represented as TiO_2) nanofibers. The UV-Vis spectra in the solid state, Fig. 3.5 (A) show the successful adsorption of complexes **1-Sn** and **1-In** dyes to the mixed rutile/anatase titania nanofibers, where the spectra of the dyed nanofibers show the absorption peaks consisting of Q-bands at 572 nm and 616 nm for TiO_2_**1-Sn**, and at 566 nm and 609 nm for TiO_2-**1-In** and the Soret band peaks are at 446 nm and 431 nm for TiO_2-**1-Sn** and TiO_2_**1-In**, respectively, Table 3.1. Fig. 3.5 (B) shows the adsorption of complexes **3, 1-Sn 2-Sn** and **3-Sn** onto purely rutile TiO_2 nanofibers (represented as *r*TiO_2), where similar to the mixed anatase/rutile nanofibers the adsorption of the porphyrins was successful. The peak observed in the bare TiO_2 nanofibers in Fig. 3.5 peaks near 350 nm and is typical of titanium dioxide[111] absorption spectra. When compared to the in-solution UV-Vis (Table 3.1) the Soret peaks and Q-bands typical of porphyrins, appear broader due to aggregation in solid state[112]. A red-shift of the peaks was also noted (Table 3.1) and is also typical of the porphyrin-type complexes in the solid state[112].

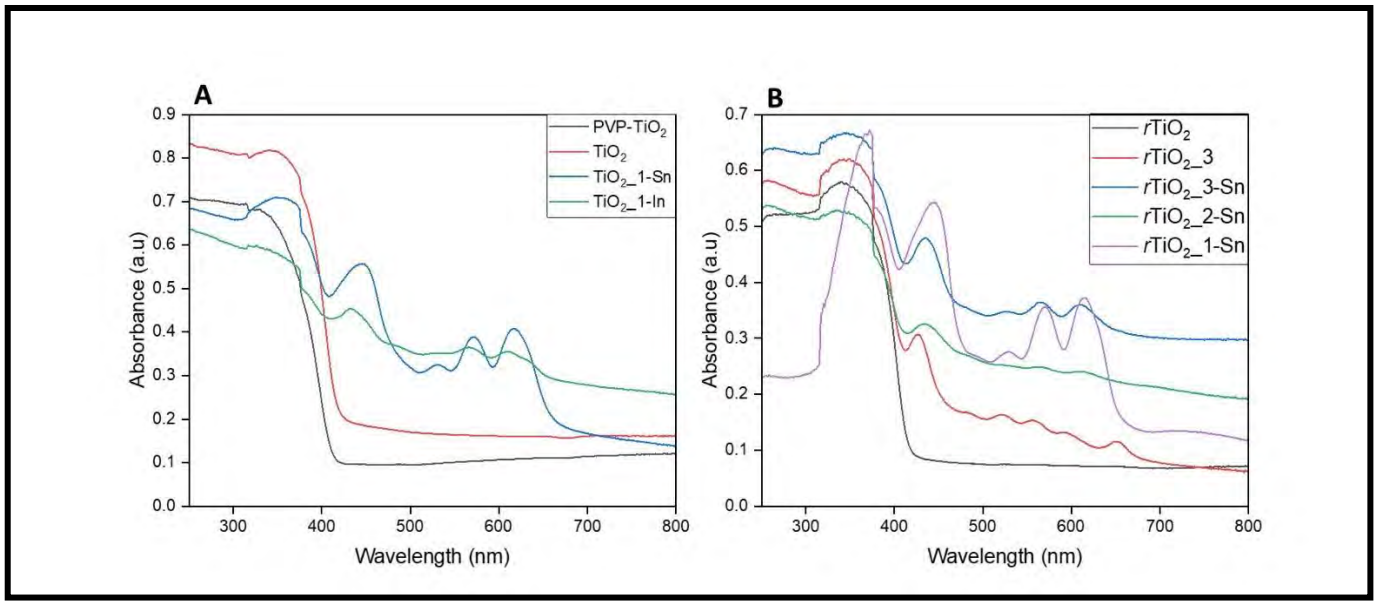

Fig. 3.5: Solid-state UV-Vis spectra of mixed anatase/rutile nanofibers (A) before and after adsorption with complexes **1-Sn** and **1-In**, and purely rutile TiO_2 (*r*TiO_2) (B) before and after adsorption of porphyrin complexes **3, 1-Sn 2-Sn** and **3-Sn**.

The titania peaks in Fig. 3.5 were also used to assess the changes in band gap of titania upon introduction of the nanofibers and the results of these can be found in Table 3.2. The band gap of TiO_2 nanofibers alone and with porphyrins was determined using Tauc's equation (Eq. 3.1)[113], and the plot is represented in Fig. 3.6 for TiO_2 alone (similar Tauc plots were used to determine the band gap energies of the porphyrin-containing nanofibers),

$$(ahv)^{1/n} = k(hv - Eg) \qquad (3.1)$$

where α is the absorption coefficient, *h* is Planck's constant, v is the photon's frequency, Eg is the band gap energy and k is a proportionality constant. The value of n in the exponent is an indication of the nature of the electronic transition that occurs

in the TiO_2 nanofibers[114]. In this case, direct allowed transitions[115] were studied so n=1/2.

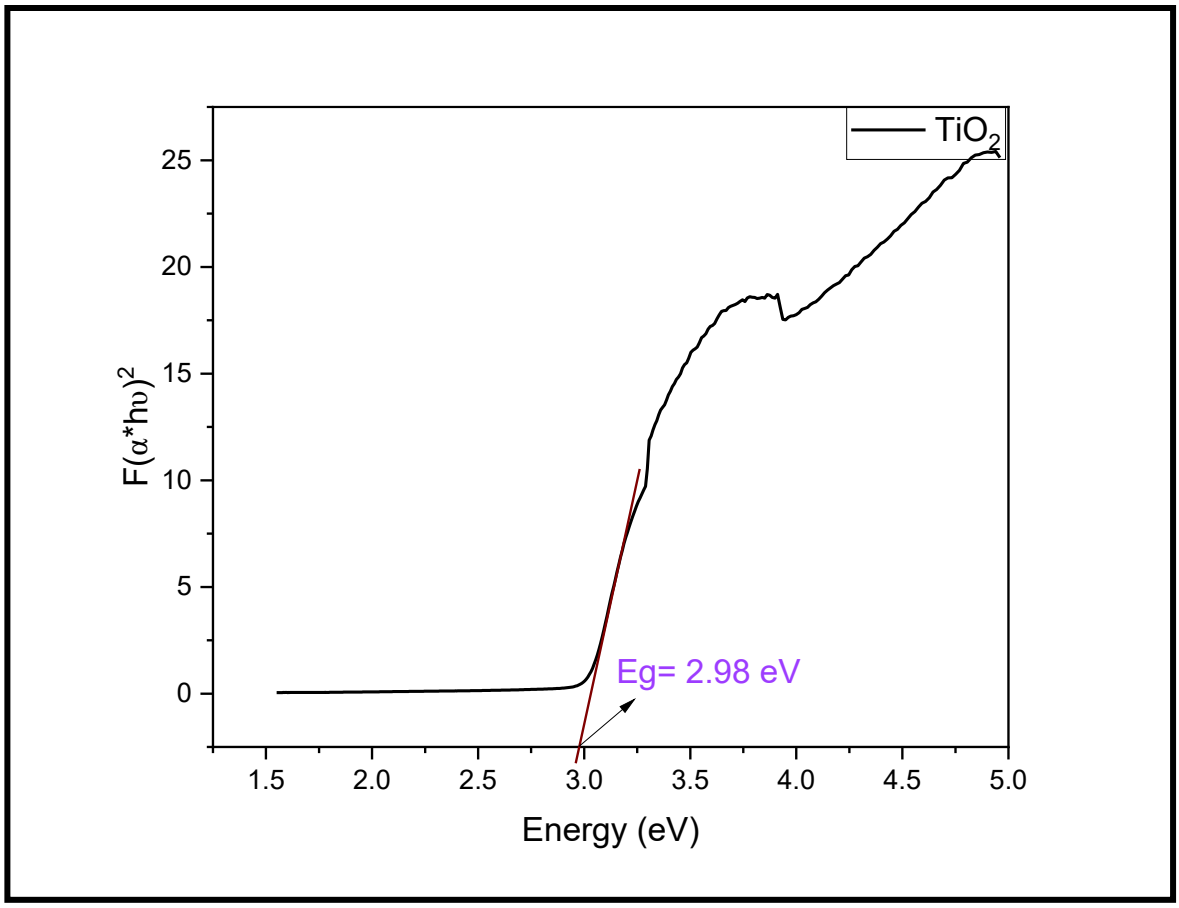

Figure 3.6: An example of the Tauc plot (*r*TiO_2) used to determine the nanofibers' band gap energies.

Table 3.2: Band gap and loading values of TiO_2 nanofibers after adsorption with porphyrins.

Sample	Band Gap energies (eV)	Porphyrin loading (%)	SEM sizes (nm)
PVP/TiO_2	3.91	-	665 ± 140
TiO_2	3.27	-	515 ± 86
TiO_2 _**1-Sn**	3.05	4.87	481 ± 82
TiO_2 _**1-In**	3.06	3.68	481 ± 82
rTiO_2 (Rutile)	2.98	-	382 ± 9.09
rTiO_2 _**3**	2.84	1.85	380 ± 10.29
rTiO_2 _**1-Sn**	2.75	5.86	321.45 ± 5.30
rTiO_2 _**2-Sn**	2.76	5.90	321.45 ± 5.30
rTiO_2 _**3-Sn**	2.74	4.35	321.45 ± 5.30

The band gap energy of the mixed anatase/rutile TiO_2 was calculated to be 3.27 eV, similar to the previously reported literature value[74], while the pure rutile TiO_2 (*r*TiO_2) was calculated to be 2.98 eV, similar to the literature-reported value of 3.0 eV[76,116]. The band gap values of the nanofibers narrowed upon adsorption with the porphyrins, with TiO_2_**1-Sn** and *r*TiO_2 _**3-Sn** nanofibers having the lowest band gaps of 3.05 and 2.74 respectively. Rutile titania has been reported to have lower band gap energies[74], thus explaining the lower energies calculated for *r*TiO_2 and dyed their counterparts, Table 3.2.

The nanofibers containing metallated porphyrins gave the narrowest band gaps indicating that these nanofibers have the most increased absorption in visible light. Narrowing the band gap energy of materials reduces the distance between the valence band and the conduction band, therefore requiring less energy for electrons to excite electrons into the conduction band. This allows for light absorption at higher wavelengths and is advantageous as it increases the nanofiber activity in the visible region and, thus, makes them more applicable for use in sunlight and other visible light sources. The electrons also require less effort for nanofiber activity which aids in the catalysis activity of the nanofibers containing porphyrins for applications in antimicrobial studies.

3.2.2 X-ray diffraction

The diffractograms in Fig. 3.7 (A) compares mixed-phase titania nanofibers before and after adsorption with **1-Sn** and **1-In** and the diffractograms presented in Fig. 3.7 (B) show purely rutile titania nanofibers before and after adsorption of free base *r*TiO_2 _**3** and metallated porphyrins *r*TiO_2 _**3-Sn**, (similar peaks were obtained for TiO_2_**1-Sn** and TiO_2_**2-Sn**.) The mixed phase TiO_2 nanofibers show diffraction peaks at (004), (200) and (215) tetragonal planes of anatase TiO_2 (JCPDS card no. 12-1272)[117] as well as (110), (101), (111), (210), (211), (220), (002), (310), (301) and (121) planes of the rutile phase TiO_2 (JCPDS card no. 21-1276)[117]. The *r*TiO_2 nanofibers show diffraction peaks at 28.05° (110), 36.49° (101), 39.27° (200), 41.75° (111), 44.56° (210), 54.81° (211), 57.12° (220), 63.22° (002), 64.56° (310), 69.48° (301) and 70.25° (112) planes of the rutile phase TiO_2 (JCPDS card no. 21-1276[117] and catalogue JCPDS-ICDD 2003 file number 89-4920[118]. These diffractograms also indicate the successful formation of mixed-phase nanofibers as well as the successful formation

of pure rutile nanofibers There were no significant changes noted in the diffraction peaks of the bare titania and when compared to the dyed nanofibers indicating that the presence of porphyrins does not introduce any structural changes to the nanofiber[119].

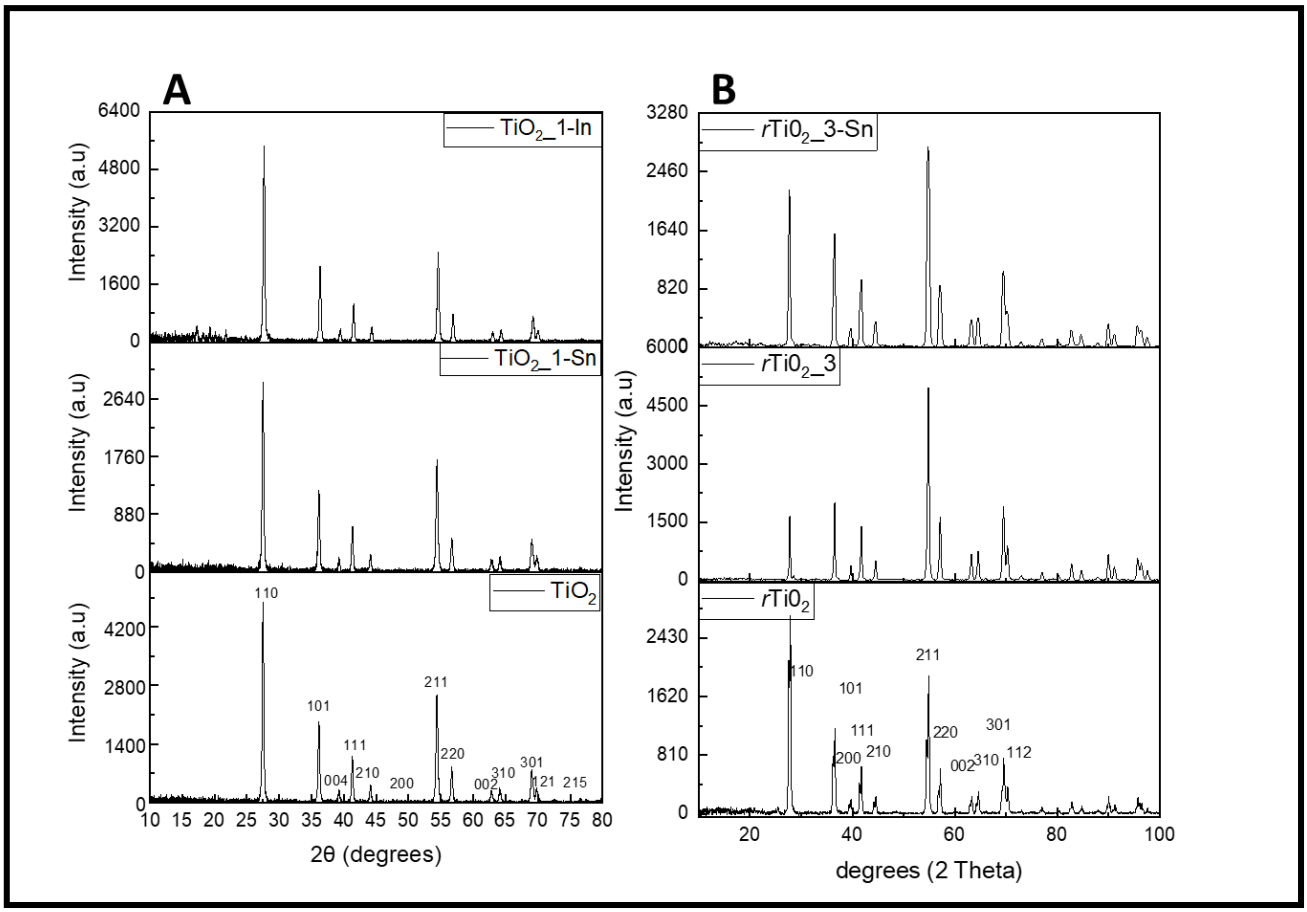

Figure 3.7: Diffractograms of mixed-phase TiO_2 (A) and single-phased rutile *r*TiO_2 (B) nanofibers before and after adsorption of porphyrins.

3.2.3 Fourier Transform Infrared Spectroscopy

Infrared spectroscopy in Fig. 3.8 showed a prominent titania peak near 500 cm^{-1} present in all samples. Peaks were observed at 3000-3200 cm^{-1}, 1500-1680 cm^{-1} and

1100-1300 cm^{-1} of the C-H bonds, C=C bonds, and the C-O of the methoxy groups in the porphyrin respectively, for TiO_2_**1,** TiO_2_**1-Sn**, TiO_2_**2-In,** Fig. 3.8 (A).

Aromatic C-H bonds and C=C bonds originating from porphyrins were also observed at 2900-3000 cm^{-1} and 1300-1500 cm^{-1} respectively for samples *r*TiO_2_**3**, *r*TiO_2 _**1-Sn** *r*TiO_2_**2-Sn** and *r*TiO_2_**3-Sn**, Fig. 3.8 (B). The presence of porphyrin peaks on the nanofibers indicates a successful dying of the porphyrin complexes onto the nanofibers.

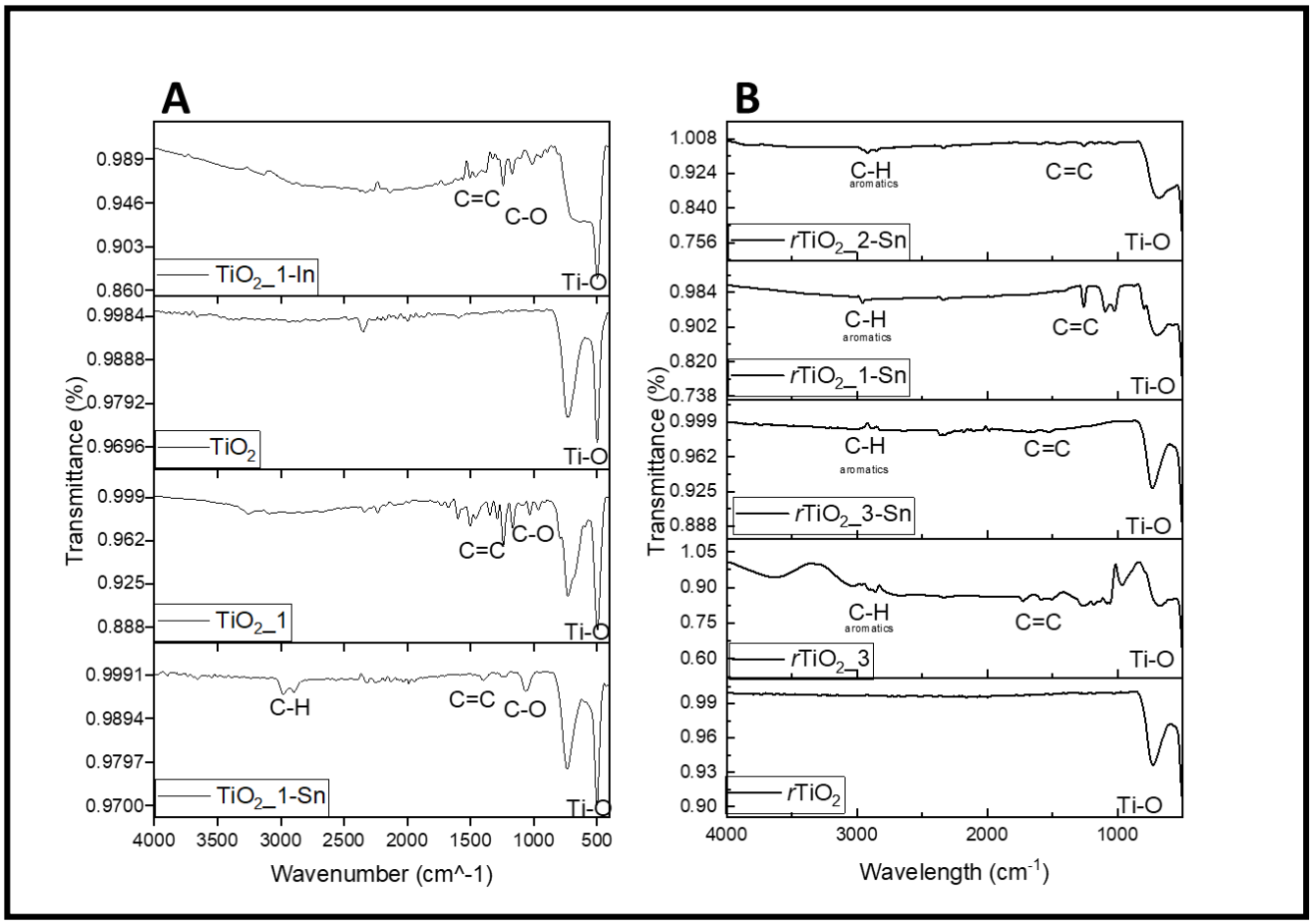

Figure 3.8: FTIR of mixed-phase bare titania nanofiber, TiO_2_**1,** TiO_2_**1-Sn** and TiO_2_**2-In** dyed nanofibers (A), and rutile phase TiO_2, TiO_2_**3**, TiO_2_**1-Sn**, TiO_2_**2-Sn** and TiO_2_**3-Sn** (B).

3.2.4 Thermogravimetric analysis

A thermogravimetric analysis (TGA) was used to assess and compare the thermostability of nanofibers before and after calcination, as well as after dyeing the nanofibers with complexes **1-Sn** and **1-In** dyes and the results for mixed-phase titania are shown in Fig. 3.9 (A). The initial thermogram of PVP/Titania indicated that there is a significant amount of weight loss that stabilises around 500 ℃, indicating that all of the support PVP polymer has been burnt off therefore leaving the titania. The PVP support polymer was then calcined at 650 ℃ to yield bare mixed-phase titania which was then dyed with **1-Sn** and **1-In** and the obtained thermograms indicated that the bare calcined and dyed TiO_2 remained fairly thermostable.

Fig. 3.9 (B) compares the thermograms of complex **3** before and after metallation. The metallated complex **3-Sn** shows a faster degradation than the free base complex **3**. TiO_2 and *r*TiO_2, (Figs. 3.9 (A) and 3.9 (B) respectively), displayed good thermostability with an overall mass loss of 1.49% and 8.06%, respectively.

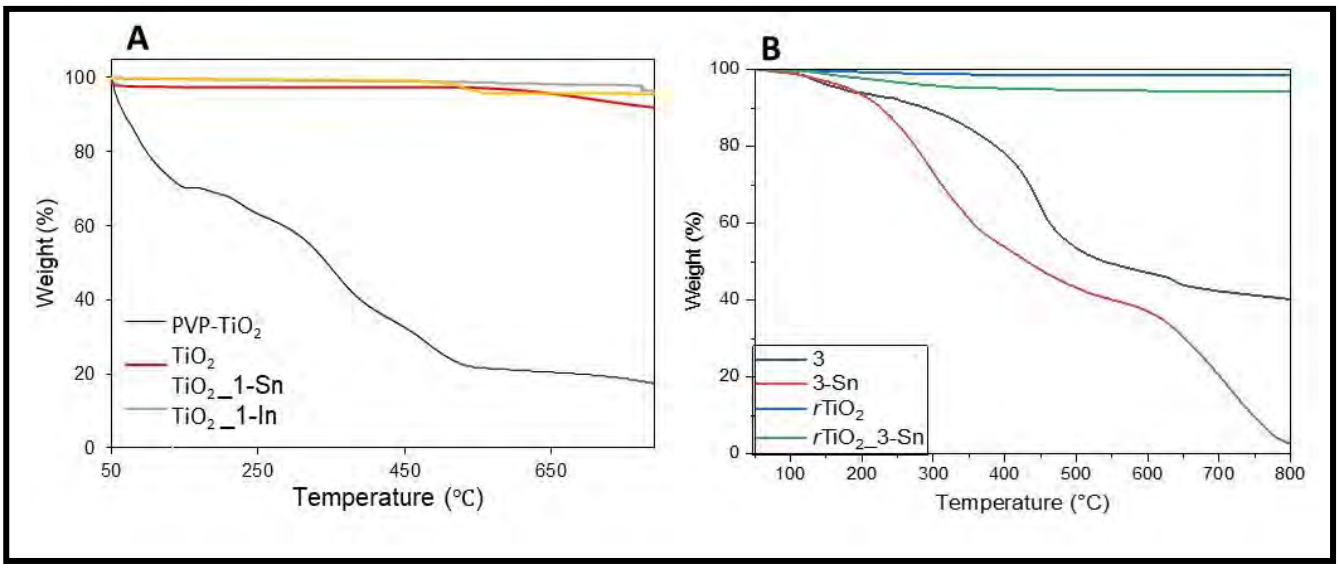

Figure 3.9: A thermogram of titania nanofibers before and after adsorption to porphyrin complexes **1-Sn** and **1-In** dyes (A), and a thermogravimetric analysis graph of percentage weight loss of complex **3** before and after adsorption onto *r*TiO_2 nanofiber (B).

The *r*TiO_2_**3-Sn** displayed an expected increased percentage mass loss in comparison to the more stable peak *r*TiO_2, indicative of porphyrin degradation. Similar degradation patterns were observed for the other porphyrins. The thermogravimetric data was used to assess the loading of porphyrins onto the nanofibers,[120] and the results are presented in Table 3.2. This involves comparing the mass in the TGA pan after the decomposition of the TiO_2 -porphyrin with that of the porphyrin alone. Equal masses (mg) for porphyrin and respective TiO_2 -porphyrin were weighed separately in the TGA pan and then heated in argon to 800°C. The data shows that the free base porphyrin (*r*TiO_2_**3**) had a smaller loading of 1.85%, while the metallated porphyrins had larger loadings of 5.86%, 5.90%, and 4.35%, for *r*TiO_2_**1-Sn** and *r*TiO_2_**2-Sn** and *r*TiO_2_**3-Sn,** respectively and 4.87% and 3.68% for TiO_2_**1-Sn** and TiO_2_**1-1n.**

3.2.5 Scanning Electron Microscopy

Scanning electron microscopy (SEM) images were obtained to assess the morphological structure of the nanofibers before calcination, as well as before and after porphyrin adsorption. The images in Fig. 3.10 are those of PVP-TiO_2, bare calcinated TiO_2 and *r*TiO_2, TiO_2_**1**, TiO_2_**1-Sn,** and *r*TiO_2_**1** dyed nanofibers.

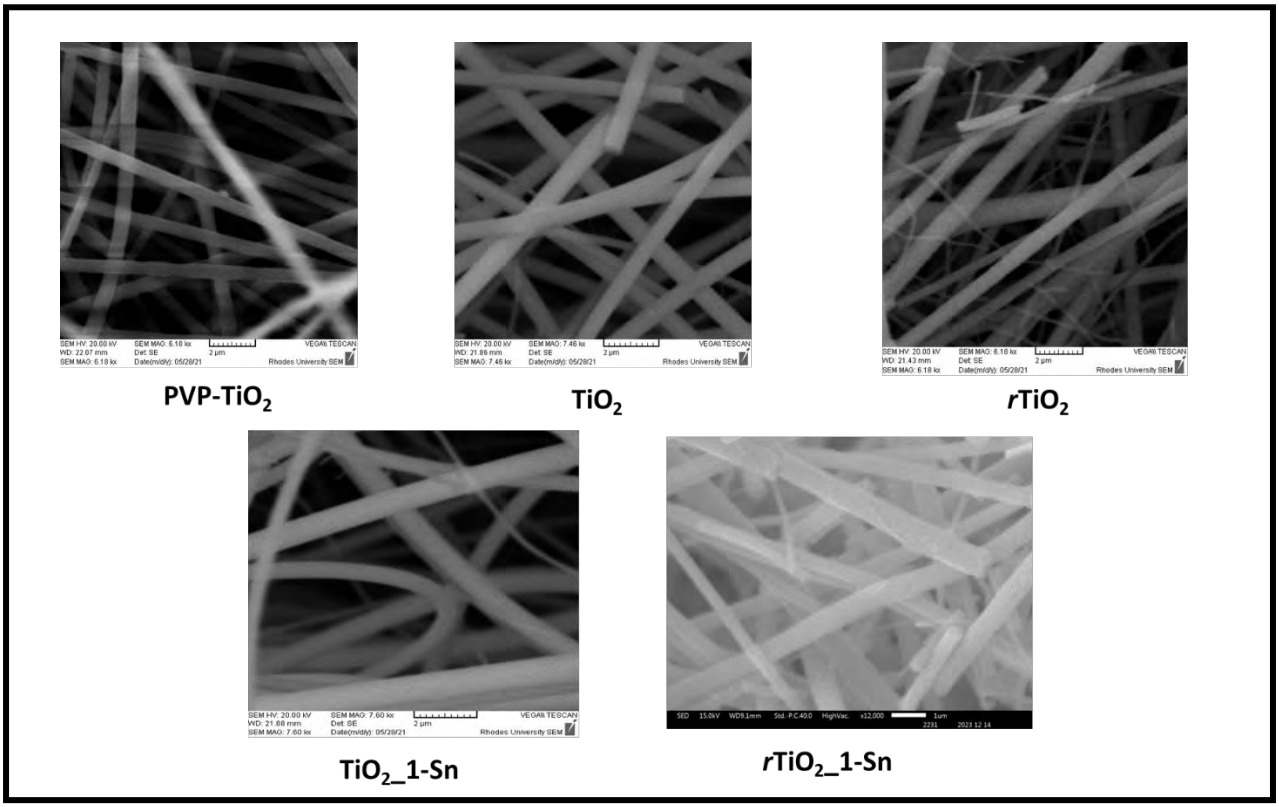

Figure 3.10: Scanning electron microscopy images of TiO_2 with PVP pre-calcination, before and after adsorption with porphyrins.

The SEM images were also used to determine size difference where it was observed that before calcination, the nanofibers TiO_2 with PVP polymer had average diameters of 665 ± 140 nm, Table 3.2. The bare calcinated mixed-phaseTiO_2 were observed to have an average diameter of 515 ± 86 nm and the metalloporphyrin dyed nanofibers were observed to have average diameters of 481 ± 82 nm, Table 2. The notable

decrease of 150 nm in diameter size post calcination was expected as the support polymer is removed, while the dyed nanofibers which differ by 34 nm from the bare calcinated TiO_2 fall within the error limits of the bare nanofibers. This can be deemed as normal since the adsorption method used does not change the morphology of the nanofibers as can be seen in the SEM images obtained (Fig. 3.10). The rutile nanofibers were observed to have smaller diameters than those of the mixed nanofibers and with the bare *r*TiO_2 having average diameters of 382 ± 9.09 and the metallated porphyrin nanofibers *r*TiO_2_**1-Sn** and *r*TiO_2_**2-Sn** and *r*TiO_2_**3-Sn** having average diameters of 321.45 ± 5.30, and an example of the histogram used for size determination can be found in Fig. S3.

3.3 Conclusions to the chapter

The characterisation of complexes **3** and **3-Sn** showed successful syntheses with MALDI-TOF Mass spectrometry giving the expected mass for complex **3** and a mass corresponding to $[M\text{-}Cl+2H]^+$ amu. UV–vis spectroscopy showed the expected peaks consistent with those of freebase and metallated porphyrins for **3** and **3-Sn** respectively and ^1H NMR spectroscopy showed the expected protons for both complexes with some instrumental grease peaks.

Solid-state ultraviolet-visible spectroscopy, XRD, FT-IR, TGA and SEM were used to characterise TiO_2 nanofibers and porphyrin-adsorbed TiO_2. The results obtained from XRD indicated a successful fabrication of both mixed-phase anatase/rutile and single-phase rutile nanofiber while the solid-state UV-vis and FTIR showed successful adsorption of the porphyrin dyes into the nanofibers, and the titania peaks from the UV-vis indicating lower band gaps for the single-phase rutile TiO_2 and its porphyrin dyed counterparts. The thermograms obtained from the TGA analysis showed good

thermostability of TiO_2. The thermal degradation curves were used to determine the % loading of porphyrins onto the nanofibers and it was noted that metallated porphyrins had a larger % loading onto the nanofibers than the free base complex **3**. SEM images obtained also proved a successful fabrication of nanofibers ranging between 321.45 ± 5.30 and 515 ± 86 nm in size.

Chapter 4

Photophysicochemical studies

Photophysicochemical studies, namely triplet lifetimes, fluorescence lifetimes and singlet oxygen quantum yields of porphyrins alone and on nanofibers where necessary were determined and are discussed in this chapter.

4. Photophysicochemical parameters

Table 4.1 summarises the photophysical and photochemical properties of porphyrins alone or adsorbed onto nanofibers.

4.1 Triplet lifetimes

The triplet decay curve of complex **3** along with its best-fit curve presented in Fig. 4.1 show an example of the plots constructed to determine the triplet lifetimes of the complexes presented in Table 4.1.

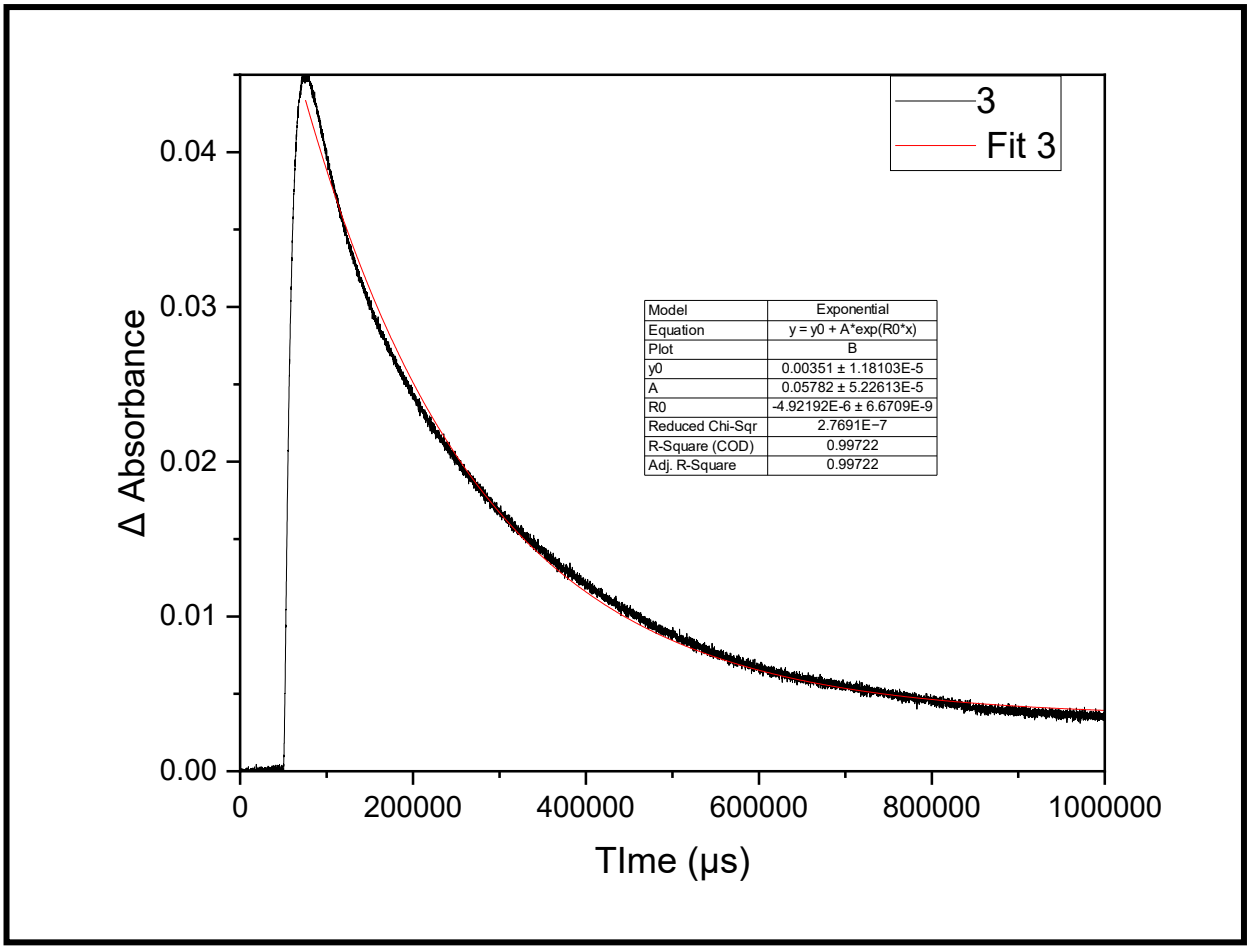

Figure 4.1: An example of the triplet decay curves (complex **3**) used in the calculations of the triplet lifetimes.

The data collected indicated that the metallated porphyrin (complex **3-Sn**) gave a longer triplet lifetime compared to the free base **3**, with a lifetime of 58 μs. Symmetrically substituted complexes **1-In, 1-Sn**, and **2-Sn** showed shorter lifetimes of 13, 37 and 106 μs compared to the asymmetrical complexes **3-Sn** having the longest 119 μs. Thus, asymmetry improves triplet state properties in porphyrin-type complexes as reported before[121].

4.2 Fluorescence lifetimes and quantum yields

The fluorescence lifetimes (τ_F) presented in Table 4.1 were obtained from running a time-correlated single photon count method that produced the curve in Fig. S4 (supplementary information). The free base complex **3**, with a lifetime of 6.55 ns, was observed to have longer fluorescence lifetimes compared to complex **3-Sn**, and the other metallated complexes **1-Sn**, **1-In**, and **2-Sn**, which had fluorescence lifetimes of 0.88, 1.65, 6.30, and 0.73 ns, respectively. The fluorescence quantum yields were also low for metallated derivatives, corresponding to fluorescence lifetimes, Table 4.1. This indicates that upon metallation, intersystem crossing into the triplet state was promoted, and this is advantageous as a complex can produce more singlet oxygen species in the triplet state.

Table 4.1: Summary of photo physicochemical properties of porphyrin complexes alone or when adsorbed onto TiO_2 nanofibers, where τ_F, τ_T, and Φ_Δ refer to fluorescence lifetimes, triplet state lifetimes, and singlet oxygen quantum yields, respectively, in DMF unless otherwise stated. TiO_2 refers to mixed-phase anatase and rutile nanofibers, while *r*TiO_2 refers to purely rutile nanofibers.

Complexes	τ_T (µs) [a]	τ_F (ns)	Φ_f	Φ_Δ [b]
1-Sn	37	1.65	0.01	0.62
1-In	13	6.30	0.01	0.59
2-Sn	106	0.73	0.01	0.84
3	58	6.55	0.10	0.50
3-Sn	119	0.88	0.02	0.69
TiO_2	-	-	-	(0.14)
rTiO_2	-	-	-	(0.27)
TiO_2_**1-Sn**				(0.32)
rTiO_2_**1-Sn**	-	-	-	(0.27)
TiO_2_**1-In**				(0.29)
rTiO_2_**2-Sn**	-	-	-	(0.23)
rTiO_2_**3**	-	-	-	(0.20)
rTiO_2_**3-Sn**	-	-	-	(0.30)

[a] values were obtained in dimethyl sulfoxide, [b] values in brackets were determined in water.

4.3 Singlet Oxygen quantum yields

Porphyrins are known to undergo a type II mechanism to generate ROS such as singlet oxygen species[122]. The plots in Fig. S5 are representative of those used in the determination of the singlet oxygen quantum yields (Φ_Δ) of complexes **1-Sn**, **1-In**, **2-Sn** and **3-Sn** (A), TiO_2 nanofibers, TiO_2_**1-Sn** and TiO_2_**1-In**, rTiO_2_**1**, rTiO_2_**1-Sn**, rTiO_2_**2-Sn**, and rTiO_2_**1-Sn** (B), irradiated at time intervals of 30 s for the metalloporphyrins in DMF and 5 min intervals for the dyed nanofiber samples in aqueous media. The plots show that the porphyrin remains stable throughout the irradiation and does not degrade over time. In contrast, the DMA and ADMA peaks (Fig. S5) show a steady decrease in absorbance after being irradiated over time.

The singlet oxygen quantum yields (Φ_Δ) obtained here further support those of the triplet and fluorescence lifetimes and indicate that upon metallation, metallated complex **3-Sn** exhibited higher yields than the free base complex **3**. Complex **2-Sn** gave the highest singlet oxygen quantum yield of 0.84. Heavy atom effect has been known to enhance intersystem crossing into the triplet state[57] and this may account for the higher quantum yields of the tetra thiomethyl substituted complex **2-Sn**. It is known that the introduction of sulphur atoms into the porphyrin ring induces an increase in intersystem crossing rate due to spin-orbit coupling enhancement, resulting in enhanced singlet oxygen quantum yields[123].

The singlet oxygen quantum yields of porphyrins on nanofibers were low in water due to the quenching effect of singlet oxygen in water[64]. In addition, oxygen has higher solubility in many organic solvents compared to water[124]. The results showed that when adsorbed onto nanofibers, the porphyrins showed the same pattern as that of the porphyrins alone, where the nanofibers containing metallated porphyrins gave higher quantum yield than **3**. TiO_2_**1-Sn** (of the mixed phase) and *r*TiO_2_**3-Sn** (of pure

rutile) performed best yielding Φ_Δ values of 0.32 and 0.30, respectively. When comparing complex **1-Sn** dyed nanofibers of the mixed phase titania and that of the rutile phase titania, it was noted that *r*TiO_2_**1-Sn** had a lower Φ_Δ of 0.27 than TiO_2_**1-Sn** at 0.30. This may be a result of the higher catalytic activity of the anatase phase[79] of the nanofiber**.** The singlet oxygen quantum yields of TiO_2 photocatalyst powders have been reported to range between 0.12-0.38[125], and the values obtained in this work are within this range, with TiO_2 and *r*TiO_2 yielding 0.27 and 0.14, respectively.

The mechanism of action for the ROS formation of TiO_2 nanomaterials is not yet widely understood,[126,127] however, the photocatalytic activity of the materials has been explained[97]. Semiconductors consist of a valence band and conduction band. Upon the absorption of energy from a light source, electrons are transferred from the valence band to the conduction band leaving behind some positively charged holes in the valence band that then form electron-hole pairs. Electrons and holes can migrate to the TiO_2 surface where they can generate hydroxyl radicals by oxidising H_2O and OH^- [97], in a similar manner to how ROS are created in a type 1 mechanism as depicted in Fig. 1.6. Upon adsorbing porphyrin dyes onto nanofibers, the photocatalytic activity of the nanofiber along with the singlet oxygen from the photosensitiser creates a synergistic effect that catalyses and enhances the microbe-killing effect of the dyed nanofiber.

4.4 Conclusions to the chapter

Triplet lifetimes, fluorescence lifetimes and quantum yields, and singlet oxygen quantum yields of porphyrin complexes alone and on nanofibers, where necessary, were determined. The results showed that the physicochemical properties of the porphyrins improve upon metallation, and this can be seen in the case of **3** and **3-Sn**

where upon metallation, the fluorescence lifetime and quantum yield decrease while the triplet lifetime and singlet oxygen quantum yield increase. The results obtained here were desirable, proving that the complexes are viable candidates for photoinactivation studies.

The porphyrin-adsorbed nanofibers showed similar trends where the nanofibers containing metallated porphyrin complex **3-Sn** gave higher singlet oxygen quantum yield than the nanofiber containing the free base complex **3**.

Chapter 5

Antimicrobial photodynamic inactivation

This chapter explores the application of the synthesised porphyrins and the fabricated mixed phase anatase/rutile TiO_2 and pure rutile TiO_2 in antimicrobial inactivation studies. The studies are conducted against *Staphylococcus aureus (S. aureus), Escherichia coli (E. coli) and Candida albicans (C. albicans)*.

5.1. Antimicrobial photodynamic inactivation (aPDI) studies

Blank studies were done to ensure the sterility of the phosphate-buffered solution (PBS) and control studies were performed to ensure that the use of DMF does not increase or quench bacterial growth. No bacterial growth was observed on the blanks and the DMF was observed not to have any effect on the bacterial growth. *S. aureus* was used for the aPDI studies.

5.1.1 Antimicrobial inactivation therapy of porphyrins in solution

Porphyrin complexes **1**, **1-Sn** and **2-Sn** were used in the inactivation of *S. aureus* in solution, For porphyrins alone, *S. aureus* was treated to different concentrations of the porphyrin drugs ranging from 3 μM to 100 μM in 1% DMF, incubated at 37 °C for 30 min to allow for the porphyrin drugs to localise into the bacterial cells and then irradiated for 60 min with a j-spectrum halogen lamp (340-800 nm, with a fluence of 30 mW/cm^2). The same study was repeated for dark studies, where instead of irradiation, the bacterial suspensions treated with porphyrins were left in the dark for 60 min. Log reduction values were determined and the results are presented in Fig. 5.1 and Table 5.1.

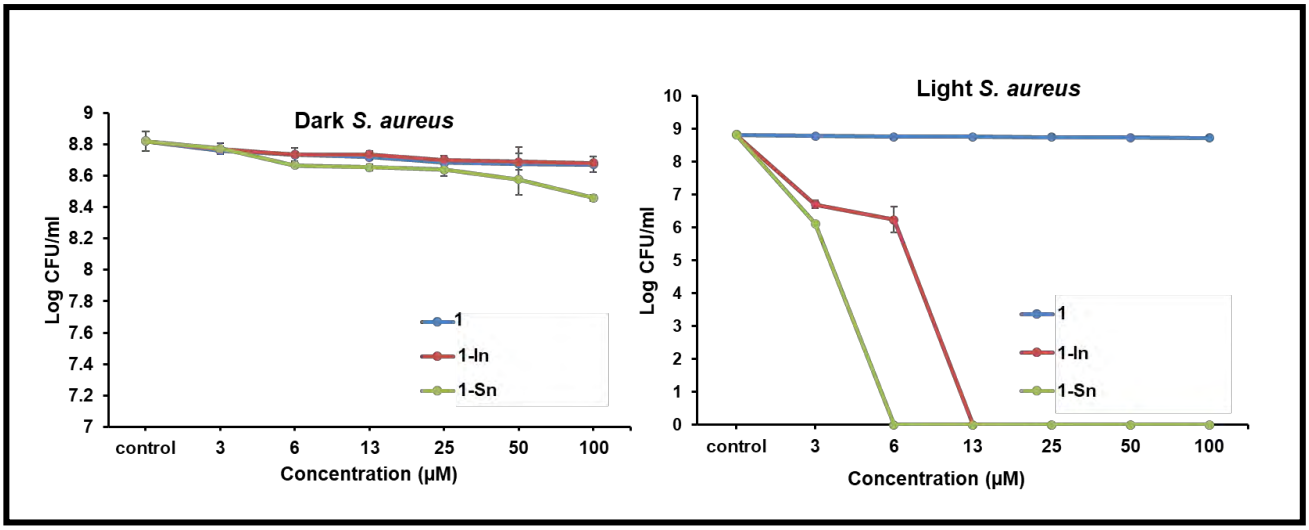

Figure 5.1: *S. aureus* after a 60 min light irradiation in the presence of complexes **1**, **1-Sn** and **1-In** in solution (1% DMF in PBS).

The porphyrin concentration studies presented in Fig. 5.1 indicate that after a 60 min irradiation time, free base complex **1** porphyrin showed a very low log reduction of 0.09 (Table 5.1) and a high cell viability of 82.8% at a concentration of 100 μM. Complexes **1-In** and **1-Sn** however, displayed impressive results with log reductions of 8.82 and up to 100% cell inactivation at much lower concentrations of 12.5 μM and 6.0 μM, respectively. The results also indicate that complex **1-In** required a higher concentration of the photosensitiser when compared to complex **1-Sn** to achieve complete bacterial eradication.

5.1.2 Antimicrobial inactivation studies of porphyrins dyed mixed phase TiO_2 nanofibers

Studies of the porphyrins on the mixed-phase nanofibers were carried against *S. aureus*. The experiments were performed as follows: 5 mg of porphyrin-dyed nanofibers were placed in bacterial suspensions in a 48-well plate and then incubated

for 30 min, followed by irradiation at 15 min intervals for 60 min. Dark studies were conducted where bacterial suspensions treated with dyed nanofibers were left in the dark at the same intervals as the light studies. The observed cell viability of *S. aureus* after being treated with the dyed nanofibers is presented in Fig. 5.2. The studies were done in triplicates.

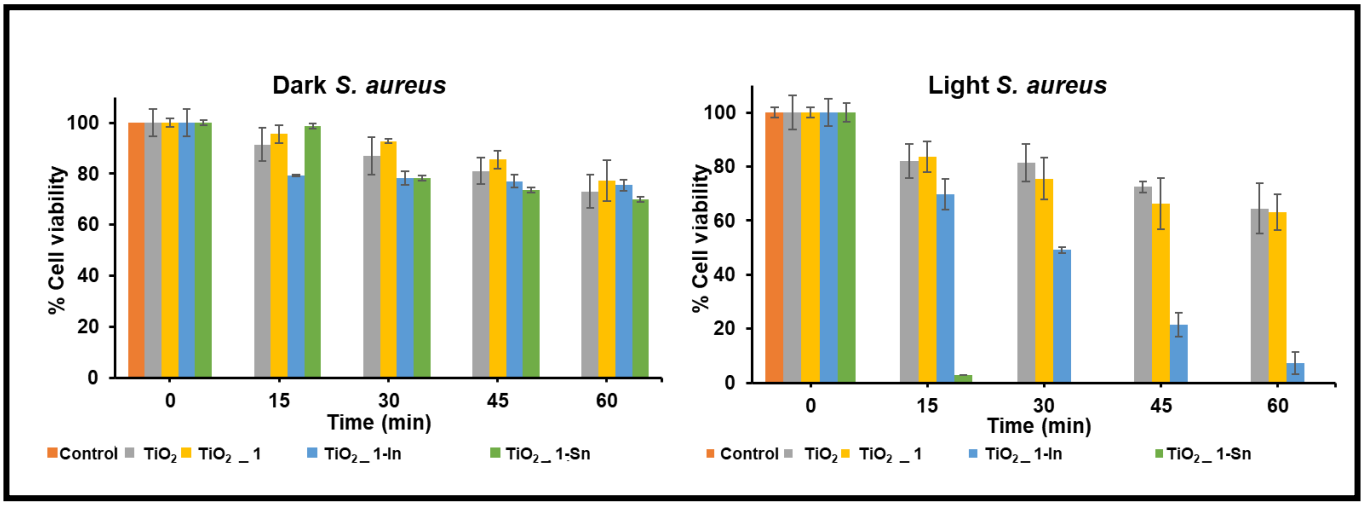

Figure 5.2: Cell viability of *S. aureus* after 60 min irradiation in the presence of TiO_2, TiO_2_**1**, TiO_2_**1-Sn**, TiO_2_**1-In**.

Table 5.1: Summary of % cell viability and log reduction of *S. aureus* after 60 min of irradiation, unless otherwise stated. Values for the porphyrin complexes alone were recorded in 1% DMF in PBS in solution.

Sample	**Cell viability (%)**	**2nd Reuse Cell viability (%)**	**Log reduction (Log CFU/ mL)**	**2nd Reuse (Log CFU/ mL)**
1 (100)[a]	82.8	-	0.09	-
1-In (12.5)[a]	0.00	-	8.82	-
1-Sn (6.0)[a]	0.00	-	8.82	-
TiO_2	64.6	98.6	0.16	0.01
TiO_2_**1**	63.1	86.6	0.22	0.06
TiO_2_**1-In**	7.23	37.3	1.30	0.54
TiO_2_**1-Sn**	0.00 (30 min)[b]	0.00	8.54 (30 min)[b]	8.35

[a] values in brackets are for the concentration in μM, [b] 30 min irradiation

The nanofiber time-dependent studies presented in Fig. 5.2 display a similar trend to studies in solution where TiO_2_**1-Sn** has a complete inactivation of bacteria after 30 min of irradiation. TiO_2_**1-In** nanofibers displayed 92.8% cell inactivation after 60 min of irradiation. This can be accounted for by the heavy atom effect that both tin and indium provide, as heavy metals are known to greatly enhance optical properties[57]. This reason also accounts for the notable bacterial cell death of the bare TiO_2 nanofibers as titanium is also a heavy metal where a 64.6% cell viability was observed after 60 min of irradiation. The bacterial inactivation properties of TiO_2 post-dyeing

display an enhancement that further highlights the synergistic effect of the porphyrins and the nanofibers.

5.1.3 Antimicrobial inactivation studies using rutile TiO_2

Microbial studies were carried out on *Staphylococcus aureus (S. aureus), Escherichia coli (E. coli) and Candida albicans (C. albicans)* to assess the antimicrobial effect of porphyrins in solution or adsorbed onto rutile titania (*r*TiO_2) nanofibers on the mentioned microorganisms.

Different concentrations (3, 6, 13, 25, 50 and 100 μM for *S. aureus* and 6, 13, 25, 50, 100 and 200 μM for *E. coli* and *C. albicans*) of porphyrin complexes were prepared in 5% DMF and treated against 1×10^7 CFU/mL of *S. aureus, E. coli* and *C. albicans* to determine the optimum working concentrations for the porphyrin complexes using Fig. S6, and the cell viability decreased with increase in concentration. The final concentrations of 200 mM for *C. albicans*, 100 mM for *S. aureus*, and 200 mM for *E. coli* were employed for aPDI studies. *E. coli* cells contain an outer cell wall and *C. albicans* are generally more complex eukaryotic cells that are harder to inactivate than the simpler *S. aureus*. As a result, the final concentrations of porphyrins were doubled for the more complex *E. coli* and *C. albicans*. The log reduction results at these concentrations of porphyrin complex are presented in Table 5.2. 20 mg using *r*TiO_2 nanofibers were employed for aPDI.

5.1.3.1 Dark toxicity

Bare *r*TiO_2 exhibited a 28.9% decrease in cell viability in the dark, Fig. 5.3 for *S. aureus.* In Fig. 5.3, 20 mg of nanofibers containing porphyrins were incubated for 30 min before irradiating one of the samples for 1 h and keeping the other in the dark for the same amount of time. The cell viability values decreased by 24.4% for *r*TiO_2_**3**, 15.6% for *r*TiO_2_ **3-Sn**, and 28.6% for *r*TiO_2_**2-Sn** against *S. aureus* in the dark. Sn metal on its own has been reported not to have any antimicrobial activity[128], the dark toxicity detected by the tin porphyrins could attributed to the chlorine atoms attached to the tin, as they are known to inactivate microbes in water[129]. Although enhanced by light, TiO_2 can form ROS both under UV light and in dark conditions[130], and this further explains the dark toxicity detected.

In a study by Gladkowski et al, some methoxy-substituted flavanones were studied against their unsubstituted counterparts where it was noted that the compounds containing the methoxy substituents inhibited the growth of various bacteria and fungi[131]. Similar results were observed in studies by Suwito et al and Marques et al where variations of chalcones containing the methoxy substituents displayed antibacterial and antifungal properties[62,63]. This antibacterial effect of the methoxy substituent accounts for the bacterial inactivation observed in the dark studies in Figs. 5.2 and 5.3.

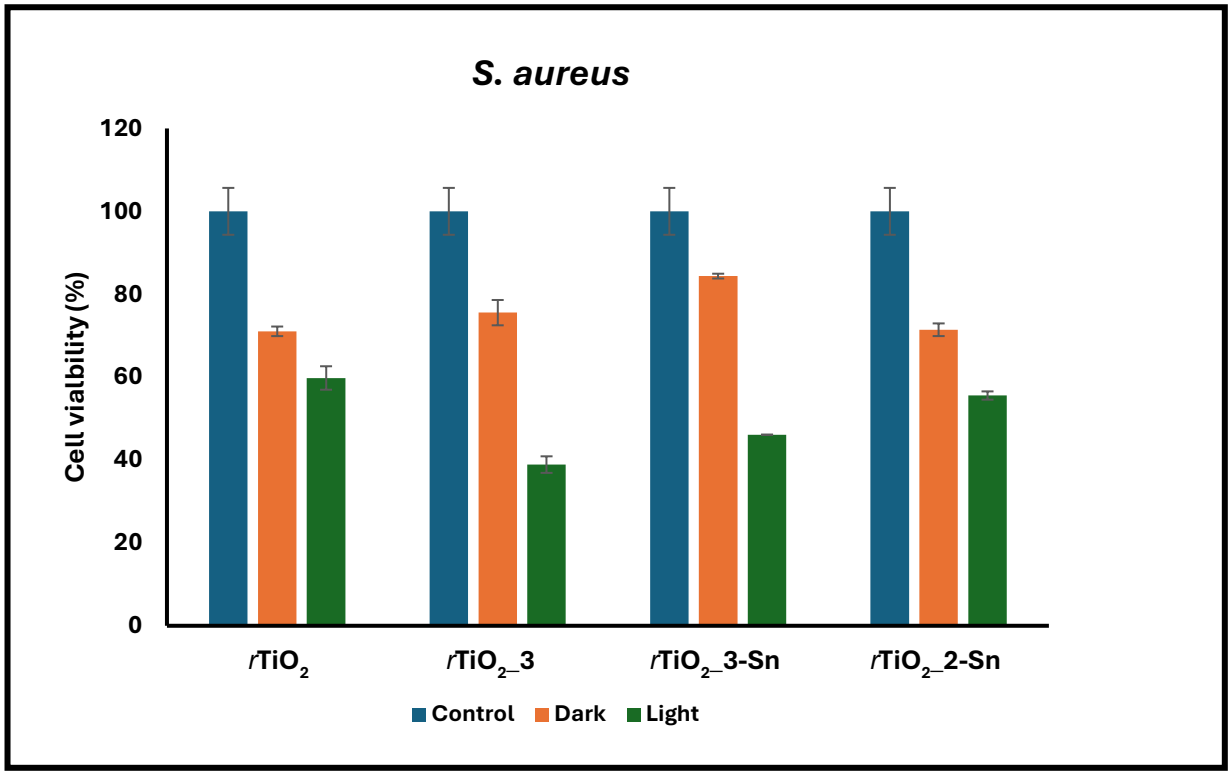

Figure 5.3: An assessment of dark toxicity of porphyrins adsorbed onto *r*TiO_2 nanofibers against *S. aureus* after a 60 min irradiation using 20 mg of nanofibers.

Table 5.2: Log reduction values of post-treatment with porphyrin complexes and cell viabilities of nanofibers 1 h post-treatment irradiation (unless otherwise stated). For porphyrin complexes in solution, the concentrations of 200 mM for *C. albicans*, 100 mM for *S. aureus*, and 200 mM for *E. coli* were employed. For the nanofibers, 20 mg were employed.

Samples	Log Reduction *(% cell viability)*		
	S. aureus	*E. coli*	*C. albicans*
3	1.29 (49.9)	1.54 (31.7)	-
3-Sn	1.56 (5.83)	1.70 (53.9)	0.67 (3.78)
2-Sn	1.35 (24.8)	1.55 (34.8)	0.63 (7.42)
rTiO_2	0.36 (83.6)	0.46 (53.6)	0.32 (40.2)
rTiO_2_**3**	0.63 (31.7)	0.65 (32.9)	0.92 (15.1)
rTiO_2_**1-Sn**	8.80(0.0)	0.20 (52.8)	0.64 (17.0)
rTiO_2_**2-Sn** (2 h)	6.76 (0.0)	0.81 (48.1)	0.95 (17.3)
rTiO_2_**3-Sn**	6.76 (0.0)	0.76 (77.5)	0.31 (4.7)

5.1.3.2 aPDI studies

The porphyrin aPDI studies (Table 5.2) indicate that the porphyrins in solution (**3** as an example) applied in this work were not very effective in eradicating microbes giving

log reductions less than the recommended log 3[132]. There was a large improvement in log reduction values when tin porphyrins were adsorbed on the *r*TiO_2 nanofibers with values of 6.76. 6.76 and 8.8 for *r*TiO_2_**3-Sn,** *r*TiO_2_**2-Sn**, and *r*TiO_2_**1-Sn**, respectively, for *S. aureus,* Table 5.2 and Fig. 5.4. The increase in log reduction for Sn metallated porphyrin complexes when adsorbed onto *r*TiO_2 nanofibers for *S. aureus* is due to the synergistic effect of the porphyrins and the nanofiber. However, this is not the case for *C. albicans and E. coli*. The increase in log reduction for porphyrins on *r*TiO_2 nanofibers could also be due to the dark toxicity, Fig. 5.3.

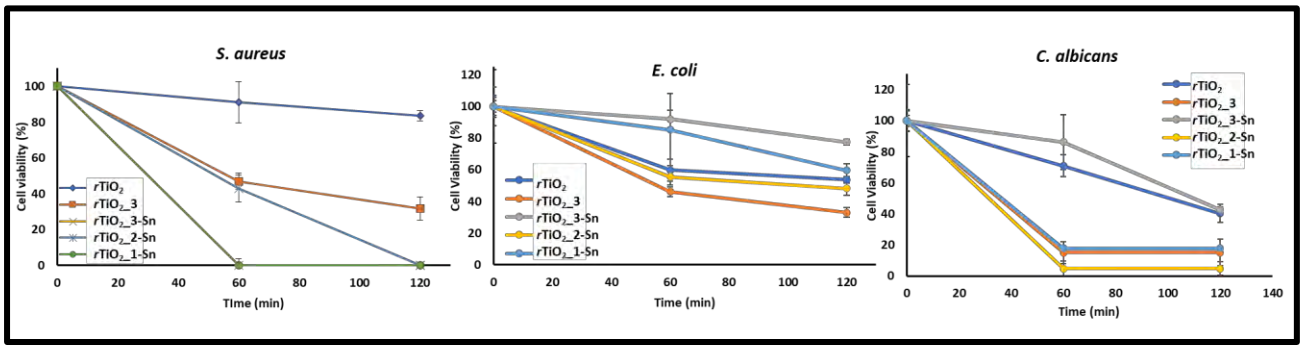

Figure 5.4: Cell viability studies of *S. aureus, E. coli* and *C. albicans* after a 2 h irradiation while being treated with porphyrins adsorbed on rutile nanofibers using 20 mg nanofiber.

5.2 Reusability studies.

The mixed-phase anatase/rutile TiO_2 nanofibers were used to assess the reusability of nanofibers. To assess the reusability of the nanofibers, they were washed three times using 70% ethanol (in PBS) following use and were left to dry overnight under UV light, to ensure cross-contamination. The cell viability results of the second time the nanofibers were reused are listed in Table 5.1.

When reused for the second time, the TiO_2_**1-Sn** nanofibers still showed a desirable bacterial inactivation with 0% viable cells, with the log reduction remaining the same after the first and second reuse cycle, after 60 min irradiation, Table 5.1. TiO_2_**1** and TiO_2_**1-In** nanofibers were less effective (as judged by the increase in % cell viability, and a decrease in log reduction) when compared to the first time they were used. This might mean that when reusing the nanofibers, more irradiation time will be required to inactivate the bacteria.

A study of the porphyrin complexes in solution was conducted to account for the drop in log reduction for **1-In,** where the photostability of complexes **1-Sn** and **1-In** were assessed in DMF as well as in aqueous media (with 1% DMF), Table S1. The % photostability in 1% DMF aqueous media decreased to 15.4% and 34.0%, for **1-Sn** and **1-In**, respectively (Fig. S7). The decline in log reduction observed in TiO_2_**1-In** when compared to that of TiO_2_**1-Sn** after reusing the nanofiber can therefore be attributed to the poor photostability of **1-In** as stated above in aqueous media.

The impressive results of the TiO_2_**1-Sn** nanofibers post application indicate that the fabricated nanofibers have a potential in the use of water treatment and can potentially be used multiple times to inactivate bacteria in water in a sustainable, cost-effective manner. Magadla *et al* have reported on the use of photodynamic inactivation of the biofilm form of bacteria[133], with high log reductions. This shows the composites reported here can be used in complex media. In addition, studies have shown that photodynamic inactivation therapy can be used for localized applications such as burn wounds[134].

After the antimicrobial photodynamic inactivation application studies, the integrity of the nanofibers was determined, using UV-Vis spectra (Fig. S8) and SEM images (Fig.

S9). The SEM images indicated that after being washed and used 3 times, some of the nanofibers display some breakage that can be noted by shorter fragments of the nanofibers, Fig. S9. The UV-Vis spectra indicated that post application, the porphyrin dyes nanofibers were still well adsorbed onto the nanofibers, as can be seen by the Soret bands and Q-bands typical of porphyrins, Fig. S8. This proves that the porphyrins are insoluble and do not leech into the aqueous bacterial solutions, therefore making them applicable for water treatment.

5.3 Conclusions to the chapter

Antimicrobial inactivation studies were performed against*, S. aureus, E. coli, and C. albicans.* The research detailed in the chapter showed that when in solution complex **1-Sn** eradicated 100% of *S. aureus* at a low concentration of 6.0 μM followed by complex **1-In** at a concentration of 12.5 μM. Complexes **2-Sn, 3** and **3-Sn** however, were less effective, producing log reduction lower than the recommended value of 3 for *S. aureus, E. coli, and C. albicans*.

Mixed phase anatase/rutile TiO_2 were used to inactivate *S. aureus* while pure rutile TiO_2 were studied in the inactivation of *S. aureus, E. coli, and C. albicans*. When dyed onto nanofibers, complex **1-Sn** still demonstrated good efficacy in the inactivation of *S. aureus,* with log reductions of 8.54 and 8.80 when adsorbed onto TiO_2 and *r*TiO_2 respectively, with the more photocatalytic TiO_2_**1-Sn** eradicating the bacteria at half the time of *r*TiO_2_**1-Sn**. Good eradication of *S. aureus* was also observed for *r*TiO_2_**2-Sn** and *r*TiO_2_**3-Sn**, while unsatisfactory results were obtained for the inactivation of *E. coli* and *C. albicans*.

When assessing reusability, TiO_2_**1-Sn** was still able to inactivate *S. aureus* after 2 reuse cycles, while the less photostable TiO_2_**1-In** was only able to achieve an eradication of 62.7% after the second reuse cycle.

6. Conclusions

In conclusion, the data presented in this work indicates great applicability of nanofibers in the visible range with the solid-state UV-Vis absorption data indicating that the porphyrins show more red-shifted peaks when adsorbed on nanofibers. Based on this research, it can be concluded that porphyrins adsorbed on TiO_2 nanofibers have potential in the inactivation of microorganisms.

When in solution, complex **1-Sn** presented desirable activity against *S. aureus* with 100% cell inactivation at a lower concentration than complex **1-In**. When adsorbed onto the nanofibers, complex **1-Sn** showed higher activity than complex **1-In**. Complex **1** adsorbed nanofibers displayed much less effective bacterial inactivation. The nanofibers were successfully recovered, and when reused, the best-performing TiO_2_**1-Sn** displayed 100% eradication.

The rutile nanofibers showed good activity against with up to 100% bacterial inactivation after 1 h for *r*TiO_2_**3-Sn** and 2 h for *r*TiO_2_**2-Sn**, for *S. aureus*. The porphyrins used proved to be ineffective and showed little bacterial inactivation. Although not very effective on their own, the synergistic effect created by the porphyrin dyes and rutile TiO_2 nanofibers enhanced the antimicrobial effect of the dyed nanofiber systems, thus improving bacterial inactivation. The results here show that dyed rutile nanofibers have some good potential in antimicrobial research.

Future perspectives

One of the challenges encountered in this work was that cationic porphyrins, which are reported to improve efficacy due to enhanced penetration into the cell wall of gram-

negative bacteria, could not be studied in this work due to their increased solubility in aqueous media.

In this work, porphyrins were physically adsorbed onto nanofibers. The fabrication of nanofibers and the synthesis of porphyrins could be modified in a manner that allows for the exploration of other conjugation methods such as a stronger chemical bond as opposed to physical adsorption, to reduce leeching of charged compounds. This would increase the efficacy of the porphyrin-nanofiber system in eradicating a wider range of microorganisms. Composites of TiO_2 /Chitosan nanofibers could be fabricated as chitosan is also insoluble in water and has antimicrobial properties. Asymmetric charged porphyrins containing a carboxylic group could be attached to the chitosan through an amide bond or an ester bond and then electrospun. The antimicrobial effect of the chitosan, the photocatalytic effect of the TiO_2 as well as the generation of singlet oxygen species by the porphyrins could synergistically enhance the inactivation of a wider range of microorganisms.

References

(1) *Water Wise - Causes of Water Pollution*. https://waterwise.co.za/site/water/environment/causes-of-water-pollution.html (accessed 2024-03-25).

(2) P. Gwimbi, M. George, M. Ramphalile, Bacterial Contamination of Drinking Water Sources in Rural Villages of Mohale Basin, Lesotho: Exposures through Neighbourhood Sanitation and Hygiene Practices. *Environ. Health Prev. Med.,* **2019**, *24*, 33. https://doi.org/10.1186/s12199-019-0790-z.

(3) T. A. Taylor, C. G.Unakal, Staphylococcus Aureus Infection. In: *StatPearls*, StatPearls Publishing: Treasure Island (FL), **2024**.

(4) G. A. C. Santos,M. Dropa, S. M. Rocha, F. A. S. Peternella, M. T. P. Razzolini, Staphylococcus Aureus and Methicillin-Resistant Staphylococcus Aureus (MRSA) in Drinking Water Fountains in Urban Parks. *J. Water Health,* **2020**, *18,* 654–664. https://doi.org/10.2166/wh.2020.042.

(5) P. Chittaphithakchai, N. Chomphulao, P. Kantasap, K. Wongput, P. Kaitpoka, T. Leesurapong, T. Loakuldilok, P. Poonlarp, S. Wangtuei, W. Jirarattanarangsri, S. Surawang, S. Osiriphun, Assessing the Likelihood of Staphylococcus Aureus Contamination in Bottled Drinking Water Production. *Biol. Life Sci. Forum,* **2023**, *26* 115. https://doi.org/10.3390/Foods2023-15073.

(6) M. Novak Babič, P. Zalar, B. Ženko, S. Džeroski, N. Gunde-Cimerman, N. Yeasts and Yeast-like Fungi in Tap Water and Groundwater, and Their Transmission to Household Appliances. *Fungal Ecol.,* **2016**, *20*, 30–39. https://doi.org/10.1016/j.funeco.2015.10.001.

(7) W. J. Cupozak-Pinheiro, A. Araújo de Almeida-Apolonio, M. H. Sasaki, N. H. Maran, R. Pires de Araújo, D. Beraldo dos Santos Silva, J. V. de Andrade dos Santos, A. Barufatti, M. Rodrigues Chang, K. M. Pires de Oliveira, *Candida* Species Contamination in Drinking Groundwater from Residence Wells in Three Municipalities of Midwestern Brazil and the Potential Human Health Risks. *Microb. Pathog.,* **2022**, *169*, 105660. https://doi.org/10.1016/j.micpath.2022.105660.

(8) *Antimicrobial resistance*. https://www.who.int/news-room/fact-sheets/detail/antimicrobial-resistance (accessed 2024-02-22).

(9) M. Vestergaard, D. Frees, H. Ingmer, Antibiotic Resistance and the MRSA Problem. *Microbiol. Spectr.,* **2019**, *7*, GPP3-0057-2018. https://doi.org/10.1128/microbiolspec.gpp3-0057-2018.

(10) D. Wu, Y. Ding, K. Yao, W. Gao, Y. Wang, Antimicrobial Resistance Analysis of Clinical Escherichia Coli Isolates in Neonatal Ward. *Front. Pediatr.,* **2021**, *9*, 670470. doi: 10.3389/fped.2021.670470.

(11) L. Poirel, J.-Y. Madec, A. Lupo, A.-K. Schink, N. Kieffer, P. Nordmann, S. Schwarz, Antimicrobial Resistance in Escherichia Coli. *Microbiol. Spectr.,* **2018**, *6*, ARBA-0026-2017, 27 pages. https://doi.org/10.1128/microbiolspec.arba-0026-2017.

(12) S. Costa-de-Oliveira, A. G. Rodrigues, Candida Albicans Antifungal Resistance and Tolerance in Bloodstream Infections: The Triad Yeast-Host-Antifungal. *Microorganisms* **2020**, *8*, 154. https://doi.org/10.3390/microorganisms8020154.

(13) Y. Lee, E. Puumala, N. Robbins, L. E. Cowen, Antifungal Drug Resistance: Molecular Mechanisms in Candida Albicans and Beyond. *Chem. Rev.,* **2021**, *121*, 3390–3411. https://doi.org/10.1021/acs.chemrev.0c00199.

(14) A. P. Pinto, I. B. Rosseti, M. L. Carvalho, B. G. M. da Silva, C. Alberto-Silva, M. S. Costa, Photodynamic Antimicrobial Chemotherapy (PACT), Using Toluidine Blue O Inhibits the Viability of Biofilm Produced by Candida Albicans at Different Stages of Development. *Photodiagnosis Photodyn. Ther.,* **2018**, *21*, 182–189. https://doi.org/10.1016/j.pdpdt.2017.12.001.

(15) M. Wainwright, Photodynamic Antimicrobial Chemotherapy (PACT). *J. Antimicrob. Chemother.,* **1998**, *42*, 13–28. https://doi.org/10.1093/jac/42.1.13.

(16) D. Muehler, E. Brandl, K.-A. Hiller, F. Cieplik, T. Maisch, Membrane Damage as Mechanism of Photodynamic Inactivation Using Methylene Blue and TMPyP in Escherichia Coli and Staphylococcus Aureus. *Photochem. Photobiol. Sci.,* **2022**, *21*, 209–220. https://doi.org/10.1007/s43630-021-00158-z.

(17) J. Oyim, C. A. Omolo, E. K. Amuhaya, Photodynamic Antimicrobial Chemotherapy: Advancements in Porphyrin-Based Photosensitize Development. *Front. Chem.,* **2021**, *9*, 635344. https://doi.org/10.3389/fchem.2021.635344.

(18) N. T. Felifel, M. A. Sliem, Z. Kamel, J. Bojarska, M. G. Seadawy, R. M. Amin, S. M. Elnagdy, Antimicrobial Photodynamic Therapy against Escherichia Coli and Staphylococcus Aureus Using Nanoemulsion-Encapsulated Zinc

Phthalocyanine. *Microorganisms,* **2023**, *11*, 1143. https://doi.org/10.3390/microorganisms11051143.

(19) M. R. Hamblin, Antimicrobial Photodynamic Inactivation: A Bright New Technique to Kill Resistant Microbes. *Curr.Opin. Microbiol.,* **2016**, *33*, 67–73. https://doi.org/10.1016/j.mib.2016.06.008.

(20) T. H. S. Souza, J. F. Sarmento-Neto, S. O. Souza, B. L. Raposo, B. P. Silva, C. P. F. Borges, B. S. Santos, P. E. Cabral Filho, J. S. Rebouças, A. Fontes, Advances on Antimicrobial Photodynamic Inactivation Mediated by Zn(II) Porphyrins. *J Photoch. Photobio. C.,* **2021**, *49,* 100454. https://doi.org/10.1016/j.jphotochemrev.2021.100454.

(21) A. Wozniak, M. Grinholc, Combined Antimicrobial Activity of Photodynamic Inactivation and Antimicrobials–State of the Art. *Front. Microbiol.,* **2018**, *9,* 930. https://doi.org/10.3389/fmicb.2018.00930.

(22) J. Ghorbani, D. Rahban, S. Aghamiri, A. Teymouri, A. Bahador, Photosensitizers in Antibacterial Photodynamic Therapy: An Overview. *Laser Ther.,* **2018**, *27*, 293–302. https://doi.org/10.5978/islsm.27_18-RA-01.

(23) A. Dwivedi, N. Awasthi, R. Yadav, S. Chaudhary, A. Shukla, N. Kumar, Spectroscopic Analysis of Porphyrin (C 20 H 12 N 4) Ring Studied by DFT Methodology. *J. Inform. Comput. Sci.,* **2020**, *9*, 89–99.

(24) H. Huang, W. Song, J. Rieffel, J. F. Lovell, Emerging Applications of Porphyrins in Photomedicine. *Front. Phys.,* **2015**, *3*, 23. https://doi.org/10.3389/fphy.2015.00023.

(25) G. Singh, S. Chandra, Unravelling the Structural-Property Relations of Porphyrinoids with Respect to Photo- and Electro-Chemical Activities. *Electrochem. Sci. Adv.,* **2023**, *3*, e2100149. https://doi.org/10.1002/elsa.202100149.

(26) P. Rothemund, A. R Menotti, Porphyrin Studies. IV.1 The Synthesis of α,β,γ,δ-Tetraphenylporphine. *J. Am. Chem. Soc.,* **1941**, *63*, 267–270. https://doi.org/10.1021/ja01846a065.

(27) A. D. Adler, F. R. Longo, W. Shergalis, Mechanistic Investigations of Porphyrin Syntheses. I. Preliminary Studies on *Ms* -Tetraphenylporphin. *J. Am. Chem. Soc.,* **1964**, *86*, 3145–3149. https://doi.org/10.1021/ja01069a035.

(28) A. D. Adler, F. R. Longo, J. D. Finarelli, J. Goldmacher, J. Assour, L. A. Korsakoff, Simplified Synthesis for Meso-Tetraphenylporphine. *J. Org. Chem.,* **1967**, *32*, 476–476. https://doi.org/10.1021/jo01288a053.

(29) J. S. Lindsey, The Synthesis of Meso-Substituted Porphyrins. In *Metalloporphyrins Catalyzed Oxidations*; Montanari, F., Casella, L., Eds.; Springer, Netherlands: Dordrecht, **1994**, pp 49–86. https://doi.org/10.1007/978-94-017-2247-6_2.

(30) J. S. Lindsey, H. C. Hsu, I. C. Schreiman, Synthesis of Tetraphenylporphyrins under Very Mild Conditions. *Tetrahedron Lett.,* **1986**, *27*, 4969–4970. https://doi.org/10.1016/S0040-4039(00)85109-6.

(31) J. S. Lindsey, I. C. Schreiman, H. C. Hsu, P. C. Kearney, A. M. Marguerettaz, Rothemund and Adler-Longo Reactions Revisited: Synthesis of Tetraphenylporphyrins under Equilibrium Conditions. *J. Org. Chem.,* **1987**, *52*, 827–836. https://doi.org/10.1021/jo00381a022.

(32) M. Gouterman, Study of the Effects of Substitution on the Absorption Spectra of Porphin. *J. Chem. Phys.,* **1959**, *30*, 1139–1161. https://doi.org/10.1063/1.1730148.

(33) R. Giovannetti, *The Use of Spectrophotometry UV-Vis for the Study of Porphyrins*; IntechOpen, J. Uddin, Ed., Rijeka, **2012**. https://doi.org/10.5772/38797.

(34) S. V. Jenkins, A. Srivatsan, K. Y. Reynolds, F. Gao, Y. Zhang, C.D. Heyes, R. K. Pandey, J. Chen, Understanding the Interactions between Porphyrin-Containing Photosensitizers and Polymer-Coated Nanoparticles in Model Biological Environments. *J. Colloid Interface Sci.,* **2016**, *461*, 225–231. https://doi.org/10.1016/j.jcis.2015.09.037.

(35) M. Imran, M. Ramzan, A. K. Qureshi, M. A. Khan, M. Tariq, Emerging Applications of Porphyrins and Metalloporphyrins in Biomedicine and Diagnostic Magnetic Resonance Imaging. *Biosensors.,* **2018**, *8*, 95. https://doi.org/10.3390/bios8040095.

(36) W. Zhang, W. Lai, R. Cao, Energy-Related Small Molecule Activation Reactions: Oxygen Reduction and Hydrogen and Oxygen Evolution Reactions Catalyzed by Porphyrin- and Corrole-Based Systems. *Chem. Rev.,* **2017**, *117*, 3717–3797. https://doi.org/10.1021/acs.chemrev.6b00299.

(37) A. Yella, H.-W. Lee, H. N. Tsao, C. Yi, A. K. Chandiran, Md. K. Nazeeruddin, E. W.-G. Diau, C.-Y. Yeh, S. M. Zakeeruddin, M Grätzel, Porphyrin-Sensitized Solar Cells with Cobalt (II/III)–Based Redox Electrolyte Exceed 12 Percent Efficiency. *Science.,* **2011**, *334*, 629–634. https://doi.org/10.1126/science.1209688.

(38) M. G. Walter, A. B. Rudine, C. C. Wamser, Porphyrins and Phthalocyanines in Solar Photovoltaic Cells. *J. Porphyr. Phthalocyanines.,* **2010**, *14*, 759–792. https://doi.org/10.1142/S1088424610002689.

(39) A. S.Oliveira, D. Licsandru, R. Boscencu, R. Socoteanu, V. Nacea, L. F. V. Ferreira, A Singlet Oxygen Photogeneration and Luminescence Study of Unsymmetrically Substituted Mesoporphyrinic Compounds. *Int. J. Photoenergy,* **2009**, *2009*, e413915. https://doi.org/10.1155/2009/413915.

(40) M. Ravikumar, D. Raghav, K. Rathinasamy, A. Kathiravan, E. M. Mothi, DNA Targeting Long-Chain Alkoxy Appended Tin(IV) Porphyrin Scaffolds: Photophysical and Antimicrobial PDT Investigations. *ACS Appl. Bio Mater.,* **2018**, *1*, 1705–1716. https://doi.org/10.1021/acsabm.8b00507.

(41) R. Soman, D. Raghav, S. Sujatha, K. Rathinasamy, C. Arunkumar, Axial Ligand Modified High Valent Tin(IV) Porphyrins: Synthesis, Structure, Photophysical Studies and Photodynamic Antimicrobial Activities on Candida Albicans. *RSC Adv.,* **2015**, *5*, 61103–61117. https://doi.org/10.1039/C5RA09343K.

(42) B. Babu, R. C. Soy, J. Mack, T. Nyokong, Non-Aggregated Lipophilic Water-Soluble Tin Porphyrins as Photosensitizers for Photodynamic Therapy and Photodynamic Antimicrobial Chemotherapy. *New J. Chem.,* **2020**, *44*, 11006–11012. https://doi.org/10.1039/D0NJ01564D.

(43) B. Babu, J. Mack, T Nyokong, An Octabrominated Sn(IV) Tetraisopropylporphyrin as a Photosensitizer Dye for Singlet Oxygen Biomedical Applications. *Dalton Trans.,* **2020**, *49*, 9568–9573. https://doi.org/10.1039/D0DT01915A.

(44) R. C. Soy, B. Babu, D. O. Oluwole, N. Nwaji, J. Oyim, E. Amuhaya, E. Prinsloo, J. Mack, T. Nyokong, Photophysicochemical Properties and Photodynamic Therapy Activity of Chloroindium(III) Tetraarylporphyrins and Their Gold Nanoparticle Conjugates. *J. Porphyr. Phthalocyanines,* **2019**, *23*, 34–45. https://doi.org/10.1142/S1088424618501146.

(45) L. C. Makola, T. Nyokong, E. K. Amuhaya, Impact of Axial Ligation on Photophysical and Photodynamic Antimicrobial Properties of Indium (III) Methylsulfanylphenyl Porphyrin Complexes Linked to Silver-Capped Copper

Ferrite Magnetic Nanoparticles. *Polyhedron,* **2021**, *193*, 114882. https://doi.org/10.1016/j.poly.2020.114882.

(46) M. W. Murage, E. K. Amuhaya, B. N. Mbatia, E. K. Muge, S. Derese, Photodynamic antimicrobial activity of indium(III) porphyrin complexes against foodborne pathogens, *J. Porphyr. Phthalocyanines, doi: 10.1142/S1088424624500561*. In Press.

(47) J. Khisa, S. Derese, J. Mack, E. Amuhaya, T. Nyokong, Synthesis, Photophysical Properties and Photodynamic Antimicrobial Activity of Meso 5,10,15,20-Tetra(Pyren-1-Yl)Porphyrin and Its Indium(III) Complex. *J. Porphyr. Phthalocyanines,* **2021**, *25*, 794–799. https://doi.org/10.1142/S1088424621500462.

(48) L. C.Makola, S. Mgidlana, T Nyokong, Amphiphilic Axially Modified Cationic Indium-Porphyrins Linked to Hydrophilic Magnetic Nanoparticles for Photodynamic Antimicrobial Chemotherapy against Gram-Negative Strain; *Escherichia Coli*. *Dyes Pigm.,* **2021**, *192,* 109262. https://doi.org/10.1016/j.dyepig.2021.109262.

(49) L. C. Makola, M. Managa, T.Nyokong, Enhancement of Photodynamic Antimicrobial therapy through the Use of Cationic Indium Porphyrin Conjugated to Ag/CuFe2O4 Nanoparticles. *Photodiagnosis Photodyn. Ther.,* **2020**, *30,* 101736. https://doi.org/10.1016/j.pdpdt.2020.101736.

(50) N. B. Magaela, L. C. Makola, M. Managa, T. Nyokong, T. Photodynamic Activity of Novel Cationic Porphyrins Conjugated to Graphene Quantum Dots against Staphylococcus Aureus. *J. Porphyr. Phthalocyanines,* **2022**, *26*, 392–402. https://doi.org/10.1142/S1088424622500316.

(51) J. H.Jang, K.-S. Jeon, S. Oh, H.-J. Kim, T. Asahi, H. Masuhara, M. Yoon, Synthesis of Sn-Porphyrin-Intercalated Trititanate Nanofibers: Optoelectronic Properties and Photocatalytic Activities. *Chem. Mater.,* **2007**, *19*, 1984–1991. https://doi.org/10.1021/cm0629863.

(52) N. K. Shee, G.-S. Lee, H.-J. Kim, Sn(IV)Porphyrin-Incorporated TiO2 Nanotubes for Visible Light-Active Photocatalysis. *Molecules,* **2024**, *29*, 1612. https://doi.org/10.3390/molecules29071612.

(53) B. Babu, J. Mack, T. Nyokong, Sn(IV)-Porphyrinoids for Photodynamic Anticancer and Antimicrobial Chemotherapy. *Dalton Trans.,* **2023**, *52*, 5000–5018. https://doi.org/10.1039/D3DT00603D.

(54) T. Phromsatit, W. Jantayot, K. Pinsuwan, A. Nuchthanom, S. Boonyuen, Thermal Behavior and the Solvent Effects of ρ-Methoxy Tetraphenylporphyrin (TOMPP), Copper Porphyrin (CuTOMPP), and Nitroporphyrin (CuTOMPP-NO2). *MATEC Web Conf.,* **2016**, *69,* 06002. https://doi.org/10.1051/matecconf/20166906002.

(55) S. L. Tong, J. Zhang, Y. Yan, S. Hu, J. Yu, L. Yu, Supramolecular Assembly Based on a Series of Meso-Tetrakis(p-Methoxyphenyl)Porphrin Complexes. *Solid State Sci.,* **2011**, *13*, 1320–1327. https://doi.org/10.1016/j.solidstatesciences.2011.03.029.

(56) E. R. Baral, D. Kim, S. Lee, M. H. Park, J. G. Kim, Tin(IV)-Porphyrin Tetracarbonyl Cobaltate: An Efficient Catalyst for the Carbonylation of Epoxides. *Catalysts.* **2019**, *9*, 311. https://doi.org/10.3390/catal9040311.

(57) P. Dechan, G. D. Bajju, Synthesis and Spectroscopic Properties of Axial Phenoxide and Para Amino Phenoxide Incorporated Indium (III) Porphyrins. *J. Mol. Struct.,* **2019**, *1195*, 140–152. https://doi.org/10.1016/j.molstruc.2019.05.120.

(58) P. Dechan, G. D. Bajju, P. Sood, U. A. Dar, Crystallographic Elucidations of Indium(III) Porphyrin Conformations, Morphology and Aggregation Behaviour: Comparative Optical Study of Free Base Porphyrins and Their Indium(III) Derivatives at Varying pH. *J. Mol. Struct.,* **2019**, *1183*, 87–99. https://doi.org/10.1016/j.molstruc.2019.01.064.

(59) S. Dingiswayo, B. Babu, E. Prinsloo, J. Mack, T. Nyokong, A Comparative Study of the Photophysicochemical and Photodynamic Activity Properties of Meso-4-Methylthiophenyl Functionalized Sn(IV) Tetraarylporphyrins and Triarylcorroles. *J. Porphyr. Phthalocyanines,* **2020**, *24*, 1138–1145. https://doi.org/10.1142/S1088424620500273.

(60) M. Bartolomeu, C. J. P. Monteiro, M. Fontes, M. G. P. M. S. Neves, M. A. F. Faustino, A. Almeida, Photodynamic Inactivation of Microorganisms in Different Water Matrices: The Effect of Physicochemical Parameters on the Treatment Outcome. *Sci. Total Environ.,* **2023**, *860*, 160427. https://doi.org/10.1016/j.scitotenv.2022.160427.

(61) W. Gładkowski, M. Siepka, T. Janeczko, E. Kostrzewa-Susłow, J. Popłoński, M. Mazur, B. Żarowska, W. Łaba, G. Maciejewska, C. Wawrzeńczyk, Synthesis and Antimicrobial Activity of Methoxy- Substituted γ-Oxa-ε-Lactones Derived from

Flavanones. *Molecules,* **2019**, *24,* 4151. https://doi.org/10.3390/molecules24224151.

(62) B. C. Marques, M. B. Santos, D. B. Anselmo, D. A.Monteiro, E. Gomes, M. F. C. Saiki, P. Rahal, P. L. Rosalen, J. C. O. Sardi, L. O. Regasini, Methoxychalcones: Effect of Methoxyl Group on the Antifungal, Antibacterial and Antiproliferative Activities. *Med. Chem.,* **2020**, *16*, 881–891. https://doi.org/10.2174/1573406415666190724145158.

(63) H. Suwito, Ni'matuzahroh, A. N. Kristanti, S. Hayati, S. R. Dewi, I. Amalina, N. N. T. Puspaningsih, Antimicrobial Activities and In Silico Analysis of Methoxy Amino Chalcone Derivatives. *Procedia Chem.,* **2016**, *18*, 103–111. https://doi.org/10.1016/j.proche.2016.01.017.

(64) A. Ogunsipe, J.-Y. Chen, T. Nyokong, Photophysical and Photochemical Studies of Zinc(II) Phthalocyanine Derivatives—Effects of Substituents and Solvents. *New J. Chem.,* **2004**, *28*, 822–827. https://doi.org/10.1039/B315319C.

(65) S. Fery-Forgues, D. Lavabre, Are Fluorescence Quantum Yields So Tricky to Measure? A Demonstration Using Familiar Stationery Products. *J. Chem. Educ.,* **1999**, *76*, 1260–1264. https://doi.org/10.1021/ed076p1260.

(66) R. L. Brookfield, H. Ellul, A. Harriman, G. Porter, Luminescence of Porphyrins and Metalloporphyrins. Part 11.—Energy Transfer in Zinc–Metal-Free Porphyrin Dimers. *J. Chem. Soc., Faraday Trans. 2*, **1986**, *82*, 219–233. https://doi.org/10.1039/F29868200219.

(67) M. Y. Berezin, S. Achilefu, Fluorescence Lifetime Measurements and Biological Imaging. *Chem. Rev.,* **2010**, *110*, 2641–2684. https://doi.org/10.1021/cr900343z.

(68) I. E. Kochevar, R. W. Redmond, [2] Photosensitized Production of Singlet Oxygen. In *Methods in Enzymology*; Singlet Oxygen, UV-A, and Ozone; Academic Press, Amsterdam, **2000**, Vol. 319, pp 20–28. https://doi.org/10.1016/S0076-6879(00)19004-4.

(69) M. C. DeRosa, R. J. Crutchley, Photosensitized Singlet Oxygen and Its Applications. *Coord. Chem. Rev.,* **2002**, *233-234,* 351–371. https://doi.org/10.1016/S0010-8545(02)00034-6.

(70) Y. Hao, B. M. Liu, T. F. Bennett, C. G. Monsour, M. Selke, Y. Liu, Determination of Singlet Oxygen Quantum Yield of a Porphyrinic Metal–Organic Framework. *J. Phys. Chem. C.,* **2021**, *125*, 7392–7400. https://doi.org/10.1021/acs.jpcc.1c00310.

(61) R. Venkatesan, N. Periasamy, T. S. Srivastava, Singlet Molecular Oxygen Quantum Yield Measurements of Some Porphyrins and Metalloporphyrins. *Proc. Indian Acad. Sci. (Chem. Sci.),* **1992**, *104*, 713–722. https://doi.org/10.1007/BF02839117.

(62) S. Stojanov, A. Berlec, A. Electrospun Nanofibers as Carriers of Microorganisms, Stem Cells, Proteins, and Nucleic Acids in Therapeutic and Other Applications. *Front. Bioeng. Biotechnol.,* **2020**, *8: 130.* https://doi.org/10.3389/fbioe.2020.00130.

(63) S. G. Kumbar, R. James, S. P. Nukavarapu, C. T. Laurencin, Electrospun Nanofiber Scaffolds: Engineering Soft Tissues. *Biomed. Mater.,* **2008**, *3*, 034002. https://doi.org/10.1088/1748-6041/3/3/034002.

(74) Z. S. Tang, N. Bolong, I. Saad, J. L. Ayog, The Morphology of Electrospun Titanium Dioxide Nanofibers and Its Influencing Factors. *MATEC Web Conf.,* **2016**, *47*, 01020. https://doi.org/10.1051/matecconf/20164701020.

(75) A. V. Demyanenko, A. S. Bogomolov, N. V. Dozmorov, A. I. Svyatova, A. P. Pyryaeva, V. G. Goldort, S. A. Kochubei, A. V. Baklanov, Singlet Oxygen 1O2 in Photocatalysis on TiO2. Where Does It Come From? *J. Phys. Chem. C.,* **2019**, *123*, 2175–2181. https://doi.org/10.1021/acs.jpcc.8b09381.

(76) T. Luttrell, S. Halpegamage, J. Tao, A. Kramer, E. Sutter, M. Batzill, Why Is Anatase a Better Photocatalyst than Rutile? - Model Studies on Epitaxial TiO2 Films. *Sci. Rep.,* **2014**, *4*, 4043. https://doi.org/10.1038/srep04043.

(77) R. Katoh, K. Takahashi, K. Sugawa, Quantum Yields of Photoluminescence of TiO2 Photocatalysts. *J. Phys. Chem. C.,* **2022**, *126*, 20954–20959. https://doi.org/10.1021/acs.jpcc.2c06761.

(78) P. Pascariu, C. Cojocaru, A. Airinei, N. Olaru, I. Rosca, E. Koudoumas, M. P. Suchea, Innovative Ag–TiO2 Nanofibers with Excellent Photocatalytic and Antibacterial Actions. *Catalysts,* **2021**, *11,* 1234. https://doi.org/10.3390/catal11101234.

(79) A. Chahardoli, L. Hosseinzadeh, Y. Shokoohinia, A. Fattahi, Production of Rutile Titanium Dioxide Nanoparticles by Trans-Ferulic Acid and Their Biomedical Applications. *Mater. Today Commun.,* **2022**, *33*, 104305. https://doi.org/10.1016/j.mtcomm.2022.104305.

(80) B. Caratão, E. Carneiro, P. Sá, B. Almeida, S. Carvalho, Properties of Electrospun TiO_2 Nanofibers. *J. Nanotechnol.,* **2014**, *2014*, e472132. https://doi.org/10.1155/2014/472132.

(81) X. Yu, T. Hou, Y. Li, X. Sun, S.-T. Lee, Effective Band Gap Reduction of Titanium Oxide Semiconductors by Codoping from First-Principles Calculations. *Int. J. Quantum Chem.,* **2013**, *113*, 2546–2553. https://doi.org/10.1002/qua.24502.

(82) C. Liao, Y. Li, S. C. Tjong, Visible-Light Active Titanium Dioxide Nanomaterials with Bactericidal Properties. *Nanomaterials* **2020**, *10*, 124. https://doi.org/10.3390/nano10010124.

(83) K. Song, Q. Wu, Y. Qi, T. Kärki,. 20 - Electrospun Nanofibers with Antimicrobial Properties. In *Electrospun Nanofibers*, Afshari, M., Ed., Woodhead Publishing Series in Textiles, Woodhead Publishing, Sawston, **2017**, pp 551–569. https://doi.org/10.1016/B978-0-08-100907-9.00020-9.

(84) J. Z. Soo, L. C. Chai, B. C. Ang, B. H. Ong, Enhancing the Antibacterial Performance of Titanium Dioxide Nanofibers by Coating with Silver Nanoparticles. *ACS Appl. Nano Mater.,* **2020**, *3*, 5743–5751. https://doi.org/10.1021/acsanm.0c00925.

(85) S.-Y. Ryu, J. W. Chung, S.-Y. Kwak, Dependence of Photocatalytic and Antimicrobial Activity of Electrospun Polymeric Nanofiber Composites on the Positioning of Ag–TiO2 Nanoparticles. *Compos. Sci. Technol.,* **2015**, *117*, 9–17. https://doi.org/10.1016/j.compscitech.2015.05.014.

(86) W. S. Lee, Y.-S. Park, Y.-K. Cho, Significantly Enhanced Antibacterial Activity of TiO2 Nanofibers with Hierarchical Nanostructures and Controlled Crystallinity. *Analyst,* **2014**, *140*, 616–622. https://doi.org/10.1039/C4AN01682C.

(87) R. F. Bonan, M. F. Mota, R. M. da Costa Farias, S. D. da Silva, P. R. F. Bonan, L. Diesel, R. R. Menezes, D. E. da Cruz Perez, *In Vitro* Antimicrobial and Anticancer Properties of TiO2 Blow-Spun Nanofibers Containing Silver Nanoparticles. *Mater. Sci. Eng. C.,* **2019**, *104*, 109876. https://doi.org/10.1016/j.msec.2019.109876.

(88) L. Wang, J. Ali, C. Zhang, G. Mailhot, G. Pan, Simultaneously Enhanced Photocatalytic and Antibacterial Activities of TiO2/Ag Composite Nanofibers for Wastewater Purification. *J. Environ. Chem. Eng.,* **2020**, *8,* 102104. https://doi.org/10.1016/j.jece.2017.12.057.

(89) S. H. Hwang, J. Song, Y. Jung, O. Y. Kweon, H. Song, J. Jang, Electrospun ZnO/TiO2 Composite Nanofibers as a Bactericidal Agent. *Chem. Commun.,* **2011**, *47*, 9164–9166. https://doi.org/10.1039/C1CC12872H.

(90) B. Pant, H. R. Pant, N. A. M. Barakat, M. Park, K. Jeon, Y. Choi, H.-Y. Kim, Carbon Nanofibers Decorated with Binary Semiconductor (TiO2/ZnO) Nanocomposites for the Effective Removal of Organic Pollutants and the Enhancement of Antibacterial Activities. *Ceram. Int.,* **2013**, *39*, 7029–7035. https://doi.org/10.1016/j.ceramint.2013.02.041.

(91) H. C. T. Firmino, E. P. Nascimento, R. F. Bonan, P. P. Maciel, L. R. C. Castellano, L. N. L. Santana, G. A. Neves, R. R. Menezes, Antifungal Activity of TiO2-CeO2 Nanofibers against *Candida* Fungi. *Mater. Lett.,* **2021**, *283*, 128709. https://doi.org/10.1016/j.matlet.2020.128709.

(92) D. Gugulothu, A. Barhoum, R. Nerella, R. Ajmer, M. Bechelany, Fabrication of Nanofibers: Electrospinning and Non-Electrospinning Techniques. In *Handbook of Nanofibers*; Barhoum, A., Bechelany, M., Makhlouf, A. S. H., Eds.; Springer International Publishing: Cham, **2019**, pp 45–77. https://doi.org/10.1007/978-3-319-53655-2_6.

(93) A. Greiner, J. H. Wendorff, Electrospinning: A Fascinating Method for the Preparation of Ultrathin Fibers. *Angew. Chem. Int. Ed.,* **2007**, *46*, 5670–5703. https://doi.org/10.1002/anie.200604646.

(94) L. Lou, O. Osemwegie, S. S. Ramkumar, Functional Nanofibers and Their Applications. *Ind. Eng. Chem. Res.,* **2020**, *59*, 5439–5455. https://doi.org/10.1021/acs.iecr.9b07066.

(95) M. Managa, E. Antunes, T. Nyokong, T. Conjugates of Platinum Nanoparticles with Gallium Tetra – (4-Carboxyphenyl) Porphyrin and Their Use in Photodynamic Antimicrobial Chemotherapy When in Solution or Embedded in Electrospun Fiber. *Polyhedron,* **2014**, *76*, 94–101. https://doi.org/10.1016/j.poly.2014.03.050.

(96) S. Mapukata, T. Nyokong, Development of Phthalocyanine Functionalised TiO2 and ZnO Nanofibers for Photodegradation of Methyl Orange. *New J. Chem.,* **2020**, *44*, 16340–16350. https://doi.org/10.1039/D0NJ03326J.

(97) A. Jain, D. Vaya, Photocatalytic Activity of TiO2 Nanomaterial. *J. Chil. Chem. Soc.,* **2017**, *62*, 3683–3690. https://doi.org/10.4067/s0717-97072017000403683.

(98) V. Kumaravel, K. M. Nair, S. Mathew, J. Bartlett, J. E. Kennedy, H. G. Manning, B. J. Whelan, N. S. Leyland, S. C. Pillai, Antimicrobial TiO2 Nanocomposite

Coatings for Surfaces, Dental and Orthopaedic Implants. *Chem. Eng. J.,* **2021**, *416,* 129071. https://doi.org/10.1016/j.cej.2021.129071.

(99) I. I. Samoĭlenko, E. I. Vasil'eva, I. B. Pavlova, M. A. Tumanian, [Mechanisms of the bactericidal action of hydrogen peroxide]. *Zh Mikrobiol Epidemiol Immunobiol* **1983**, 12, 30–33.

(100) S. Heo, S. Kim, D. Kang, The Role of Hydrogen Peroxide and Peroxiredoxins throughout the Cell Cycle. *Antioxidants (Basel),* **2020**, *9*, 280. https://doi.org/10.3390/antiox9040280.

(101) I. J. Macdonald, T. J. Dougherty, Basic Principles of Photodynamic Therapy. *J. Porphyr. Phthalocyanines,* **2001**, *5*, 105–129. https://doi.org/10.1002/jpp.328.

(102) W. Spiller, H. Kliesch, D. Wöhrle, S. Hackbarth, B. Röder, G. Schnurpfeil, Singlet Oxygen Quantum Yields of Different Photosensitizers in Polar Solvents and Micellar Solutions. *J. Porphyr. Phthalocyanines,* **1998**, *2*, 145–158. https://doi.org/10.1002/(SICI)1099-1409(199803/04)2:2<145::AID-JPP60>3.0.CO;2-2.

(103) A. Ogunsipe, T. Nyokong, T. Photophysical and Photochemical Studies of Sulphonated Non-Transition Metal Phthalocyanines in Aqueous and Non-Aqueous Media. *J.Photochem. Photobiol. A: Chem.,* **2005**, *173*, 211–220. https://doi.org/10.1016/j.jphotochem.2005.03.001.

(104) S. Mapukata, N. Nwahara, T. Nyokong, The Photodynamic Antimicrobial Chemotherapy of Stapphylococcus Aureus Using an Asymmetrical Zinc Phthalocyanine Conjugated to Silver and Iron Oxide Based Nanoparticles. *J. Photochem. Photobiol. A: Chem.,* **2020**, *402*, 112813. https://doi.org/10.1016/j.jphotochem.2020.112813.

(105) O. L. Osifeko, M. Durmuş, T. Nyokong, Physicochemical and Photodynamic Antimicrobial Chemotherapy Studies of Mono- and Tetra-Pyridyloxy Substituted Indium(III) Phthalocyanines. *J. Photochem. Photobiol. A: Chem.,* **2015**, *301*, 47–54. https://doi.org/10.1016/j.jphotochem.2014.12.011.

(106) G. R. Fulmer, A. J. M. Miller, N. H. Sherden, H. E. Gottlieb, A. Nudelman, B. M. Stoltz, J. E. Bercaw, K. I. Goldberg, NMR Chemical Shifts of Trace Impurities: Common Laboratory Solvents, Organics, and Gases in Deuterated Solvents Relevant to the Organometallic Chemist. *Organometallics,* **2010**, *29,* 2176–2179. https://doi.org/10.1021/om100106e.

(107) M. Scharinger, M. Kuntz, A. Scharinger, J. Teipel, T. Kuballa, S. G. Walch, D. W. Lachenmeier, Rapid Approach to Determine Propionic and Sorbic Acid Contents in Bread and Bakery Products Using 1H NMR Spectroscopy. *Foods,* **2021**, *10* (3), 526. https://doi.org/10.3390/foods10030526.

(108) J. R. Weinkauf, S. W. Cooper, A. Schweiger, C. C. Wamser, Substituent and Solvent Effects on the Hyperporphyrin Spectra of Diprotonated Tetraphenylporphyrins. *J. Phys. Chem. A.,* **2003**, *107*, 3486–3496. https://doi.org/10.1021/jp022046f.

(109) R. I. Y.Quiroz-Segoviano, I. N. Serratos, F. Rojas-González, S. R. Tello-Solís, R. Sosa-Fonseca, O. Medina-Juárez, C. Menchaca-Campos, M. A. García-Sánchez, On Tuning the Fluorescence Emission of Porphyrin Free Bases Bonded to the Pore Walls of Organo-Modified Silica. *Molecules,* **2014**, *19*, 2261–2285. https://doi.org/10.3390/molecules19022261.

(110) M. Uttamlal, A. S. Holmes-Smith, The Excitation Wavelength Dependent Fluorescence of Porphyrins. *Chem. Phys. Lett.,* **2008**, *454*, 223–228. https://doi.org/10.1016/j.cplett.2008.02.012.

(111) S. K. Kuriechen, S. Murugesan, S. Paul Raj, Mineralization of Azo Dye Using Combined Photo-Fenton and Photocatalytic Processes under Visible Light. *J. Catal.,* **2013**, *2013*, e104019. https://doi.org/10.1155/2013/104019.

(112) L. Alagna, A. Capobianchi, M. P. Casaletto, G. Mattogno, A. M. Paoletti, G. Pennesi, G. Rossi, Effect of Molecular Packing on the Solid State Spectra of Ruthenium Phthalocyanine: Anomalous Behaviour of a Monodimensional Stacked Assembly. *J. Mater. Chem.,* **2001**, *11*, 1928–1935. https://doi.org/10.1039/B100041L.

(113) P. Makuła, M. Pacia, W. Macyk, How To Correctly Determine the Band Gap Energy of Modified Semiconductor Photocatalysts Based on UV–Vis Spectra. *J. Phys. Chem. Lett.,* **2018**, *9*, 6814–6817. https://doi.org/10.1021/acs.jpclett.8b02892.

(114) B. D. Viezbicke, S. Patel, B. E. Davis, D. P. Birnie III, Evaluation of the Tauc Method for Optical Absorption Edge Determination: ZnO Thin Films as a Model System. *Phys. Status Solidi B Basic Res.,* **2015**, *252*, 1700–1710. https://doi.org/10.1002/pssb.201552007.

(115) J. Zhang, P. Zhou, J. Liu, J. Yu, New Understanding of the Difference of Photocatalytic Activity among Anatase, Rutile and Brookite TiO2. *Phys. Chem. Chem. Phys.,* **2014**, *16*, 20382–20386. https://doi.org/10.1039/c4cp02201g.

(116) Y. Nosaka, A. Y. Nosaka, Reconsideration of Intrinsic Band Alignments within Anatase and Rutile TiO2. *J. Phys. Chem. Lett.,* **2016**, *7*, 431–434. https://doi.org/10.1021/acs.jpclett.5b02804.

(117) F. Scarpelli, T. F. Mastropietro, T. Poerio. N. Godbert, Mesoporous TiO2 Thin Films: State of the Art. In *Titanium Dioxide - Material for a Sustainable Environment*; IntechOpen, D. Yang, Ed., Rijeka, **2018**. https://doi.org/10.5772/intechopen.74244.

(118) R. de A. Ramos, M. H. Boratto, M. S. Li, L. V. de A. Scalvi, Emission Properties Related to Distinct Phases of Sol-Gel Dip-Coating Titanium Dioxide, and Carrier Photo-Excitation in Different Energy Ranges. *Mat. Res.,* **2017**, *20*, 866–873. https://doi.org/10.1590/1980-5373-MR-2016-0675.

(119) S. T. Mkhondwane, R. Matshitse, T. Nyokong, Porphyrin-Graphitic Carbon Nitride Quantum Dots Decorated on Titanium Dioxide Electrospun Nanofibers for Photocatalytic Degradation of Organic Pollutants. *J. Coord. Chem.,* **2022**, *75*, 2150–2169. https://doi.org/10.1080/00958972.2022.2132153.

(120) S. Loganathan, R. B.Valapa, R. K. Mishra, G. Pugazhenthi, S. Thomas, Chapter 4 - Thermogravimetric Analysis for Characterization of Nanomaterials. In *Thermal and Rheological Measurement Techniques for Nanomaterials Characterization*; Thomas, S., Thomas, R., Zachariah, A. K., Mishra, R. K., Eds., Micro and Nano Technologies, Elsevier, Amsterdam, **2017**, pp 67–108. https://doi.org/10.1016/B978-0-323-46139-9.00004-9.

(121) S. Venugopal Rao, P. T. Anusha, L. Giribabu, S. P. Tewari,Picosecond Optical Nonlinearities in Symmetrical and Unsymmetrical Phthalocyanines Studied Using the Z-Scan Technique. *Pramana - J. Phys.,* **2010**, *75*, 1017–1023. https://doi.org/10.1007/s12043-010-0157-x.

(122) C. Comuzzi, M. Marino, D. Poletti, M. Boaro, P. Strazzolini, New Antimicrobial PVC Composites. Porphyrins Self-Aggregation in Tuning Surface Morphologies and Photodynamic Inactivation towards Sustainable Water Disinfection. *J. Photochem. Photobiol. A: Chem.,* **2022**, *430*, 113967. https://doi.org/10.1016/j.jphotochem.2022.113967.

(123) J.-H. Ha, S. Ko, C.-H. Lee, W. Lee, Y.-R. Kim, Effect of Core Atom Modification on Photophysical Properties and Singlet Oxygen Generation Efficiencies: Tetraphenylporphyrin Analogues Core-Modified by Oxygen and/or Sulfur. *Chem. Phys. Lett.,* **2001**, *349*, 271–278. https://doi.org/10.1016/S0009-2614(01)01231-3.

(124) H. Ramesh, T. Mayr, M. Hobisch, S. Borisov, I. Klimant, U. Krühne, J. M. Woodley, Measurement of Oxygen Transfer from Air into Organic Solvents. *J. Chem. Technol. Biotechnol.,* **2016**, *9*, 832–836. https://doi.org/10.1002/jctb.4862.

(125) T. Daimon, Y. Nosaka, Formation and Behavior of Singlet Molecular Oxygen in TiO2 Photocatalysis Studied by Detection of Near-Infrared Phosphorescence. *J. Phys. Chem. C.,* **2007**, *111*, 4420–4424. https://doi.org/10.1021/jp070028y.

(126) M. N. Alomary, M. A. Ansari, Proanthocyanin-Capped Biogenic TiO2 Nanoparticles with Enhanced Penetration, Antibacterial and ROS Mediated Inhibition of Bacteria Proliferation and Biofilm Formation: A Comparative Approach. *Chem. Eur. J.,* **2021**, *27*, 5817–5829. https://doi.org/10.1002/chem.202004828.

(127) M. Pelaez, P. Falaras, V. Likodimos, K. O'Shea, A. A. de la Cruz, P. S. M. Dunlop, J. A. Byrne, D. D. Dionysiou, Use of Selected Scavengers for the Determination of NF-TiO2 Reactive Oxygen Species during the Degradation of Microcystin-LR under Visible Light Irradiation. *J. Mol. Catal. A Chem.,* **2016**, *425*, 183–189. https://doi.org/10.1016/j.molcata.2016.09.035.

(128) W. Gładkowski, M. Siepka, T. Janeczko, E. Kostrzewa-Susłow, J. Popłoński, M. Mazur, B. Żarowska, W. Łaba, G. Maciejewska, C. Wawrzeńczyk, Synthesis and Antimicrobial Activity of Methoxy- Substituted γ-Oxa-ε-Lactones Derived from Flavanones. *Molecules,* **2019**, *24,* 4151. https://doi.org/10.3390/molecules24224151.

(129) M. Yasuyuki, K. Kunihiro, S. Kurissery, N. Kanavillil, Y. Sato, Y. Kikuchi, Antibacterial Properties of Nine Pure Metals: A Laboratory Study Using Staphylococcus Aureus and Escherichia Coli. *Biofouling,* **2010**, *26*, 851–858. https://doi.org/10.1080/08927014.2010.527000.

(130) M. A. Adefisoye, A. O. Olaniran, Does Chlorination Promote Antimicrobial Resistance in Waterborne Pathogens? Mechanistic Insight into Co-Resistance and Its Implication for Public Health. *Antibiotics,* **2022**, *11*, 564. https://doi.org/10.3390/antibiotics11050564.

(131) N. Yerli Soylu, A. Soylu, D. N. Dikmetas, F. Karbancioglu-Guler, S. Kucukbayrak, M. E. Taygun, Photocatalytic and Antimicrobial Properties of Electrospun TiO2–SiO2–Al2O3–ZrO2–CaO–CeO2 Ceramic Membranes. *ACS Omega,* **2023**, *8*, 10836–10850. https://doi.org/10.1021/acsomega.2c06986.

(132) F. F. Sperandio, Y.-Y. Huang, M. R. Hamblin, Antimicrobial Photodynamic Therapy to Kill Gram-Negative Bacteria. *Recent Pat. AntiInfect. Drug Discov.,* **2013** *8*, 108–120. doi: 10.2174/1574891x113089990012.

(133) A. Magadla, Y. I. Openda, L. S. Mpeta, T. Nyokong, Evaluation of the Antibacterial Activity of Gallic Acid Anchored Phthalocyanine-Doped Silica Nanoparticles towards Escherichia Coli and Staphylococcus Aureus Biofilms and Planktonic Cells. *Photodiagnosis. Photodyn. Ther.* **2023**, *42*, 103520. https://doi.org/10.1016/j.pdpdt.2023.103520.

(134) A. Hampden-Martin, J. Fothergill, M. El Mohtadi, L. Chambers, A. J. Slate, K. A. Whitehead, K. Shokrollahi, Photodynamic Antimicrobial Chemotherapy Coupled with the Use of the Photosensitizers Methylene Blue and Temoporfin as a Potential Novel Treatment for Staphylococcus Aureus in Burn Infections. *Access Microbiol.,* **2021**, *3*, 000273. https://doi.org/10.1099/acmi.0.000273.

Results

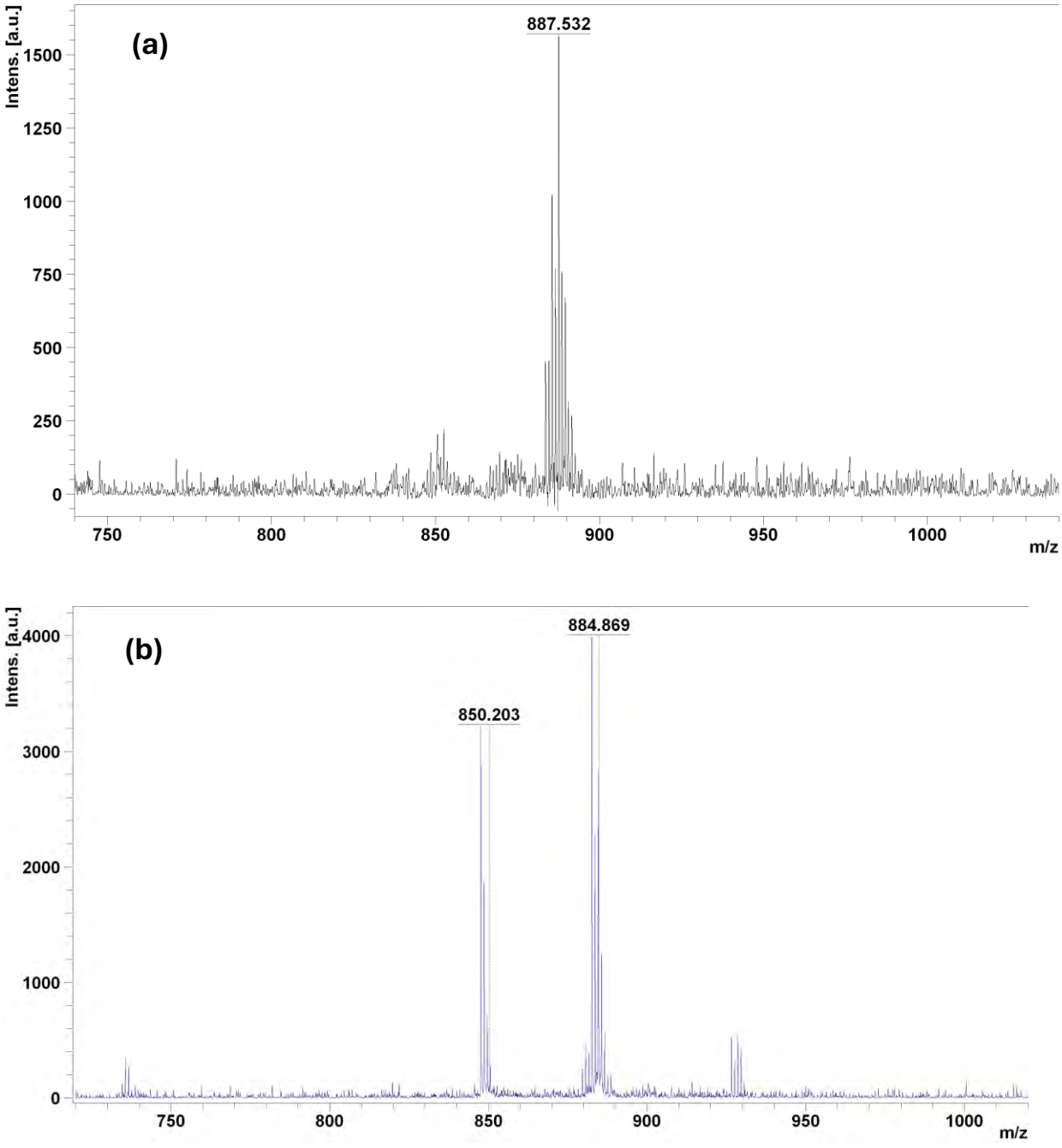

Figure S1: Mass spectroscopy of (a) **1-Sn** and (b) **1-In**

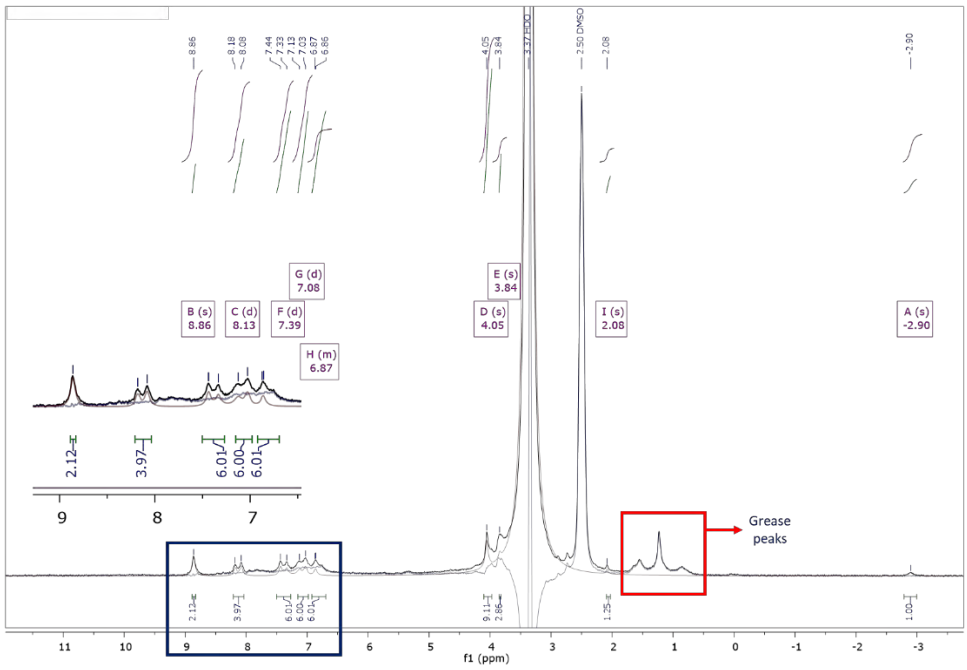

Figure S2a: Integrated ^{1}H NMR spectrum of **3**.

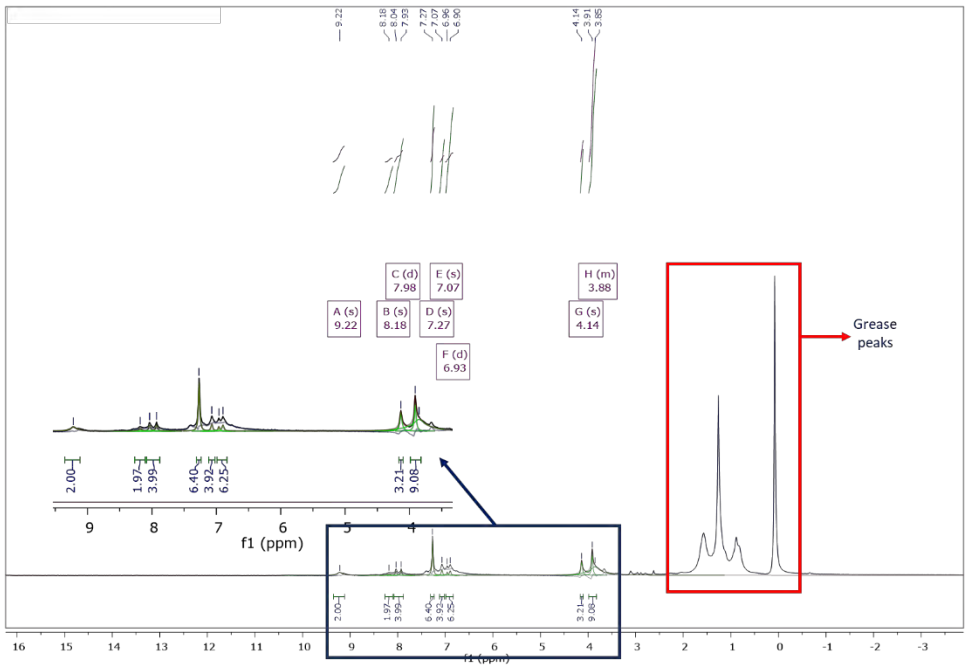

Figure S2b: Integrated ^{1}H NMR spectrum of **3-Sn**.

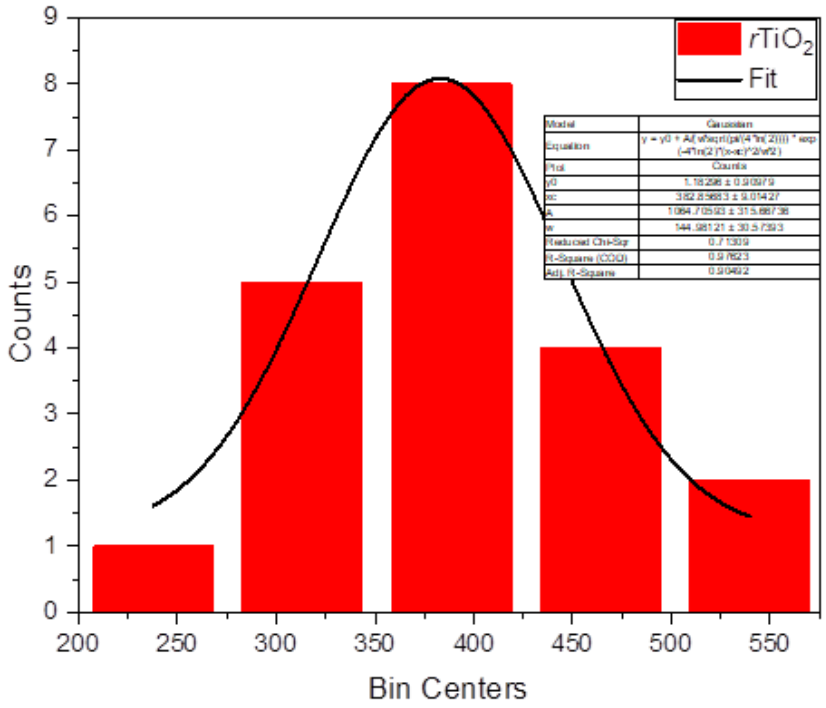

Figure S3: An example of a histogram (rTiO$_2$) used for size determination of the nanofibers.

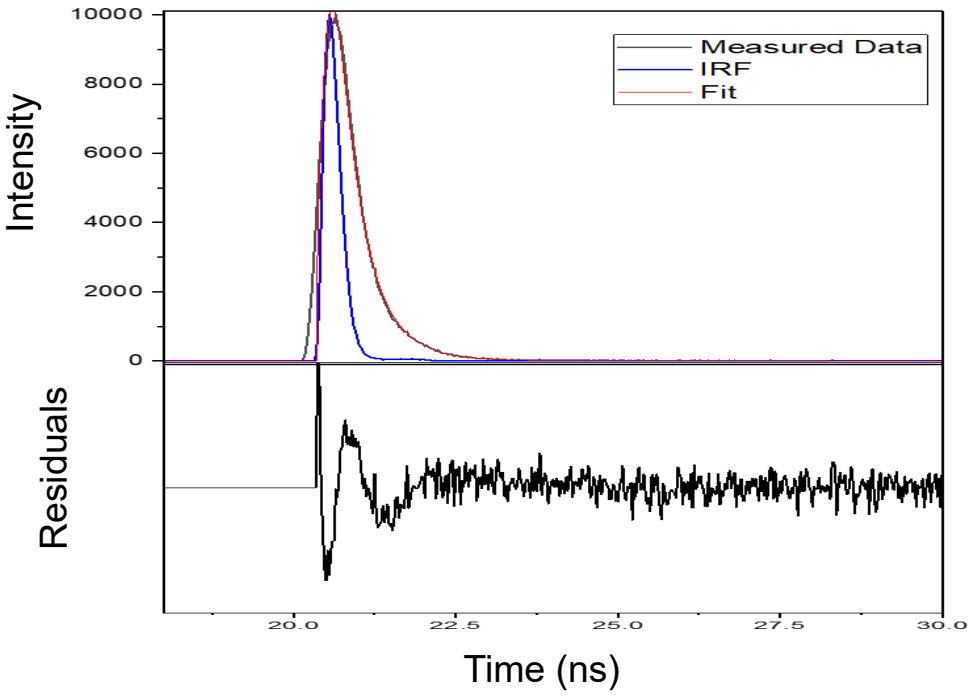

Figure S4: Fluorescence decay graph for **1-In** as an example in DMF.

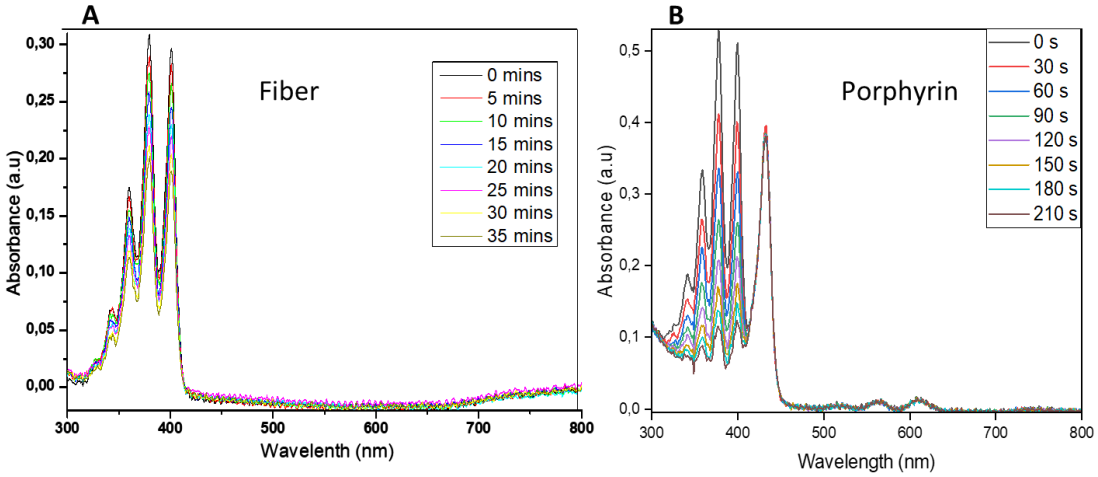

Figure S5: Production of singlet oxygen after light irradiation over a 35 min period for nanofibers (TiO_2) (A) in the presence of ADMA (in water) and a 210 s period for the porphyrins (**1-Sn**) (B) in the presence of DMA in DMF.

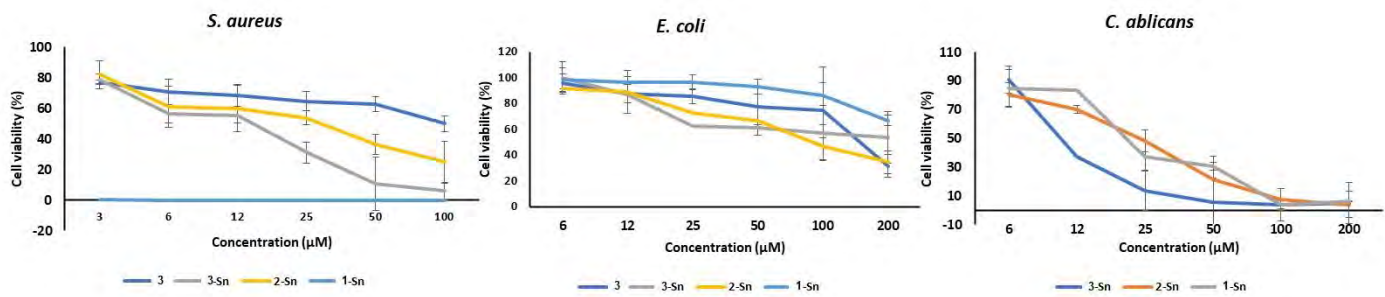

Figure S6: Cell viability graphs of **1, 1-Sn, 2-Sn** and **3-Sn** porphyrins post-irradiation treatment against *S. aureus, E. coli* and *C. albicans*.

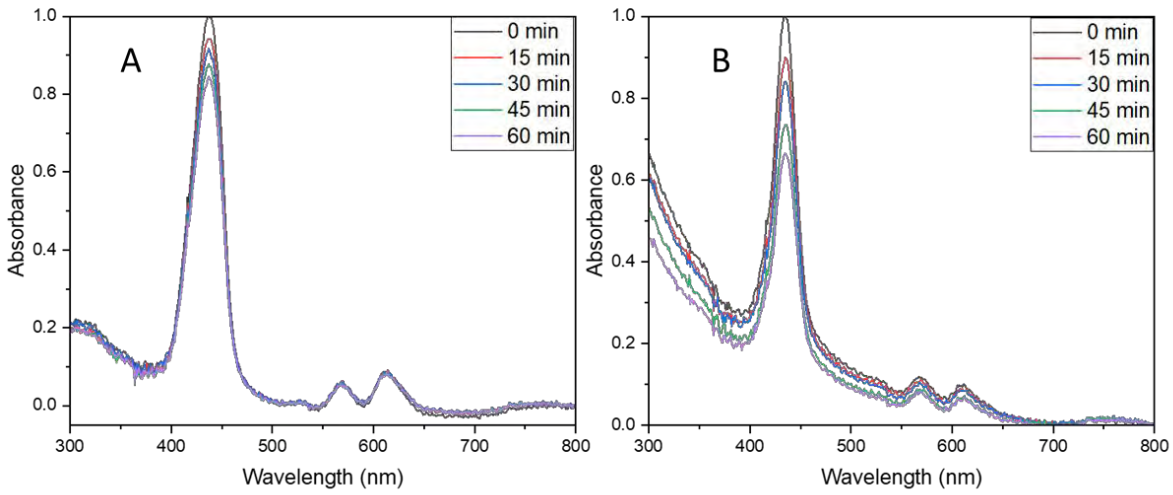

Figure S7: Photostability graphs of porphyrin complexes **1-Sn** (A) and **1-In** (B) alone, over a 60 min irradiation, in 1% DMF aqueous media.

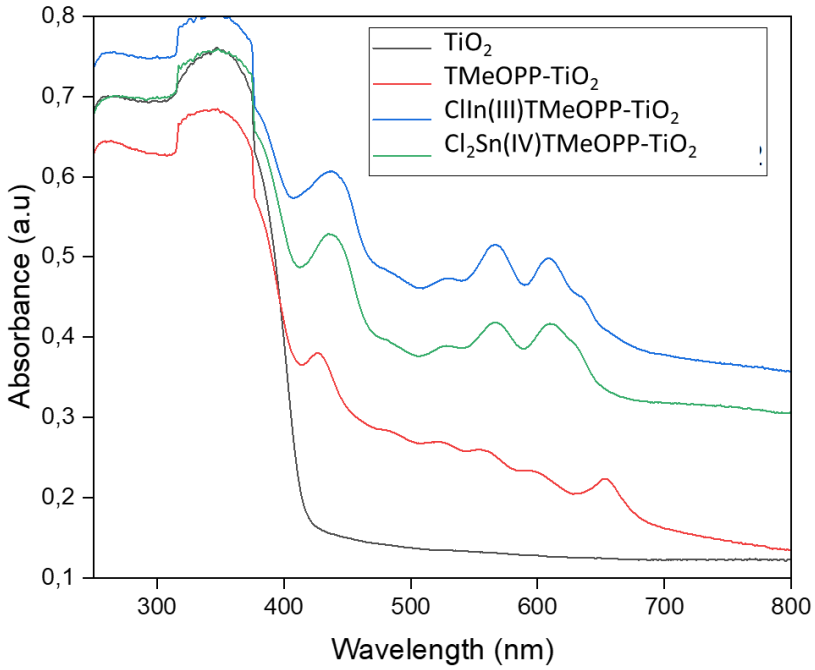

Figure S8: UV-Vis Spectra of Bare TiO_2 TiO2_**1**, TiO_2 _**1-Sn** and TiO_2 _**1-In** nanofibers (solid state) after application in antimicrobial photodynamic inactivation.

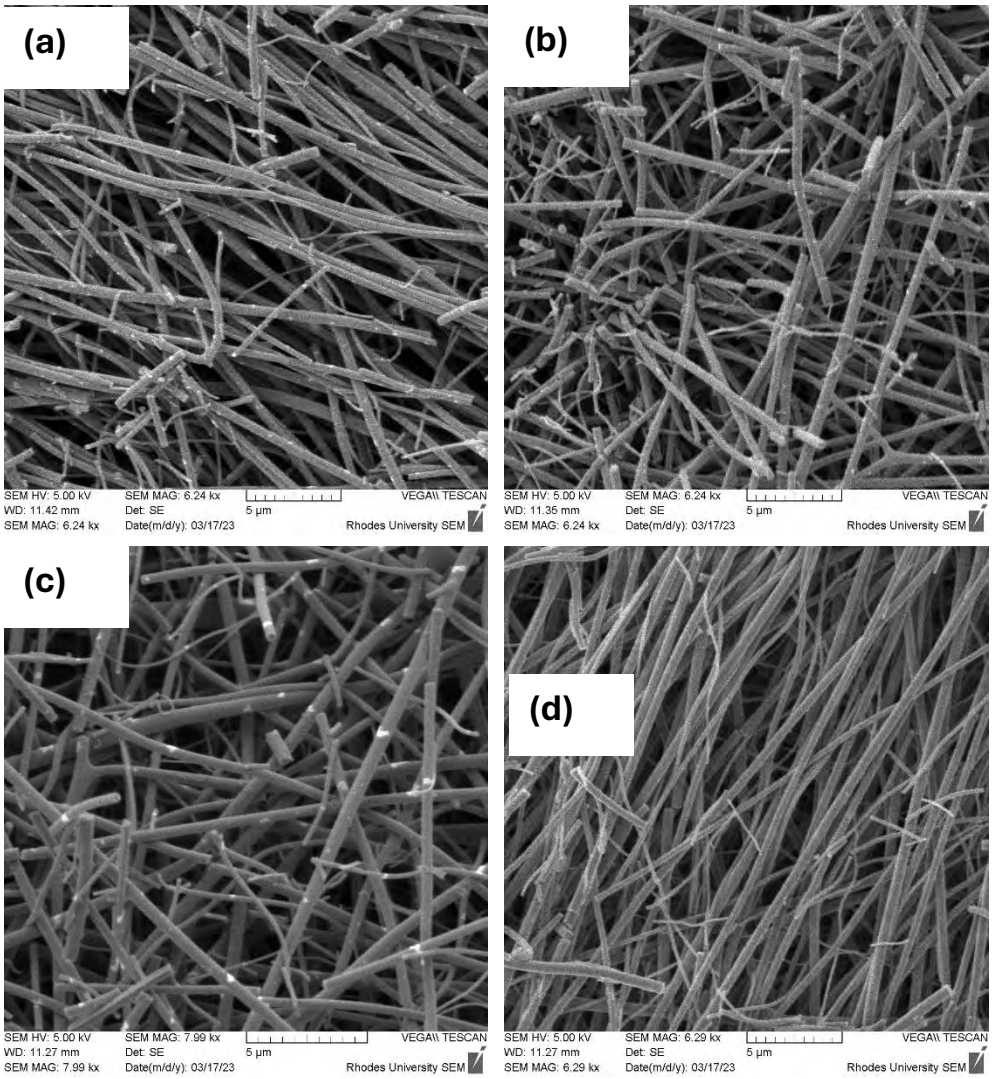

Figure S9: SEM images of (a) bare calcinated TiO_2, (b) TiO_2_**1**, (c) TiO_2 _**1-Sn** and (d) TiO_2_**1-In** nanofibers after application in antimicrobial photodynamic inactivation.

Table S1: Photodegradation of porphyrins complexes in solution

	DMF (%)	Aqueous media 1%DMF (%)
1-Sn	6.5	15.4
1-In	8.7	34.0